Very Steep Solitary Waves in Two-Dimensional Free Surface Flow

Stephen Wade

Thesis submitted for the degree of

Doctor of Philosophy

in

Applied Mathematics

at

The University of Adelaide

November 3, 2015

Abstract

Very steep solitary waves on the surface of a flow in a channel have been widely studied, in part due to their connection with the onset of wave breaking. An important extension to the study of solitary waves in a channel is the effect of localised forcing on their evolution. Forced very steep waves are the focus of this study, as they have received only limited attention in the past, and are of importance in the latter stages of wave breaking. Two types of forcing are considered, a localised pressure disturbance applied to the free surface, or a localised change to the otherwise flat topography of the channel, such as a bump or a trench. Gravity is the only body force considered, as surface tension is neglected. Boundary-integral methods are used to determine solutions to the free surface, whose evolution is described by a fully nonlinear potential flow model.

It is shown that for both types of forcing, like for unforced waves, the waves approach a Stokes limiting configuration as the wave-height is increased, and the solutions also exhibit non-uniqueness with respect to quantities such as the wave energy. The stability of the forced solutions is investigated here using a weakly nonlinear theory, valid in the limit when the wave-height and the steepness are small. The time-evolution of a perturbed steady solution is computed, and linearised stability analysis is performed numerically. It is shown that the unstable solutions may emit a solitary wave ahead of the forcing, and attain the form of the stable solution near the forcing location.

Signed Statement

I certify that this work contains no material which has been accepted for the award of any other degree or diploma in my name, in any university or other tertiary institution and, to the best of my knowledge and belief, contains no material previously published or written by another person, except where due reference has been made in the text. In addition, I certify that no part of this work will, in the future, be used in a submission in my name for any other degree or diploma in any university or other tertiary institution without the prior approval of the University of Adelaide.

I consent to this copy of my thesis, when deposited in the University Library, being made available for loan and photocopying, subject to the provisions of the Copyright Act 1968.

I also give permission for the digital version of my thesis to be made available on the web, via the University's digital research repository, the Library Search and also through web search engines.

SIGNED: _____ DATE: _____

Acknowledgements

First I must sincerely thank my three supervisors. Benjamin Binder, I learnt so much from working with you, your insight was invaluable in completing this story. Trent Mattner, you inspired or helped me get unstuck numerous times in our conversations and Jim Denier, your advice, guidance and experience cannot be praised highly enough. I am so grateful for all your work, and for the chance you took on me, as there are many in your position who wouldn't have.

Thank you also, Nigel Bean, for sharing your experience in the preparation of a thesis, and to the truly excellent staff at the School of Mathematical Sciences for their organisation and support over the years.

There are some fellow postgraduates to thank. Geraldine Wong, thank you for showing me the ropes and being my so-called PhD 'mum'. Rhys Bowden, thank you for your friendship and being there to bounce ideas off of. Josephine Varney, I would be so much worse off without your wise counsel and support, and the same can be said for Jennifer Mecking and Maria Tsarenko who assisted from afar. Thanks to Aiden Fisher for being my 'brofessor'. And a very heartfelt 'thank you' to those who helped pick me up whenever I fell down; Alice Bednarz, Jess Kasza, Xian Lim, Kate Simms, Tyman Stanford, Paul Tune, David Wilke and Lyron Winderbaum.

And my outside supporters, my family, Mum, Dad, and Simon, the recent additions too; you are in my heart at all times, and this would not have been possible without you. I will be forever grateful to my 'fort' champion and dear friend, Cate Dyer. Finally my greatest friend, Louise Uphill; I will happily listen intently to, and critically analyse, your stories for the rest of my life, and you must know that this would have not been completed without you.

I can't justly express my gratitude, thank you all for being a part of this story in my life, for your work, and for the precious and kind gifts of support, wisdom and love.

Contents

List of Figures

Chapter 1

Introduction

Steep waves are a widespread phenomenon in fluid flows, one only needs to look to the ocean to find steep waves generated by storms, tsunami caused by earthquakes, or the waves approaching a shoreline before they spectacularly and chaotically break. The study of steep waves is, at least in part, motivated by this association to wave-breaking. The focus in this thesis is to further our understanding of this important type of wave.

Very steep (periodic and solitary) gravity waves, without any other forcing present, have been studied since the late 19^{th} century. The limiting case of the highest wave was conjectured to have a Stokes corner flow [58, 59], and this structure was confirmed shortly after by calculations in the early 20^{th} century of the highest wave by Havelock [29]. Eventually, the existence of these waves was proven by Toland [61].

Although the highest waves with these configurations were proven to exist, accurate results for the properties of the wave required considerable computational and analytical effort. Lenau [37] used a combination of asymptotic results and numerical methods to determine very precisely the height and speed of the wave. Further properties of these waves, such as their momentum and energy, were

then calculated by Longuet-Higgins & Fenton [39] and Williams [69] using a combination of asymptotic expansions and numerical techniques.

Highly nonlinear phenomena slowly became apparent in the study of the 'almost-highest' waves, those just shorter than the highest wave. Longuet-Higgins & Fenton [39] showed, via Padé approximation, that the speed and energy of the wave pass a local maxima as the wave-height increases. Independent numerical calculations by Byatt-Smith & Longuet-Higgins [11] and others [30, 51] confirmed this behaviour for solitary waves, and for periodic waves by Vanden-Broeck [64]. The local maxima of the total energy with respect to wave-height was of particular interest once it was observed to correspond to the onset of an instability; Tanaka [60] performed a stability analysis of the almost-highest solutions, and showed that this maxima corresponds with the onset of a superharmonic (short wavelength) instability. Longuet-Higgins & Cleaver [38] and Longuet-Higgins & Tanaka [41] demonstrated that this instability is caused by the flow near the crest of the wave.

Furthermore, rather than passing through just one local maxima, the speed and energy were conjectured to pass through a potentially infinite number of local maxima and minima as the wave height increases; these local turning points have been estimated asymptotically by Longuet-Higgins & Fox [40], numerically by Maklakov [43], while the existence of at least one turning point has been proven by McLeod [46].

The effect of an additional localised forcing on gravity waves has been studied extensively. In this thesis we consider two additional types of forcing, that of a pressure disturbance on the free surface, and that of a small localised bump or trench in the topography of the flow. The waves subjected to these types of forcing will be referred to as 'forced', while those not will be called 'unforced'.

The theory of such forced waves in the small-amplitude limit is well established, dating back more than a century, see Lamb [35]. Akylas [2] and Grimshaw & Smyth

[27] derived models in the long-wavelength limit which exhibited an unusual phenomenon; the generation of upstream solitary waves in the transcritical regime. This feature was established numerically and experimentally by Wu [70] and Lee *et al.* [36]. Steady waves in the non-transcritical regime were also identified using this model, in narrow and wide disturbance limits, by Akylas and Grimshaw & Smyth; and other solutions for the narrow obstacle limit were later reported by Malomed [44] and Miles [47].

However, there are only limited results for such forced waves in the almost-highest regime. Dias & Vanden-Broeck [15] and Elcrat & Miller [21] considered the case of a triangular disturbance in the topography, and calculated highest and almost-highest waves, although the details in the latter regime were not determined.

In this thesis we show that forced steady solutions approach the Stokes limiting configurations for both types of disturbance. The limiting configurations for forced waves have an included angle of 120° at the highest crests of the flow. We find that like the unforced regime, the almost-highest forced solutions exhibit non-uniqueness of solutions with respect to properties such as speed or energy of the flow as the wave-height is increased.

However, we find there are some differences between the waves generated by the two types of forcing and the unforced waves. The pressure disturbance admits almost-highest solutions with a cusp at the crest, whereas these are not observed for topographical forcing nor in the unforced case. We find that for the almost-highest waves with a cusp, the orientation of the peaks of the limiting configuration are affected by the nearby pressure disturbance, which is not observed in the crests of an unforced solution. For the topographical disturbance, we find that a further increase in the depth of the trench does not significantly alter the free surface of the flow when the trench is considerably deep.

In this study the flow is taken to be the two-dimensional and irrotational flow of an incompressible and inviscid fluid. Gravity is the only body force accounted for, as surface tension is neglected. Throughout this study we restrict our attention to symmetric waves and to flow that is supercritical, defined as when the depth-based Froude number F, defined in (2.1.1), is greater than unity. The potential flow model, derived in Appendix A, is referred to as the fully nonlinear model.

In Chapter 2 we present the derivation of a boundary-integral method for solving the fully nonlinear model, and we present an outline of the numerical continuation method from Allgower & Georg [3]. Numerical continuation is used to find families of solutions to the algebraic systems presented in Chapters 3 and 4 which correspond to flow past a pressure disturbance and a topographical disturbance respectively. The boundary integrals are evaluated by discretising the flow domain, where an irregular grid inspired by Hunter & Vanden-Broeck [30] is used to improve the accuracy for the almost-highest solutions. The error in evaluating these integrals is shown to be bounded in Appendix B, extending the results of Noble & Beighton [48] to account for a change of variables in the integration.

We also present a weakly nonlinear model governed by a forced Korteweg de-Vries (fKdV) equation [33]. Our derivation follows that of Shen [54], presented in Appendix C. The weakly nonlinear model is only valid when the flow is near critical and the forcing is small, however the model proves useful in classifying solutions, identifying the free parameters in the system and for studying the unsteady behaviour of the forced waves. The weakly nonlinear theory identifies the forced wave solutions as either a perturbation to a uniform stream or as a perturbation to one or two solitary waves. These classifications are also applied to our fully nonlinear results.

We enumerate the different types of waves as types I to V. A sketch of these

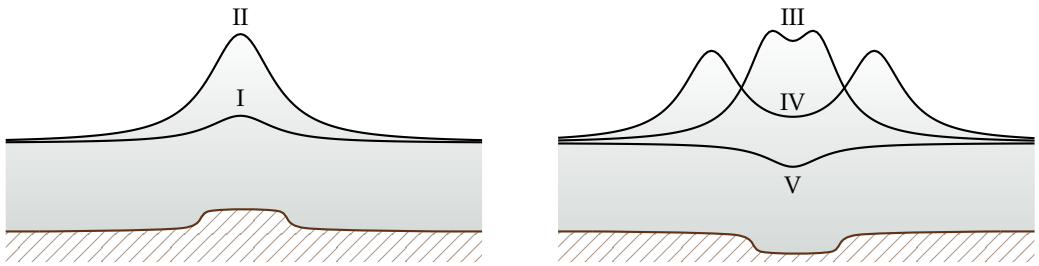

Figure 1.1.1: Sketch of the five solution types identified by the weakly nonlinear theory.

different types of waves is provided in figure 1.1.1, where a bump or trench in the topography is used to illustrate the type of disturbance appropriate to the enumerated wave type. Type-I and type-V waves are perturbations to uniform streams, being waves of elevation and depression respectively. Waves of types II or III are shown to be perturbations to a single solitary wave, where the type-II wave has a single crest and the type-III wave has a cusp-like appearance with two peaks. Waves of type IV are perturbations to two solitary waves, with two distinct crests.

In Chapter 3 we determine the solution space for the flow past a pressure disturbance, following from the results in Wade *et al.* [68]. It is confirmed that for a fixed forcing, non-uniqueness with respect to energy or speed of the wave is present for the almost-highest waves. These are all type-II–IV waves, and all approach a Stokes limiting configuration of a corner flow with an included angle of 120° and a stagnation point at the crest. An additional effect due to the presence of the nearby forcing is observed in the numerical results, and is explored by a modified Stokes' analysis, showing that the crest is rotated slightly from the horizontal for the type-III waves. The stability of all five types of wave is considered in Chapter 5.

In Chapter 4 the solution space for the flow past a topographical disturbance

is considered. The fully nonlinear solution space is significantly different to that observed for a pressure disturbance when considering the amplitude of forcing-wave height plane. In the case where the forcing represents a trench, when the trench gets very deep, an increase in the amplitude of the disturbance no longer produces a significant difference in the shape of the free surface. For this reason, the computational method is no longer able to find converged solutions for very deep trenches.

In the domain where converged solutions could be found for flow past a topographical disturbance, the almost-highest waves of type II and IV were observed, and both demonstrate the non-uniqueness that the unforced waves exhibit as they approach a Stokes limiting configuration. The type-III waves do not appear to approach a limiting configuration for this type of disturbance, unlike in the case of a pressure disturbance. The stability analysis presented in Chapter 5 also applies to the topographical disturbance, at least where the weakly nonlinear model is a valid approximation.

The time-dependent fKdV equation is used in Chapter 5 to investigate the stability of our newly identified steady solutions. The stability of the type-III and type-IV solutions have not been previously investigated. Two approaches are used within this chapter, the first being to perturb the steady solution and compute the evolution of the free surface using a spectral approximation to the time-dependent fKdV, similar to the approach of Chardard *et al.* [14]. The second approach is to perform a linearised stability analysis of the fKdV equation. This follows the approach used by Ee & Clarke [18] of numerically finding the eigenvalues and eigenmodes of a spectral approximation to the linearised fKdV.

The evolution of the perturbed steady solutions indicates that waves that are classified as perturbations to a solitary wave are unstable, whereas those waves classified as perturbations to uniform streams are stable. The peaks of the type-III

waves will coalesce, before emitting a solitary wave upstream and a combination of nonlinear solitary-like waves and dispersive oscillatory waves downstream. The type-IV waves when perturbed will, depending upon the exact perturbation as discussed in Chapter 5, immediately emit a solitary wave upstream and a dispersive wave downstream, then after some time emit another solitary wave upstream together with some downstream solitary and dispersive waves.

The linearised analysis in Chapter 5 agrees with results obtained previously by Camassa & Wu [12] and Ee & Clarke [18]. The perturbations to uniform streams are linearly stable, whereas the perturbations to solitary waves are not, due to the appearance of eigenmodes with positive real part. There are some limitations to the linearised stability analysis as the amplitude of the disturbance gets small, which is attributed to the assumption of periodicity of the domain.

In the final chapter, we summarise the results of Chapter 3–5, make some concluding remarks and discuss some potential avenues for future work.

Chapter 2

Formulation

This chapter begins with a statement of the fully nonlinear governing equations for the steady potential flow past either a pressure or topographic disturbance. From this starting point the boundary integral formulation for the shape of steep waves on the surface is presented, followed by the details of the numerical scheme we employ for finding solutions. We derive an expression for the error in the numerical evaluation of the integrals, allowing us to demonstrate that the error is well behaved as an irregular grid is further refined. Lastly a corresponding weakly nonlinear model is presented in order to identify the system's free parameters, classify the solutions, and to provide a model for the investigation of unsteady behaviour which is considered in Chapter 5.

2.1 Model

The flow in a channel can be modelled by a two-dimensional irrotational flow of an incompressible and inviscid fluid of uniform density, otherwise known as a potential flow model, see Batchelor [6]. The two-dimensional flow domain is shown in figure 2.1.1. For this model, the domain is bounded above by a free

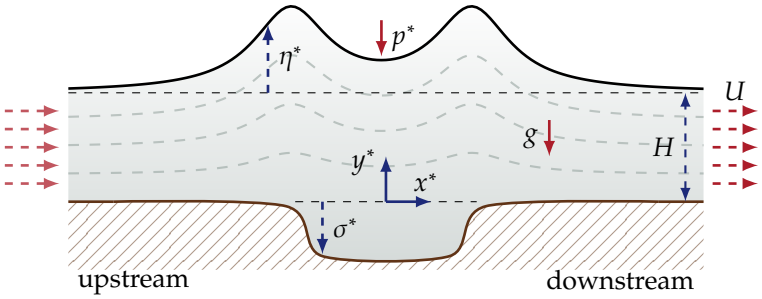

Figure 2.1.1: Schematic of the flow in a channel with either a pressure disturbance travelling with a wave, or a topographical disturbance such as smooth trench in the floor of the channel.

surface which is taken to be the interface between the water in the channel and the air above it. It is also bounded below by the impermeable topography of the channel, which is assumed to be flat in the far upstream and downstream regions of the flow.

The flow is described by its density, height, speed and the acceleration due to gravity. The density in the channel is taken to be uniform and is given by the constant ρ. The flow far downstream is an undisturbed uniform flow, which provides two parameters for the flow, the height, H, of the interface between fluid and air and a horizontal speed, U. A Cartesian coordinate system (x^*, y^*) is chosen with the x^* axis aligned with the uniform topography far upstream and far downstream. The y^* axis is orthogonal to the x^* axis, with y^* positive in the opposite direction of the acceleration due to gravity, whose magnitude is denoted by g. The free surface can now be described by the coordinates $y^* = H + \eta^*$ for some unknown $\eta^*(x^*)$. Similarly, the function $\sigma^*(x^*)$ specifies the location of the bottom topography at $y^* = \sigma^*$. Although the pressure is defined throughout the fluid, only the pressure disturbance on the free surface is required in order to close the problem, and this is given by the function $p^*(x^*)$. As we only consider systems with one disturbance, one of either σ^* or p^* is assumed to be zero. When

considering unsteady flow, the non-dimensional time variable is denoted t^*.

2.1.1 Non-dimensional variables

We non-dimensionalise all lengths with respect to the unperturbed channel depth, H, and all velocities with respect to the uniform stream speed, U. We then define non-dimensional variables (x, y) with corresponding non-dimensional velocities (u, v) as $(x, y) = (x^*, y^*)/H$ and $(u, v) = (u^*, v^*)/U$. The non-dimensional pressure variable is given by $p = p^*/\rho g H$, and the non-dimensional time variable is $t = UH^{-1}t^*$.

The Froude number F for this flow is given by the ratio of the uniform stream speed to the linear long-wave speed, thus

$$F = \frac{U}{\sqrt{gH}}. \tag{2.1.1}$$

A Froude number greater than one indicates the flow is supercritical, a flow regime where the waves predicted by the small-amplitude linear theory are travelling slower than the uniform stream (see Stoker [57]).

2.1.2 Disturbances

2.1.2.1 Pressure disturbance

To model a localised pressure disturbance on the free surface, we assume that the pressure, p, is a smooth rapidly decaying function of x. In particular we choose a Gaussian function with two real parameters A and B, given by

$$p(x) = \frac{AB}{\sqrt{\pi}} e^{-(Bx)^2}, \tag{2.1.2}$$

where $B > 0$. This pressure term satisfies $\int_{-\infty}^{\infty} p(x)\,\mathrm{d}x = A$, and so we will refer to A as the amplitude of forcing. Both the absolute value of A and the value of B

are linearly related to the magnitude of the pressure at $x = 0$. The parameter B is also related to the spatial rate of decay of the disturbance, and the larger B is, the narrower the disturbance. Taking the limit of very narrow disturbances gives

$$\lim_{B\to\infty} p(x) = \lim_{B\to\infty} \frac{AB}{\sqrt{\pi}} e^{-(Bx)^2} = A\delta(x),$$

where $\delta(x)$ is the Dirac delta function.

2.1.2.2 Topographical disturbances

The localised perturbation to the topography can be given by having either a trench along the bottom, as shown schematically in figure 2.1.1, or a bump intruding into the flow. The bump or trench is modelled in this thesis by a pair of smoothed steps, each of which is given by hyperbolic tangent functions. The topography is thus specified by

$$\sigma(x) = \frac{A}{2l} \left[\tanh S(x + l/2) - \tanh S(x - l/2)\right]. \tag{2.1.3}$$

The quantity A is again referred to as the amplitude of the disturbance. The topographical disturbance given by (2.1.3) is a smooth bump when $A > 0$, and is a trench for $A < 0$. The parameter S determines the steepness of the smoothed steps, and we fix this throughout at $S = 10$. Much larger values of S will make the corners of the disturbance sharper, and for this the potential flow may not be an appropriate model, while very small values of $S \ll 1$ would increase significantly the length of the disturbance. The distance between the inflexion points of the topographical disturbance at $\pm l/2$ is fixed at unity, i.e. $l = 1$ throughout.

The function $\sigma(x)$ given by (2.1.3) has the property (see appendix C.2) that

$$\int_{-\infty}^{\infty} \sigma(x)\,\mathrm{d}x = A,$$

and, like $p(x)$ given by (2.1.2), approaches $A\delta(x)$ as the limit of the disturbance width $l \to 0$ is taken. This also shows that $|A|$ is the area of the disturbance.

2.1.3 The governing equations

The non-dimensional form of the fully nonlinear time-dependent model is derived in Appendix A. The system of equations for our model is comprised of a governing equation (A.6), and boundary conditions on the topography, the free surface and the far field. The boundary conditions are no-penetration (kinematic) conditions on the topography and the free surface, given by equations (A.4) and (A.5), and a dynamic boundary condition on the free surface, given by Bernoulli's equation (A.9). The far-field conditions are given by (A.8).

The equations are restated here assuming a steady flow and using the velocity potential ϕ derived from the equations $u = \phi_x$ and $v = \phi_y$. For steady flows, all field variables are independent of time and it follows that all partial derivatives with respect to t can be set equal to zero. The steady flow is solved using boundary-integral methods, in particular the inverse plane methods introduced by Vanden-Broeck & Schwartz [67] and used more recently by Binder *et al.* [10], Dias & Vanden-Broeck [16], Lustri *et al.* [42], Vanden-Broeck [66] which we will formulate in §2.2.

Laplace's equation emerges as the governing equation of the velocity potential from either the divergence-free velocity condition (A.6) or by recalling that ϕ is the real part of an analytic function defined by (A.7), thus

$$\phi_{xx} + \phi_{yy} = 0 \tag{2.1.4}$$

in the domain of the fluid $\sigma < y < 1 + \eta$. The kinematic boundary conditions (A.4) and (A.5) are;

$$\phi_x \eta_x = \phi_y \quad \text{for } y = 1 + \eta(x), \text{ and} \tag{2.1.5}$$

$$\phi_x \sigma_x = \phi_y \quad \text{for } y = \sigma(x). \tag{2.1.6}$$

Bernoulli's equation (A.9), in terms of ϕ, is applied on the free-surface streamline

to give the dynamic boundary condition

$$\frac{1}{2}(\phi_x^2 + \phi_y^2) + \frac{1}{F^2}(y + p) = \frac{1}{2} + \frac{1}{F^2} \quad \text{on } y = 1 + \eta. \tag{2.1.7}$$

To close the problem we impose the far-field downstream condition

$$\phi \sim x \quad \text{and} \quad \eta \to 0 \quad \text{as } x \to \infty.$$

In addition to these physical boundary conditions we also impose a radiation condition, which ensures that the waves are generated only by the disturbance and not from reflections from the far field; this ensures that all waves are advected out of the domain away from the source of the disturbance. In this model the radiation condition implies that any non-local waves are downstream of the disturbance, and thus for symmetric flows, no non-local waves will be present.

2.2 Conformal mapping

To determine the shape of the free surface, a boundary-integral method is used that is based on conformal mappings of the flow domain. Conformal maps preserve the analyticity of quantities of the flow in the flow domain, and so the Cauchy integral formula [5] is used to provide an equation allowing for the solution for the free surface without solving for the entire flow domain. Consider the flow in the complex plane $z = x + \mathrm{i}y$, one such example with a smooth trench is shown in the upper left of figure 2.2.2. Introduce the steady complex potential $f(x, y) = \phi(x, y) + \mathrm{i}\psi(x, y)$. Without loss of generality we set $\psi = 1$ on the free surface, and it then follows that $\psi = 0$ on the bottom of the channel from the definition of the non-dimensional stream-function. The mapping from the z-plane to the f-plane is illustrated in the top two images presented in figure 2.2.2.

The domain of the flow is now exactly known in the f-plane, it consists of the simple region between the horizontal lines $\psi = 0$ and $\psi = 1$. The function ϕ will

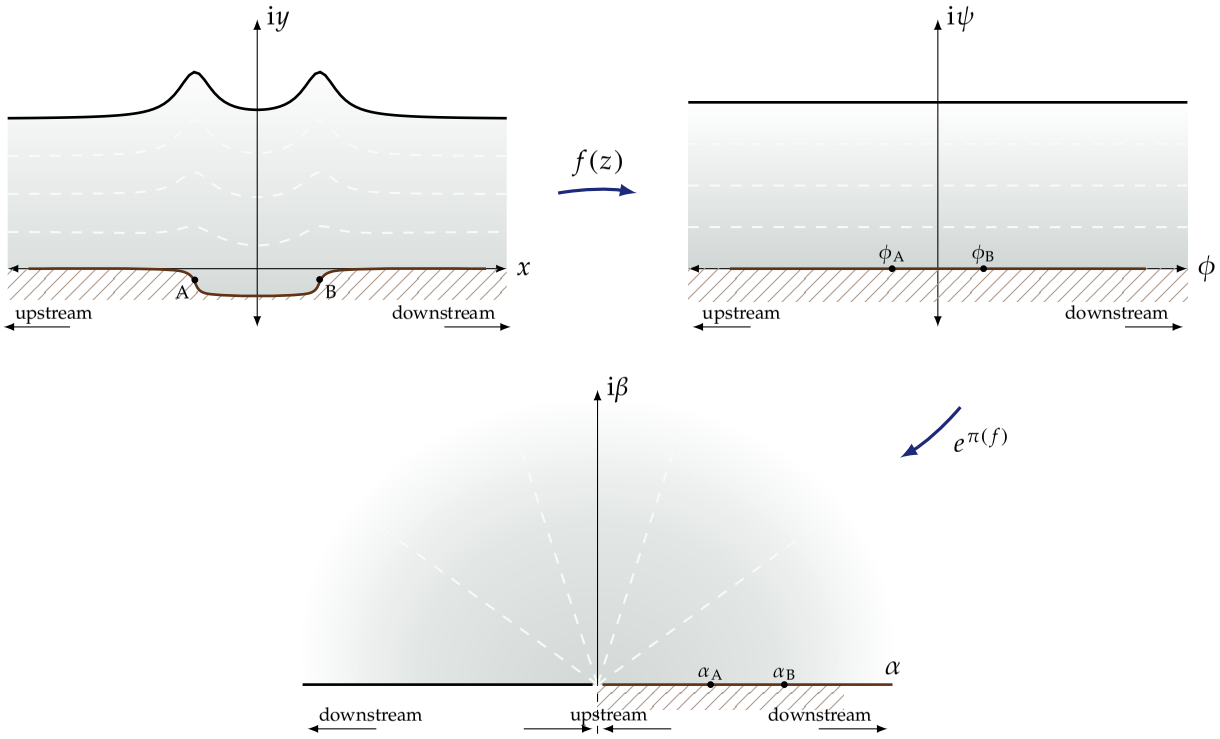

Figure 2.2.2: Diagram of the transform of the flow domain from the $z = x + \mathrm{i}y$ plane to the $\zeta = \alpha + \mathrm{i}\beta$ plane via the complex potential $f = \phi + \mathrm{i}\psi$ plane. Two points along the trench, A and B, are shown with their respective locations ϕ_A and ϕ_B in the f-plane, and α_A and α_B in the ζ-plane.

contain a free constant, which is fixed by letting $\phi = 0$ at $x = 0$. The inflexion points in the physical domain of the trench will be used in Chapter 4 and are indicated as A and B for illustrative purposes here, with corresponding values $f = \phi_A$ and $f = \phi_B$ along the real axis in the f-plane also shown.

Following Vanden-Broeck [66] and later Lustri *et al.* [42] (and references therein), the transformation

$$\zeta = \alpha + \mathrm{i}\beta = e^{\pi f} \tag{2.2.8}$$

is chosen to conformally map the flow domain in the f-plane to the upper half of the ζ-plane, where $\alpha, \beta \in \mathbb{R}$. The flow in the far upstream region is now mapped to the origin, and the far downstream region of the flow is mapped to $|\zeta| \to \infty$. This mapping is shown schematically at the bottom of figure 2.2.2. The bottom of the channel is mapped to the positive segment of the α (real) axis, while the free surface is mapped to negative segment of the α axis. The two inflexion points of the topography are found on the real axis in the ζ-plane, and are located at $\zeta = \alpha_A$ and $\zeta = \alpha_B$ in figure 2.2.2.

The complex velocity $w(\zeta)$ is an analytic function in the domain of the flow in the ζ-plane, it is defined by

$$\frac{\mathrm{d}f}{\mathrm{d}z} = w(\zeta) = u(\zeta) - iv(\zeta). \tag{2.2.9}$$

This expression can be integrated and we use this to find the shape of the free surface, which is given by $z(\zeta) = z(\alpha)$ for $\alpha \in \mathbb{R} > 0$.

We will employ a subscript notation to distinguish a function of ζ from the same quantity expressed as a function of ϕ. The subscript s indicates a flow quantity evaluated on the free surface as a function of ϕ, for example the horizontal component of velocity on the free surface is denoted by $u_s(\phi) = u(-e^{\pi\phi})$. A subscript b indicates a quantity evaluated on the channel floor, for example $u_b(\phi) = u(e^{\pi\phi})$.

Using this notation, integrating (2.2.9), with $\mathrm{d}f = \mathrm{d}\phi$ along a streamline, then equating real and imaginary components yields

$$y_s(\phi) = 1 - \int_{\phi}^{\infty} \frac{v_s(\hat{\phi})}{u_s(\hat{\phi})^2 + v_s(\hat{\phi})^2}\,\mathrm{d}\hat{\phi}, \tag{2.2.10}$$

and

$$x_s(\phi) = \int_{0}^{\phi} \frac{u_s(\hat{\phi})}{u_s(\hat{\phi})^2 + v_s(\hat{\phi})^2}\,\mathrm{d}\hat{\phi}, \tag{2.2.11}$$

where $y_s(\phi) \to 1$ as $\phi \to \infty$ and $x_s(0) = 0$ has been used in the evaluation of the integrals $\int \mathrm{d}z$.

Bernoulli's equation (2.1.7) on the free surface can be written using functions of ϕ as

$$u_s(\phi)^2 + v_s(\phi)^2 + \frac{2}{F^2}\left(y_s(\phi) + p(x_s(\phi)) - 1\right) = 1. \tag{2.2.12}$$

Equations (2.2.10), (2.2.11) and (2.2.12) form a system of three equations for the variables u_s, v_s, x_s, y_s, p and F. One more equation is needed to close the system if F and p are considered known. The Cauchy integral theorem applied to a function which is analytic in the flow domain provides this next equation, and it relates the real and imaginary components of such a function on the boundary of the flow domain. We will now formulate the resulting equation, also known as a Hilbert transform.

2.2.1 Hilbert transform applied to the boundary of the transformed flow domain

Consider a closed contour traversed anti-clockwise, shown schematically in figure 2.2.3, which is contained in the upper half ζ-plane, and is comprised of four segments, labelled $\Gamma_1, \Gamma_2, \Gamma_3$ and Γ_4. The contour, which we will denote as Γ, depends on two positive real parameters ϵ and R, and a coordinate on the real

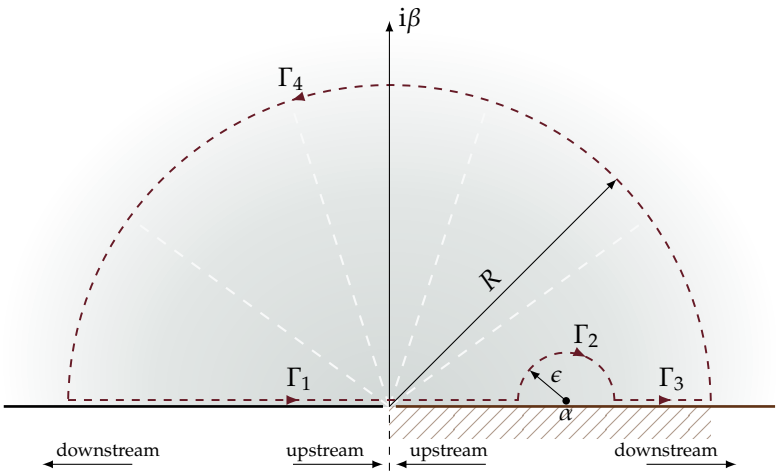

Figure 2.2.3: Diagram of contours $\Gamma_1 \ldots \Gamma_4$ in the $\alpha + \mathrm{i}\beta$ plane used to evaluate the Hilbert transform of a function which is analytic in the upper-half plane.

axis $(\alpha, 0)$ where α is finite. In order for the contour to be simple and closed, it is required that $|\alpha| < R - \epsilon$. The first segment of the contour, Γ_1, is the line segment along the real axis from $(-R, 0)$ to $(\alpha - \epsilon, 0)$. The segment Γ_2 is the circular segment of radius ϵ from $(\alpha - \epsilon, 0)$ to $(\alpha + \epsilon, 0)$, which is in the clockwise sense. Γ_3 is the straight path from $(\alpha + \epsilon, 0)$ to $(R, 0)$. Lastly, Γ_4 is the circular segment of radius R taken anti-clockwise from $(R, 0)$ to $(-R, 0)$.

The Hilbert transform of a function $g(\zeta)$, defined in the upper-half plane, can be written in terms of the contours Γ_1 and Γ_3 by taking the limit as $R \to \infty$ and $\epsilon \to 0$,

$$\begin{aligned}\mathcal{H}(g)(\alpha) &= \frac{1}{\pi} \int_{-\infty}^{\infty} \frac{g(\hat{\alpha})}{\hat{\alpha} - \alpha} \, \mathrm{d}\hat{\alpha} \\ &= \lim_{\substack{\epsilon \to 0 \\ R \to \infty}} \frac{1}{\pi} \left(\int_{\alpha - R}^{\alpha - \epsilon} \frac{g(\hat{\alpha})}{\hat{\alpha} - \alpha} \, \mathrm{d}\hat{\alpha} + \int_{\alpha + \epsilon}^{\alpha + R} \frac{g(\hat{\alpha})}{\hat{\alpha} - \alpha} \, \mathrm{d}\hat{\alpha} \right).\end{aligned}$$

Assuming g is analytic in the upper-half plane and $|\alpha| < R - \epsilon$ (as required), then by Cauchy's integral theorem,

$$\frac{1}{\pi} \int_{\Gamma} \frac{g(\zeta)}{\zeta - \alpha} \, \mathrm{d}\zeta = 0$$

for all ϵ, R. It then follows from the definition of $\mathcal{H}(g)(\alpha)$ above, that an expression for the Hilbert transform using the Γ_2 and Γ_4 contours is given by

$$\mathcal{H}(g)(\alpha) = -\lim_{\substack{\epsilon\to 0\\ R\to\infty}} \frac{1}{\pi}\int_{\Gamma_2+\Gamma_4} \frac{g(\zeta)}{\zeta-\alpha}\,\mathrm{d}\zeta. \tag{2.2.13}$$

These two contour integrals can be evaluated by parameterising the paths of integration. Let Γ_2 be parameterised by $\zeta(\gamma) = \alpha + \epsilon e^{\mathrm{i}\pi(1-\gamma)}$ for $0 < \gamma < 1$. Then the integral over Γ_2 is given by

$$\frac{1}{\pi}\int_{\Gamma_2} \frac{g(\zeta)}{\zeta-\alpha}\,\mathrm{d}\zeta = -\mathrm{i}\int_0^1 g\left(\alpha + \epsilon e^{\mathrm{i}\pi(1-\gamma)}\right)\,\mathrm{d}\gamma. \tag{2.2.14}$$

Similarly, by parameterising Γ_4 as $\zeta(\gamma) = Re^{\mathrm{i}\pi\gamma}$ for $0 < \gamma < 1$, then

$$\frac{1}{\pi}\int_{\Gamma_4} \frac{g(\zeta)}{\zeta-\alpha}\,\mathrm{d}\zeta = \mathrm{i}\int_0^1 \frac{g(Re^{\mathrm{i}\pi\gamma})Re^{\mathrm{i}\pi\gamma}}{Re^{\mathrm{i}\pi\gamma}-\alpha}\,\mathrm{d}\gamma. \tag{2.2.15}$$

We define the transform $\mathcal{I}$ of the function g as

$$\mathcal{I}(g) = -\mathrm{i}\lim_{R\to\infty}\int_0^1 \frac{g(Re^{\mathrm{i}\pi\gamma})Re^{\mathrm{i}\pi\gamma}}{Re^{\mathrm{i}\pi\gamma}-\alpha}\,\mathrm{d}\gamma. \tag{2.2.16}$$

Provided the limit as $\epsilon \to 0$ and $R \to \infty$ exists for equations (2.2.13)–(2.2.16), the Hilbert transform of the function g evaluated at α is equal to a complex rotation of $g(\alpha)$ by $\pi/2$ plus a constant,

$$\mathcal{H}(g)(\alpha) = \mathcal{I}(g) + \mathrm{i}g(\alpha). \tag{2.2.17}$$

The following lemma is a near-direct consequence of the estimation lemma, also known as the M-L inequality [5], which we use in the next step of the formulation.

Lemma 1. *If $g(\zeta)$ vanishes at infinity, then*

$$\mathcal{I}(g) = 0.$$

Proof. Let $z = Re^{i\theta}$ and $w = A + iB$, then

$$\begin{aligned} |z - w|^2 &= (R\cos\theta - A)^2 + (R\sin\theta - B)^2 \\ &= A^2 + B^2 - 2R(A\cos\theta + B\sin\theta) + R^2 \\ &\geq R^2 - 2R(A\cos\theta + B\sin\theta). \end{aligned}$$

It follows that if

$$R^2(1 - \delta^2) - 2R(A\cos\theta + B\sin\theta) \geq 0$$

for $0 < \delta < 1$ in some region $R \geq \hat{R}$, then $|z - w| > \delta R$ for $R \geq \hat{R}$. The zeros of the polynomial in R from the left-hand-side of the inequality above are $R = 0$ and $R = 2(A\cos\theta + B\sin\theta)/(1 - \delta^2)$. Let

$$\hat{R} = \max\left(0, \frac{2(A\cos\theta + B\sin\theta)}{1 - \delta^2}\right).$$

Now for any δ between 0 and 1, there is a finite number $\hat{R}$ such that for $R \geq \hat{R}$,

$$|z - w| \geq \delta R. \tag{2.2.18}$$

Now return to the absolute value of the integral in (2.2.16);

$$\begin{aligned} \left|\int_0^1 \frac{g(Re^{i\pi\gamma})Re^{i\pi\gamma}}{Re^{i\pi\gamma} - \alpha}\,\mathrm{d}\gamma\right| &\leq \int_0^1 \left|\frac{g(Re^{i\pi\gamma})Re^{i\pi\gamma}}{Re^{i\pi\gamma} - \alpha}\right|\mathrm{d}\gamma \\ &\leq \frac{1}{\delta}\int_0^1 \left|g(Re^{i\pi\gamma})\right|\mathrm{d}\gamma \end{aligned}$$

for all $R \geq \hat{R}$, by letting $w = \alpha$ in (2.2.18). Applying the estimation lemma to the above yields

$$\frac{1}{\delta}\int_0^1 \left|g(Re^{i\pi\gamma})\right|\mathrm{d}\gamma \leq \frac{1}{\delta}\max_{\gamma\in[0,1]}|g(Re^{i\pi\gamma})|$$

for all $R \geq \hat{R}$. As $\lim_{R\to\infty} g(Re^{i\pi\gamma}) = 0$ by assumption, it follows by the squeeze theorem that $\mathcal{I}(g) = 0$. □

If $g(\zeta)$ vanishes at infinity in (2.2.17), then by equating real components and using Lemma 1, it can be shown that

$$\mathrm{Re}\left(g(\alpha)\right) = \frac{1}{\pi} \fint_{-\infty}^{\infty} \frac{\mathrm{Im}\left(g(\hat{\alpha})\right)}{\hat{\alpha} - \alpha} \, \mathrm{d}\hat{\alpha}. \tag{2.2.19}$$

Breaking the domain of integration into $\hat{\alpha} > 0$ and $\hat{\alpha} < 0$, and using the substitutions $\hat{\alpha} = \mp e^{\pi\hat{\phi}}$ respectively, along with $\alpha = -e^{\pi\phi}$ on the free surface, the integral from the expression (2.2.19) can be written in terms of functions of ϕ using the s and b subscript notation from earlier:

$$\mathrm{Re}\left(g_s(\phi)\right) = -\underbrace{\fint_{-\infty}^{\infty} \frac{\mathrm{Im}\left(g_s(\hat{\phi})\right)}{e^{\pi\hat{\phi}} - e^{\pi\phi}} e^{\pi\hat{\phi}} \, \mathrm{d}\hat{\phi}}_{\text{contribution from surface}} + \underbrace{\int_{-\infty}^{\infty} \frac{\mathrm{Im}\left(g_b(\hat{\phi})\right)}{e^{\pi\hat{\phi}} + e^{\pi\phi}} e^{\pi\hat{\phi}} \, \mathrm{d}\hat{\phi}}_{\text{contribution from channel floor}}. \tag{2.2.20}$$

The real part of a quantity on the bottom of the channel can similarly be related to the imaginary part on the whole boundary; for this again, split the integral domain and let $\hat{\alpha} = \mp e^{\pi\hat{\phi}}$ as required, along with $\alpha = e^{\pi\phi}$ in (2.2.19), and

$$\mathrm{Re}\left(g_b(\phi)\right) = -\int_{-\infty}^{\infty} \frac{\mathrm{Im}\left(g_s(\hat{\phi})\right)}{e^{\pi\hat{\phi}} + e^{\pi\phi}} e^{\pi\hat{\phi}} \, \mathrm{d}\hat{\phi} + \fint_{-\infty}^{\infty} \frac{\mathrm{Im}\left(g_b(\hat{\phi})\right)}{e^{\pi\hat{\phi}} - e^{\pi\phi}} e^{\pi\hat{\phi}} \, \mathrm{d}\hat{\phi}. \tag{2.2.21}$$

The remaining equation for solving the free surface, given (2.2.10)–(2.2.12), is found by the choice of the function $g(\zeta)$.

2.2.1.1 Flow past a pressure disturbance

For a flow with a pressure disturbance, let $g(\zeta) = (u(\zeta) - 1) + iv(\zeta)$, which is a function representing the complex velocity minus the fluid velocity far downstream and upstream. This function will vanish as $\zeta \to \infty$, see Appendix D, so we can use (2.2.20). As the channel is flat, $v_b(\phi) = 0$, and so (2.2.20) is now

$$u_s(\phi) = 1 + \fint_{-\infty}^{\infty} \frac{v_s(\hat{\phi})}{e^{\pi\hat{\phi}} - e^{\pi\phi}} e^{\pi\hat{\phi}} \, \mathrm{d}\hat{\phi}. \tag{2.2.22}$$

Equation (2.2.22) combined with (2.2.10)–(2.2.12) forms a system of four equations, with unknowns u_s, v_s, x_s and y_s for any choice of parameter F and known p, and so the system is closed.

2.2.1.2 Flow past a topographical disturbance

For a topographical disturbance $v_b \neq 0$ in general, and so a more convenient formulation is to follow Binder & Vanden-Broeck [9], Lustri *et al.* [42], Vanden-Broeck [66] and others and let $g(\zeta) = \tau(\zeta) - i\theta(\zeta)$, defined by the transform of the complex velocity

$$u(\zeta) - iv(\zeta) = e^{\tau(\zeta) - i\theta(\zeta)}. \tag{2.2.23}$$

For fixed topography, $\theta_b(\phi)$ is considered known, so (2.2.20) becomes

$$\tau_s(\phi) = \fint_{-\infty}^{\infty} \frac{\theta_s(\hat{\phi})e^{\pi\hat{\phi}}}{e^{\pi\hat{\phi}} - e^{\pi\phi}}\,\mathrm{d}\hat{\phi} - \int_{-\infty}^{\infty} \frac{\theta_b(\hat{\phi})e^{\pi\hat{\phi}}}{e^{\pi\hat{\phi}} + e^{\pi\phi}}\,\mathrm{d}\hat{\phi}. \tag{2.2.24}$$

For a topographical disturbance the unknowns are τ_s, θ_s, x_s and y_s for a given F and σ, while p is assumed to be zero everywhere. Equation (2.2.24) along with (2.2.10)–(2.2.12) then form a system of four equations in the four unknowns.

The solutions are not known in general for both these systems of integral equations, either (2.2.10)–(2.2.12) combined with (2.2.22) or (2.2.24) for a pressure disturbance or a topographical disturbance respectively. To find solutions, Vanden-Broeck & Schwartz [67], Forbes & Schwartz [23], Vanden-Broeck [66] derive a system of algebraic equations by combining domain truncation, discretisation of the ϕ-coordinate, removing the singularity in the integrals (2.2.22) or (2.2.24) and applying simple integration rules such as the mid-point or trapezoidal rule to evaluate all integrals. The free surface is then solved on the discrete grid numerically using an iterative solver, with the majority of the system of equations being given by the free-surface dynamic boundary condition (2.2.12) evaluated on the discrete grid, combined with other boundary or flow conditions to ensure a closed system. Here, the domain of the integral in equations (2.2.22) or (2.2.24) is truncated to $[\phi_a, \phi_b]$, for some choice of ϕ_a and ϕ_b such that the error introduced by the truncation is small.

2.3 Numerical method for boundary integrals

2.3.1 Irregular grid

Hunter & Vanden-Broeck [30] computed very steep solitary waves using a boundary-integral method which clustered the grid points near the peak of the wave. This was achieved by introducing a change of variables $\phi = \varphi(\beta)$ in the integrals. Hunter & Vanden-Broeck [30] used $\varphi(\beta) \sim \beta^3$ to cluster the grid points near the location of the crest at $\phi = 0$, where the shape of the free surface varies rapidly for small changes in ϕ. In order to efficiently compute the entire range of waves and those with multiple crests, this idea is extended here to a piecewise-cubic polynomial, so that the transform φ with a regular discretisation in the new variable β will cluster the grid points near the crest(s) of the flow in the physical coordinates; especially for those regions of the parameter space where the wave gets steeper. We refer to this type of grid throughout as an 'irregular' grid, as it is an irregular computational grid in the variable for which most of our formulation is given, ϕ. In the usual sense, however, the grid is regular in the β variable.

The intervals of the piecewise-cubic polynomial are defined by either the location of a crest or an endpoint of the truncated integral. An endpoint of an interval will be denoted $\phi_{[j]}$, for $j = 1, \ldots, M+1$ where M is the number of intervals of the piece-wise function. Here $\phi_{[1]} = \phi_a$ is the value at left end-point of the truncated profile, and $\phi_{[M+1]} = \phi_b$ is the right end-point. Values of $\phi_{[j]}$ from $j = 2, \ldots, M$ are the locations of the crests.

Define the piecewise polynomial φ as

$$\varphi(\beta) = \varphi_{[j]}(\beta) \quad \text{for } \beta \in (\beta_{[j]}, \beta_{[j+1]}), \tag{2.3.25}$$

where $\varphi_{[j]}$ is defined by

$$\varphi_{[j]}(\beta) = (1-s)\left[\phi_{[j]}m_{[j]}(\beta) + \phi_{[j+1]}n_{[j]}(\beta)\right] + s\left[\phi_{[j]}a_{[j]}(\beta) + \phi_{[j+1]}b_{[j]}(\beta) + \lambda_{[j]}c_{[j]}(\beta) + \lambda_{[j+1]}d_{[j]}(\beta)\right].$$

Here the $\beta_{[j]}$ are values of β chosen at the endpoints of an interval, determined later to ensure monotonicity of the transform, and $\lambda_{[j]}$ are chosen so that the slope of the polynomial is small near endpoints where clustering is desired, i.e. at the crests of steep waves. As s varies from 0 to 1, φ varies from a piecewise-linear function to a piecewise-cubic function, shown in figure 2.3.4. When $s = 0$ the grid is based on linear interpolation from $(\beta_{[j]}, \phi_{[j]})$ and $(\beta_{[j+1]}, \phi_{[j+1]})$ within each interval, which implies no clustering occurs near the locations $\phi_{[j]}$. For $s = 1$ the grid is based on cubic polynomial interpolation, and clustering is present near $\phi_{[j]}$ if the value of $\lambda_{[j]}$ is taken to be small. In brief, all computations presented in Chapters 3 and 4 are shown with $s = 1$. The reason for introducing the piecewise-linear grid is that in some calculations a low resolution solution was interpolated onto a higher resolution grid, then the higher resolution surface was found for $s = 0$ and then, by numerical continuation, determined for $s = 1$.

The linear interpolant is constructed from basis functions $m_{[j]}$ and $n_{[j]}$, where $m_{[j]}(\beta_{[j]}) = 1$ and $m_{[j]}(\beta_{[j+1]}) = 0$, while $n_{[j]}$ is defined such that $n_{[j]}(\beta_{[j]}) = 0$ and $n_{[j]}(\beta_{[j+1]}) = 1$. Explicitly,

$$m_{[j]}(\beta) = -\frac{\beta - \beta_{[j+1]}}{\Delta\beta_{[j]}} \text{ and}$$
$$n_{[j]}(\beta) = \frac{\beta - \beta_{[j]}}{\Delta\beta_{[j]}},$$

where $\Delta\beta_{[j]} = \beta_{[j+1]} - \beta[j]$.

The cubic polynomial on each interval $(\beta_{[j]}, \beta_{[j+1]})$ is the unique cubic polynomial that passes through the points $(\beta_{[j]}, \phi_{[j]})$ and $(\beta_{[j+1]}, \phi_{[j+1]})$ and has slope $\lambda_{[j]}$ at each $\beta_{[j]}$. This polynomial is constructed from basis functions which are

relatively easy to determine for any choice of $\beta_{[j]}$, $\beta_{[j+1]}$, $\phi_{[j]}$, $\phi_{[j+1]}$, $\lambda_{[j]}$, and $\lambda_{[j+1]}$. The basis functions of the piecewise-cubic interpolating polynomial are;

$$a_{[j]}(\beta) = 2\frac{(\beta - \beta_{[j+1]})^2(\beta - \beta_{[j]} + \Delta\beta_{[j]}/2)}{{\Delta\beta_{[j]}}^3},$$
$$b_{[j]}(\beta) = -2\frac{(\beta - \beta_{[j]})^2(\beta - \beta_{[j]} - \Delta\beta_{[j]}/2)}{{\Delta\beta_{[j]}}^3},$$
$$c_{[j]}(\beta) = \frac{(\beta - \beta_{[j]})^2(\beta - \beta_{[j+1]})}{{\Delta\beta_{[j]}}^2} \text{ and}$$
$$d_{[j]}(\beta) = \frac{(\beta - \beta_{[j]})(\beta - \beta_{[j+1]})^2}{{\Delta\beta_{[j]}}^2}.$$

These are shown in the overlay cut-out in figure 2.3.4, where the purpose of each basis function can be inferred by whether its value or slope is zero or one at a given endpoint.

The intervals are sub-divided using a regular grid over an arbitrary domain in β. For convenience we let $\beta_i = i$ for $i = 0, 1, \ldots, N$, where N is the total number of grid points (or sub-intervals). In figure 2.3.4, the effect of the clustering when $\lambda_{[j]}$ is small is shown by considering a unit change in β at two different locations $\beta = i_0$ and $\beta = i_1$, and the corresponding change in ϕ denoted by $\Delta\phi_{i_0}$ and $\Delta\phi_{i_1}$ is shown in blue on the left-hand vertical axis.

The choice of $\beta_{[j]}$ determines the number of grid points within each interval of the piecewise transform. In order to avoid low sampling near a segment with high curvature, we aim to keep $z_s(\varphi(\beta_{i+1})) - z_s(\varphi(\beta_i))$ roughly constant. Using the definition of the complex velocity, and knowing that v_s is generally small compared to u_s, we choose

$$\beta_{[j+1]} - \beta_{[j]} = \frac{N-1}{\sum_{k=1}^{M} \Delta\phi_{[k]} \left(u_s(\phi_{[k+1]}) + u_s(\phi_{[k]})\right)^{-1}} \Delta\phi_{[j]} \left(u_s(\phi_{[j+1]}) + u_s(\phi_{[j]})\right)^{-1}$$

with $\beta_{[1]} = 0$. This ensures enough grid points within each segment such that, clustering details aside, the grid will be close to regular in the physical coordinates,

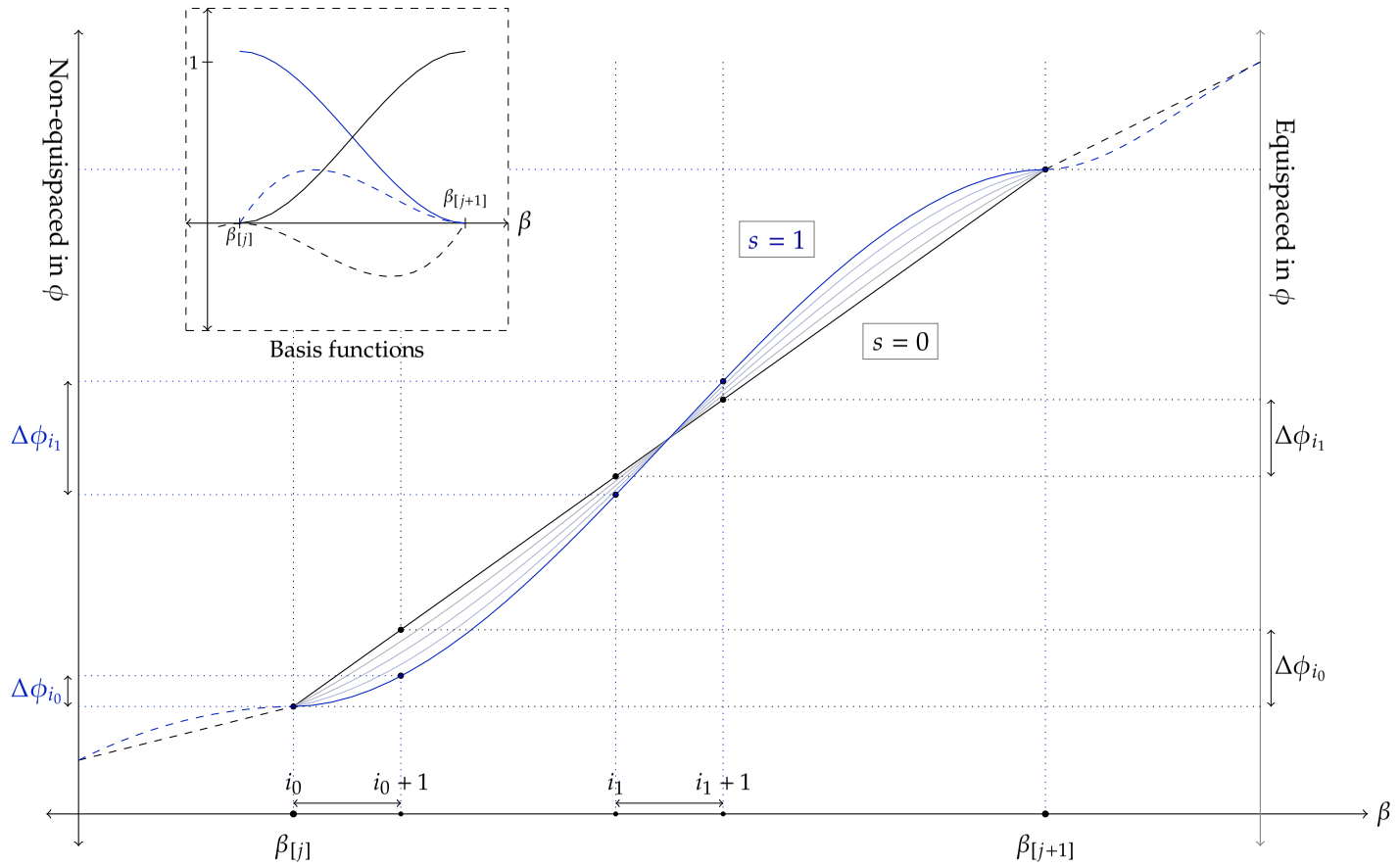

Figure 2.3.4: Sketch of the computational grid; here a blue line shows $\varphi(\beta)$ for $s = 1$, and a black line shows $\varphi(\beta)$ for $s = 0$. The basis functions are shown in the overlay with a blue solid line for $a_{[j]}$, a black solid line for $b_{[j]}$, a blue dashed line for $c_{[j]}$ and a black dashed line for $d_{[j]}$.

even though clearly irregular in ϕ.

The values of $\lambda_{[j]}$ drive the clustering, and are taken such that clustering occurs when the velocity near the crests is small, i.e. $\lambda_{[j]}$ must become small as $u_s(\phi_{[j]}) \to 0$. In addition, the coefficients $\lambda_{[j]}$ should ensure that the derivative $\varphi'(\beta)$ is non-zero, as a value of zero will adversely effect the Jacobian of the algebraic systems of equations which we must solve, presented later. For this reason $\lambda_{[j]}$ is taken to be

$$\lambda_{[j]} = u_s(\phi_{[j]})^2\gamma_1 + (1 - u_s(\phi_{[j]}))^2\gamma_2. \tag{2.3.26}$$

The coefficient $\gamma_1 = (\phi_b - \phi_a)/(N-1)$ is used to ensure that the spacing is close to that of a regular grid when $u_s(\phi_{[j]}) \approx 1$. We take $\gamma_2 = \delta\gamma_1$ for some small $\delta \approx 0.01$, so that the grid is clustered near the crest if $u_s(\phi_{[j]}) \approx 0$.

2.3.1.1 Monotonicity

When $s = 0$ each $\varphi_{[j]}(\beta)$ is monotonic, as is the whole transform $\varphi(\beta)$. For the cubic polynomial (when $s \neq 0$), the monotonicity of each $\varphi_{[j]}(\beta)$ depends largely on $u_s(\phi_{[j]})$ and $u_s(\phi_{[j+1]})$, and the choice of δ. Monotonicity can be established in the case $s = 1$ if the derivative of $\varphi'_{[j]}(\beta)$ is always positive. Firstly, since $\lambda_{[j]}$ is positive, then the values of $\varphi'_{[j]}(\beta)$ at the endpoints of the intervals are positive. Noting also that $\varphi'_{[j]}(\beta)$ is a quadratic, then provided the coefficient of the β^2 term is negative, then the quadratic will be positive on its domain. Now consider the coefficient of the β^2 term in $\varphi'_{[j]}(\beta)$,

$$\frac{3}{(\beta_{[j+1]} - \beta_{[j]})^2}\left(\lambda_{[j]} + \lambda_{[j+1]} - \frac{\phi_{[j+1]} - \phi_{[j]}}{\beta_{[j+1]} - \beta_{[j]}}\right),$$

from which it can be shown that $\varphi_{[j]}(\beta)$ is monotonic provided

$$\lambda_{[j]} + \lambda_{[j+1]} < \frac{\phi_{[j+1]} - \phi_{[j]}}{\beta_{[j+1]} - \beta_{[j]}}. \tag{2.3.27}$$

The right-hand-side is clearly positive given the definition of $\phi_{[j]}$ and $\beta_{[j]}$. Assuming $u_s(\phi_{[j]}) \leq 1$ then the right-hand-side obeys the following inequality;

$$\frac{\phi_{[j+1]} - \phi_{[j]}}{\beta_{[j+1]} - \beta_{[j]}} \geq \frac{\phi_b - \phi_a}{N-1} \left(u_s(\phi_{[j+1]}) + u_s(\phi_{[j]}) \right) .$$

Using this as a lower bound on the right-hand-side in (2.3.27), it follows that if

$$\lambda_{[j]} + \lambda_{[j+1]} - \frac{\phi_b - \phi_a}{N-1} \left(u_s(\phi_{[j+1]}) + u_s(\phi_{[j]}) \right) \leq 0 \tag{2.3.28}$$

holds, then (2.3.27) also holds. A contour plot of the left-hand part of the inequality (2.3.28) is shown in figure 2.3.5 for $\delta = 0.01$ and $-\phi_a = \phi_b = 12$. From the chosen form of $\lambda_{[j]}$ there is a factor $(\phi_b - \phi_a)/(N-1)$ throughout the expression, thus ϕ_a, ϕ_b and N do not affect the domain where the inequality above holds. There are small regions in three corners in figure 2.3.5 where the inequality (2.3.28) does not hold, and although the area (or extent) of these regions can be reduced by choosing smaller δ, this is generally not necessary as the condition is only a sufficient condition, and in all computations performed the transform $\varphi(\beta)$ behaved in a monotonic fashion for all δ used.

2.3.2 Numerical error in evaluating the Cauchy principal value integral

In Appendix B the error in numerically evaluating a Cauchy principal value integral by removing the singularity and applying the trapezoidal rule is determined. Noble & Beighton [48] found that the error for a certain class of Cauchy principal value integrals is second order in the grid spacing and bounded under certain conditions. This proof is extended to the Cauchy principal value integrals such as (2.2.22) and (2.2.24) which have a change of variables $\phi = \varphi(\beta)$, a case not explicitly considered by Noble & Beighton [48]. Corollary 2 in the appendix shows the error is bounded and second order in the grid spacing provided both $v(\alpha)$ (or $\tau(\alpha)$) and the change of variables for the irregular grid are sufficiently differentiable.

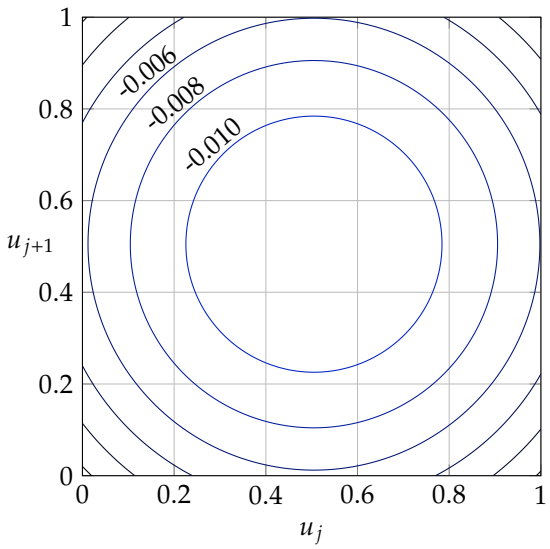

Figure 2.3.5: Contours of the value of the left-hand side of inequality (2.3.28) for $\delta = 0.01$ and $-\phi_a = \phi_b = 12$.

2.4 Numerical continuation procedure

The precise details of the system of equations are dependent upon the problem, and these are detailed in Chapters 3 and 4. All the solutions to the fully nonlinear problem are obtained by using the predictor-corrector method of Allgower & Georg [3] in order to obtain one-parameter families of solutions (or branches) in an automated fashion. The predictor-corrector method requires an underdetermined system which has one more unknown than equations; this differs from the usual approach of using Newton's method on an exactly determined system.

The one-parameter family of solutions can be thought of as the kernel of a smooth map. Let $H : \mathbb{R}^{N+1} \to \mathbb{R}^N$ be a smooth map, and let $\mathbf{x}_0$ be a regular point of the map, i.e. a point $\mathbf{x}_0$ where the Jacobian of the map, denoted H', has maximum rank, N. The solution to the system is given by the curve $\mathbf{x}(s)$, where s is the arclength, which satisfies

$$H(\mathbf{x}(s)) = 0, \tag{2.4.29}$$

and

$$H'(\mathbf{x})\dot{\mathbf{x}} = 0, \quad \|\dot{\mathbf{x}}\| = 1, \quad \text{and} \quad \mathbf{x}(0) = \mathbf{x}_0. \tag{2.4.30}$$

As a simple example, if the system of equations was a single equation say $x^2 + y^2 - 1 = 0$, then $H(x, y) : \mathbb{R}^2 \to \mathbb{R}^1$ would be given by $H(x, y) = x^2 + y^2 - 1$.

Let $\mathbf{x}_0, \mathbf{x}_1, \mathbf{x}_2, \ldots$ be a sequence of vectors in $\mathbb{R}^{N+1}$. The numerical procedure uses the QR factorisation $H'(\mathbf{x}_n)^* = Q_n R_n$. The Jacobian H' is estimated using a simple finite-difference approximation.

Let the vectors $\mathbf{q}_{n,j}$ be the column vectors of $Q = [\mathbf{q}_{n,0}, \ldots, \mathbf{q}_{n,j}, \ldots, \mathbf{q}_{n,N+1}]$. The first vector $\mathbf{x}_1$ is a predictor for $\mathbf{x}(h)$ and is given by

$$\mathbf{x}_1 = \mathbf{x}_0 \pm h\mathbf{q}_{0,N+1},$$

where h is a step-size, and the $\pm$ branch is chosen depending upon the sign of $\det(Q_n)\det(R_n)$. The details of how to calculate the sign, and how $\mathbf{q}_{0,N+1}$ corresponds to the tangent induced by H' are given in Allgower & Georg [3].

A sequence of corrector steps is then employed which generates $\mathbf{x}_2, \mathbf{x}_3, \ldots$ until $H(\mathbf{x}_n)$ is less than some chosen tolerance. The vectors $\mathbf{x}_n$ are defined by a recurrence relation, which is evaluated by solving first for $\mathbf{y}_n$ by backward substitution, first calculate

$$R_n^* \mathbf{y}_n = H(\mathbf{x}_n)$$

and then evaluate $\mathbf{x}_{n+1}$ given

$$\mathbf{x}_{n+1} = \mathbf{x}_n - Q_n \mathbf{y}_n.$$

Once this process has converged at n steps, then $\mathbf{x}_n \approx \mathbf{x}(h)$, which may also be a regular point of the map. The arclength between $\mathbf{x}_0$ and $\mathbf{x}_n$ will be approximately h. The process of predicting and correcting can then be repeated to determine the image of $\mathbf{x}(s)$ at discrete locations with approximately even spacing of h in terms of the parameter s.

2.5 Weakly non-linear dimensionless flow model

The continuation procedure in §2.4 will be applied to a discretised version of the system described at the end of §2.2.1. As the shape of the free surface is to be determined numerically, the number of free parameters in the problem is an important consideration, as it is not clear due to the system's nonlinear nature. A weakly nonlinear model can be used to provide a parametric map of the solutions in the region in which the weakly nonlinear theory is valid [18]. The weakly nonlinear theory given by Akylas [2] and Grimshaw & Smyth [27] is used here, who derived the forced Korteweg & de Vries (fKdV) equation [33] for time dependent and near critical flow past either a pressure disturbance or a topographical forcing.

The fKdV equation is derived in Appendix C using long wavelength asymptotics. It follows closely the derivation given in Shen [54]. The variables are rescaled by assuming there is a characteristic length L (e.g. a length related to wavelength) such that $(H/L)^2 = \epsilon \ll 1$ and that the free surface is of $\mathrm{O}(\epsilon)$. The other scalings are found by balancing the leading order terms and using the result given by Akylas [2] that the topographic forcing or pressure forcing must be $\mathrm{O}\left(\epsilon^2\right)$. By matching terms of the same order in ϵ the fKdV equation is derived. When written in terms of the variables used in the nonlinear computations the fKdV equation is

$$6\eta_t - \eta_{xxx} - 9\eta\eta_x + 6(F-1)\eta_x = 3(p_x + \sigma_x). \tag{2.5.31}$$

This is referred to as the time-dependent fKdV equation, and is the model used in the stability analysis in Chapter 5. The steady forced KdV is introduced next, which we use for classification and comparison in the next two chapters.

2.5.1 Steady forced KdV

Given the flow is steady, the integrated form of the fKdV equation (2.5.31) is

$$\eta_{xx} + \frac{9}{2}\eta^2 - 6(F-1)\eta = -3(p+\sigma), \tag{2.5.32}$$

where the limits $p, \eta, \sigma \to 0$ as $x \to \infty$ have been used. According to this equation, the pressure and topographical disturbances should have the same solutions at this order of approximation, or in other words the two types of forcing produce an equivalent physical response in the system. At higher order the equivalence of the two types of disturbance no longer holds, for example and additional dispersive term due to topographical forcing appears in the generalized-Boussinesq model of Lee *et al.* [36] that does not appear in the fKdV equation. In spite of this, the fKdV model is very accurate for disturbances that are not larger than about half the downstream free-surface height [55].

If the magnitude of the disturbance is sufficiently small and the disturbances have compact support, then they can be modelled by the $\delta(x)$ function. This is valid provided the amplitude parameter $A \sim \epsilon^{3/2}$. There is also a range, or scale, of validity for the parameters that affect the support, namely B and l, for a Gaussian (2.1.2) or the smooth disturbances using hyperbolic functions (2.1.3) respectively. For Gaussian disturbances, $B/\sqrt{\pi} \sim \epsilon^{1/2}$, and for the hyperbolic tangent based disturbances, $l \sim \epsilon^{-1/2}$. Using the long-wavelength scaled variables and these scales for the parameters, it follows that the disturbance approaches $\delta(x)$ as $\epsilon \to 0$. By integration in the scaled variables and then reverting back to the unscaled variables, the following equations govern the free surface;

$$\eta_{xx} + \frac{9}{2}\eta^2 - 6(F-1)\eta = 0 \qquad \text{for } x \neq 0; \text{ and} \tag{2.5.33}$$

$$\eta_x(0^+) - \eta_x(0^-) = -3A. \tag{2.5.34}$$

In the unforced regime where $A = 0$ this dynamical system has two fixed points when $F > 1$. These fixed points are located at $(0,0)$ and $(4(F-1)/3, 0)$ in the

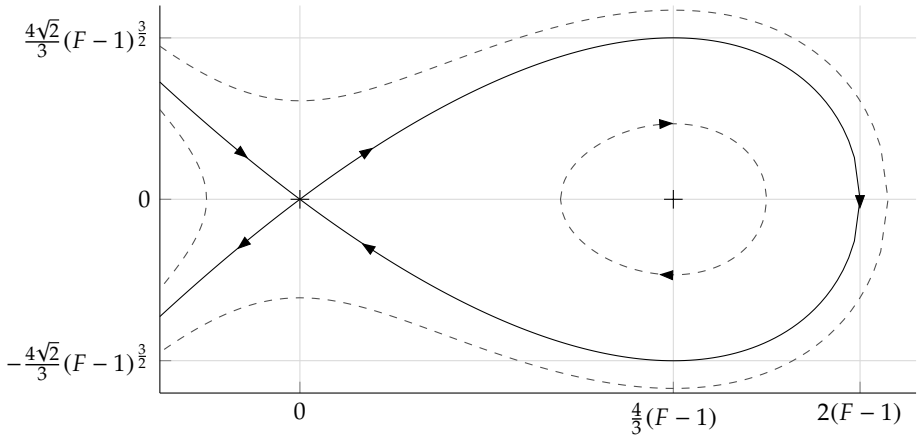

Figure 2.5.6: KdV phase portrait, + indicates the fixed points, saddle at origin and centre at $\eta = \frac{4}{3}(F-1)$. A solid line indicates unstable/stable sets of the fixed point at the origin and the dashed lines show a periodic orbit about the centre and two unbounded trajectories.

(η, η_x)-phase plane; and a linear stability analysis around these fixed points shows that they are a saddle and a centre respectively. The solution in the phase plane can be obtained by integrating equation (2.5.33) again, which gives

$$(\eta_x)^2 + 3\eta^3 - 6(F-1)\eta^2 = \begin{cases} C_{\text{up}} & x < 0, \\ 0 & x > 0, \end{cases} \tag{2.5.35}$$

where C_{up} is the upstream constant, and the downstream constant must be taken to be zero to satisfy $\eta, \eta_x \to 0$ as $x \to \infty$. The contours of (2.5.35) are used to determine the possible trajectories in the phase plane shown in figure 2.5.6, these include periodic orbits, unbounded trajectories and a homoclinic orbit enclosing the origin.

For either unforced or forced solutions, the trajectory in the phase plane must contain an interval of the stable manifold of the origin which includes the origin in order to satisfy the downstream far-field condition. If the (non-trivial) solution is unforced ($A = 0$) there is only one way of achieving this, namely by traversing

the homoclinic (or solitary wave) orbit in a clockwise direction in the phase plane as shown in figure 2.5.6.

When forcing is present, equation (2.5.34) introduces a vertical jump in the phase plane, which provides a way of transitioning between fixed points and the various trajectories in the phase plane. In this weakly nonlinear model such forced solutions are described by two parameters; the Froude number F fixes the qualitative behaviour of the solutions in the phase plane and the amplitude of forcing A determines the size of the jump in the phase plane. For given values of A and F (and $A \neq 0$), the location of the jump in the phase-plane determines the solution. Fixing F and allowing A to be free parameter will therefore admit one-parameter families of solutions in the $(A, \eta(0))$ plane.

The next two chapters contain the results for the free surface using the boundary-integral and continuation methods discussed in this chapter. We present the one-parameter families of solutions for the fully nonlinear problems, using the weakly nonlinear model for both comparison and classification.

Chapter 3

Waves past a localised pressure disturbance

3.1 Introduction

The solution space of almost-highest waves subject to a pressure disturbance is presented in this chapter. The topography is assumed flat, shown schematically in figure 3.1.1, and the symmetric pressure disturbance is given by (2.1.2). Only supercritical flow for which $F > 1$ is considered, where the linear theory predicts

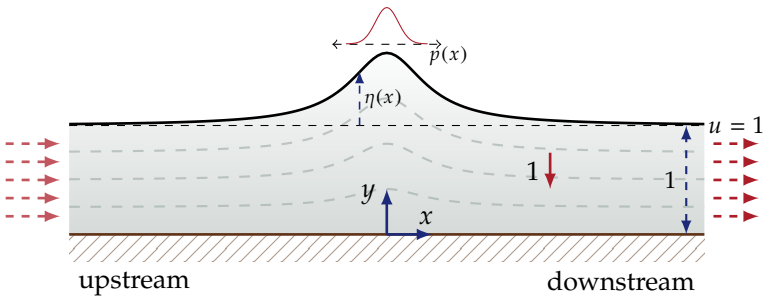

Figure 3.1.1: Schematic of the flow considered in this chapter, with flat topograhy and pressure disturbance given by (2.1.2), with symmetry about $x = 0$.

that the steady solutions are symmetric (due to the symmetry of pressure disturbance on the free surface), see for example Stoker [57]. This symmetry is then applied to the formulation so that only symmetric waves for the fully nonlinear model need to be considered. The specific details of the numerical procedure for finding solutions to the fully nonlinear model are given in §3.2, following on from the procedures outlined in the previous chapter.

As discussed in the introduction, an analysis of the weakly nonlinear phase plane of the fKdV model provides a systematic way of identifying and classifying the (fully) nonlinear solutions of the unforced system, as either a perturbation to a uniform stream or a solitary wave (or waves). This classification scheme has been applied to flows past topographical disturbances [15, 23, 65], and we present this classification for both the weakly nonlinear and fully nonlinear solutions to the flow past a pressure disturbance studied here. Further detailed discussion of the fKdV model and its solutions may be found in Baines [4] and Ee *et al.* [19, 20].

In §3.3 we show that as wave-height increases, all fully nonlinear waves that are classified as perturbations to solitary waves approach the Stokes limiting wave with an included angle of 120° and a stagnation point at the crest of the wave. These limiting configurations are not predicted by the weakly nonlinear model, and so the solution space between the two models differs considerably, in particular as the wave-height or Froude number increases. We also find a new fully nonlinear solution which is not predicted by the weakly nonlinear theory. This fully nonlinear solution does not display the presence of a cusp as per the corresponding solution to the weakly nonlinear model.

Like the unforced waves investigated previously by Longuet-Higgins & Fox [40] and Maklakov [43], we show that many properties of the forced waves are not unique with respect to the height of the wave as the limiting configuration is approached in §3.3.2. We also present an analysis of the cusped solutions as they

approach the limiting configuration, where the limiting configuration is rotated slightly. The findings are summarised and discussed in the concluding remarks in §3.4.

3.2 Formulation

For this problem the boundary integral relating $u_s(\phi)$ to $v_s(\phi)$ in (2.2.22) is used to form the system of equations for which the free-surface is found as a solution (rather than (2.2.24) which relates τ_s and θ_s). This approach was chosen as it allows a significant simplification to the contribution from the far-field by substituting Stokes' result (see, for example, [11] and [30]) for the velocity; this is derived in Appendix D, and given by (D.11).

As only symmetric waves are considered, we can exploit this symmetry to write

$$v_s(-\phi) = -v_s(\phi) \quad \text{and} \quad u_s(\phi) = u_s(-\phi),$$

so that the integral (2.2.22) is given, by an appropriate change of variables, as

$$u_s(\phi) = 1 + \frac{1}{2}\int_0^\infty G(\phi,\hat{\phi})\,\mathrm{d}\hat{\phi} \quad \text{for } -\infty < \phi < \infty, \tag{3.2.1}$$

where

$$G(\phi,\hat{\phi}) = \frac{v_s(\hat{\phi})}{e^{\pi(\phi+\hat{\phi})}-1} + \frac{v_s(\hat{\phi})}{1-e^{\pi(\phi-\hat{\phi})}} + \frac{v_s(\hat{\phi})}{e^{\pi(\hat{\phi}-\phi)}-1} + \frac{v_s(\hat{\phi})}{1-e^{-\pi(\phi+\hat{\phi})}}. \tag{3.2.2}$$

In order to use the trapezoidal rule (B.5), the semi-infinite domain in this equation is split into a finite segment for which the trapezoidal rule is applied, and a semi-infinite segment which can be either ignored or approximated [30]. The equation for the horizontal velocity is then

$$u_s(\phi) = 1 + \frac{1}{2}\int_0^{\phi_\mathrm{m}} G(\phi,\hat{\phi})\,\mathrm{d}\hat{\phi} + \frac{1}{2}\int_{\phi_\mathrm{m}}^\infty G(\phi,\hat{\phi})\,\mathrm{d}\hat{\phi} \quad \text{for } -\phi_\mathrm{m} < \phi < \phi_\mathrm{m}, \tag{3.2.3}$$

where $\phi_\mathrm{m} \gg 1$ is the domain truncation parameter.

Stokes' result on the asymptotic, or linearised, behaviour of the complex velocity as $|\phi| \to \pm\infty$ is used to approximate the integrand in the second integral in (3.2.3). The far-field complex velocity given by (D.11) can be written, again using the symmetry of the flow, as

$$u_s(\phi) - iv_s(\phi) \approx 1 + De^{-\lambda_0|\phi|}\left(\cos\lambda_0 \pm i\sin\lambda_0\right), \quad \text{as } |\phi| \to \infty, \tag{3.2.4}$$

for some real D. Here, $\lambda = \lambda_0$ is the smallest positive solution to

$$\tan\lambda = \lambda F^2, \tag{3.2.5}$$

with the positive sign in (3.2.4) taken for the downstream direction and the negative sign taken for the upstream direction.

The semi-infinite integral in (3.2.3) can be evaluated efficiently using hypergeometric functions (denoted ${}_2F_1$, see Abramowitz & Stegun [1]); for example the first term can be transformed by $\hat{\alpha} = e^{\pi\hat{\phi}}$,

$$\begin{aligned}\int_{\phi_\mathrm{m}}^{\infty} \frac{v_s(\hat{\phi})}{e^{\pi(\phi+\hat{\phi})}-1}\,\mathrm{d}\hat{\phi} &= \frac{D\sin\lambda_0}{\pi}\int_{e^{\pi\phi_\mathrm{m}}}^{\infty}\frac{\hat{\alpha}^{-(\lambda_0/\pi+1)}}{1-e^{\pi\phi}\hat{\alpha}}\,\mathrm{d}\hat{\alpha},\\ &= -D\sin\lambda_0\frac{e^{-\pi(\phi_\mathrm{m}+\phi)}e^{-\phi_\mathrm{m}\lambda_0}}{\pi+\lambda_0}{}_2F_1\left(1,1+\lambda_0/\pi;2+\lambda_0/\pi;e^{-\pi(\phi_\mathrm{m}+\phi)}\right),\end{aligned}$$

by formula 3.194.2 of [25]. The other terms in the semi-infinite integral have similar expressions in terms of ${}_2F_1$ (of which only one other is needed). Combining these results with the removal of the singularity (B.1) in the finite domain integral,

equation (3.2.3) can be written as

$$
\begin{aligned}
u_s(\phi) \approx 1 &+ \frac{1}{2}\int_0^{\phi_\mathrm{m}} \coth(\pi(\phi+\hat{\phi})/2)(v_s(\hat{\phi})+v_s(\phi))\,\mathrm{d}\hat{\phi} \\
&+ \frac{1}{2}\int_0^{\phi_\mathrm{m}} \coth(\pi(\hat{\phi}-\phi)/2)(v_s(\hat{\phi})-v_s(\phi))\,\mathrm{d}\hat{\phi} + \frac{v_s(\phi)}{\pi}\ln\left|\frac{\sinh(\pi(\phi-\phi_\mathrm{m})/2)}{\sinh(\pi(\phi+\phi_\mathrm{m})/2)}\right| \\
&\quad - D\sin\lambda_0\left\{\frac{e^{-\pi(\phi_\mathrm{m}+\phi)}e^{-\lambda_0\phi_\mathrm{m}}}{\pi+\lambda_0}{}_2F_1\left(1,1+\lambda_0/\pi;2+\lambda_0/\pi;e^{-\pi(\phi_\mathrm{m}+\phi)}\right)\right. \\
&\qquad \left. + \frac{e^{-\lambda_0\phi_\mathrm{m}}}{\lambda_0}{}_2F_1\left(1,\lambda_0/\pi;1+\lambda_0/\pi;e^{-\pi(\phi_\mathrm{m}-\phi)}\right)\right\}
\end{aligned}
\tag{3.2.6}
$$

for $-\phi_\mathrm{m} < \phi < \phi_\mathrm{m}$.

The singular term involving the logarithm function in (3.2.6) is partly compensated for by the fact that $v_s(\phi)$ decays exponentially as shown in Appendix D. Provided the computational method does not involve evaluation of $u_s(\phi)$ from (3.2.6) with $\phi \approx \phi_\mathrm{m}$, there is no risk of significant subtractive cancellation error when using a floating-point number system.

3.2.1 Numerical procedure

The piecewise-cubic transform from §2.3.1 is now applied to form a regular grid in the new variable β, and an irregular grid in ϕ. For symmetric waves, the left-hand endpoint of the integral is given by $\phi_{[1]} = 0$, and the right-hand endpoint is located at $\phi_{[M+1]} = \phi_\mathrm{m}$. For symmetric calculations, the value of M, which we recall is the number of intervals of the piece-wise cubic described in §2.3.1, also happens to be the number of crests of the wave. As per the form of the type-I–V waves, we find that there are only two cases for the number of crests to consider in the results presented in this chapter. The first case is when there is one only one crest at $\phi = x = 0$ and so $M = 1$, and the piece-wise cubic has one interval representing the portion of the wave in the region $x > 0$. When there are two crests, and thus two pieces to the $x > 0$ component of the wave, we have $M = 2$. In this case, the

location $\phi_{[2]}$ of the downstream crest is unknown and must be determined as part of the solution ($\phi_{[3]} = \phi_{\mathrm{m}}$ is the downstream end of the truncated domain).

The regular grid in β from §2.3.1 is

$$\beta_i = i, \quad \text{for } i = 0, 1, 2, \ldots, N, \tag{3.2.7}$$

and the corresponding irregular grid in ϕ is given by the function $\varphi(\beta)$ from (2.3.25),

$$\phi_i = \varphi(\beta_i), \tag{3.2.8}$$

where we also define the mid-points

$$\phi_{i+1/2} = \varphi\left(i + 1/2\right) \quad \text{for } i = 0, 1, 2, \ldots, N-1. \tag{3.2.9}$$

As stated previously, the majority of the equations in the algebraic system of equations are given by equating the dynamic boundary condition (2.2.12) evaluated at the mid-points $\phi_{i+1/2}$ with the same equation evaluated at the final point $\phi_{N-1/2}$, thus

$$\left[u_s(\phi)^2 + v_s(\phi)^2 + \frac{2}{F^2}\left(y_s(\phi) + p(x_s(\phi))\right)\right]_{\phi=\phi_{N-1/2}}^{\phi=\phi_{i+1/2}} = 0 \tag{3.2.10}$$

for $i = 0, 1, \ldots, N-2$. The values of $u_s(\phi_{i+1/2})$ are determined by applying the trapezoidal rule (B.5) to the integrals in (3.2.6). The pressure term can be calculated once $x_s(\phi_{i+1/2})$ is known, which is found by applying the mid-point rule to the integral (2.2.11)

$$x_s(\phi_i) = \frac{1}{2}\sum_{j=0}^{i-1} \frac{u_s(\phi_{j+1/2})}{u_s(\phi_{j+1/2})^2 + v_s(\phi_{j+1/2})^2}\varphi'(j + 1/2) \tag{3.2.11}$$

for $i = 0, \ldots, N$, then (while still maintaining the order of approximation) using the average $x_s(\phi_{i+1/2}) \approx \frac{1}{2}(x_s(\phi_i) + x_s(\phi_{i+1}))$. As there is no known or fixed value of $y_s(\phi)$ to work from, unlike $x_s(0) = 0$, we instead calculate the value $y_s(\phi_{i+1/2}) -$

$y_s(\phi_{N-1/2})$. Using the midpoint rule in (2.2.10), and the same averaging as for $x_s(\phi_{i+1/2})$, the following expression is derived:

$$\begin{aligned} y_s(\phi_{i+1/2}) - y_s(\phi_{N-1/2}) \approx \frac{1}{4}\frac{v_s(\phi_{i+1/2})}{u_s(\phi_{i+1/2})^2 + v_s(\phi_{i+1/2})^2}\varphi'(i+1/2) \\ - \frac{1}{2}\sum_{j=i}^{N-2}\frac{v_s(\phi_{j+1/2})}{u_s(\phi_{j+1/2})^2 + v_s(\phi_{j+1/2})^2}\varphi'(j+1/2) \\ - \frac{1}{4}\frac{v_s(\phi_{N-1/2})}{u_s(\phi_{N-1/2})^2 + v_s(\phi_{N-1/2})^2}\varphi'(N-1/2). \quad (3.2.12) \end{aligned}$$

The space of permissible solutions is explored by using the predictor-corrector method described in §2.4 to determine solution branches on which F is fixed. We choose value of B, which affects the width of the disturbance, to be 2.8 throughout this chapter so that the distance between the inflexion points of the pressure disturbance is approximately one. The qualitative nature of the results is fairly robust to changes in B, although there are certainly differences in the wide disturbance regime, when $B \ll 1$, that are not considered here. The uniform stream solution for a fixed Froude number $F > 1$ is taken as a starting point for our calculations. Given that solutions with one crest are found in the neighbourhood of the uniform stream, there are initially $N+3$ unknowns A, D, λ_0 and $v_s(\phi_i)$ for $i = 1, \ldots, N$ (as $v(\phi_0 = 0) = 0$, due to symmetry), and so $N+2$ equations are required altogether. Equation (3.2.10) provides the first $N-1$ equations. Another two equations are given by using the values $v_s(\phi_{N-1/2})$ and $v_s(\phi_{N-3/2})$, chosen to match the flow to the linearised solution by equating real and imaginary components of equation (3.2.4). The last equation we use is the relationship for λ_0 given by (3.2.5).

For each computed solution, two-crest solutions were detected by searching for any i such that $v_s(\phi_{i+1})v_s(\phi_i) < 0$ with $v_s(\phi_i) > 0$. When this occurred, the solution for which an additional crest was detected was interpolated onto a new grid with an extra unknown $\phi_{[2]}$ and an extra equation $v_s(\phi_{[2]}) = 0$, and the continuation algorithm was then resumed on this new system. Numerical

solutions were checked to be independent of the choice of N and ϕ_m (the results presented here are converged to within graphical accuracy). Typically $N > 1000$ and $\phi_m \approx 10$ in the computations. The choice of ϕ_m and the convergence of solutions is presented in further detail in §3.2.2.

There are other ways to explore the solutions space rather than simply fixing the Froude number. The branch of unforced waves can be computed using the same continuation method as for the fixed-F solution branches, except now $A = 0$ is fixed and F is an unknown system parameter to be determined. Other branches for fixed non-zero amplitude of forcing can be computed using the same approach. Another useful branch of solutions is the branch for which the velocity at the crest of the wave is fixed and small. As the velocity is small, these solutions are very close to solutions with a Stokes' corner flow at the crest, these are the waves which we refer to as the 'almost-highest' waves. We will compute the almost-highest waves using the unforced almost-highest solitary wave as a starting point. The system of equations and unknowns is again similar to those just described, except for the inclusion of a new equation $u_{\min} - \min_i u_s(\phi_i) = 0$, with $u_{\min}$ a fixed (known) constant, and A and F are now considered unknowns in the system.

3.2.2 Irregular grid equations and convergence

So far the unknowns and equations required for the transform $\varphi(\beta)$ from §2.3.1, as well as the choice of the parameter $\delta \ll 1$ which affects clustering near crests, have been omitted from the system. The unknowns in the formula for $\varphi(\beta)$ are the values of $\lambda_{[j]}$, and each adds a corresponding equation given by (2.3.26) to the system, so as required by our continuation method, there is still one more unknown than equations.

As shown in Appendix B, the error in the numerical evaluation of the integrals is well behaved with respect to the number of grid points, however the effect

of the width of the domain, ϕ_m, and the clustering parameter, δ, also needs to be considered. Hunter & Vanden-Broeck [30] showed that for unforced almost-highest waves, the linearised boundary condition allows for accurate solutions to be obtained for $\phi_m \approx 10$, however the clustering parameter is not considered in detail. Exact solutions are not available for most forced-wave problems and so to determine the effect of ϕ_m and δ, solutions using less refined grids are compared to solutions obtained by very refined grids to find an approximate value of the error.

First we consider the convergence of the free surface as function of ϕ_m. The grid spacing is held constant while the domain width is varied, to determine the approximate error as a function of domain width. This leads to a visual analysis of the region for which the solution is independent of ϕ_m.

The value $\Delta = \phi_m/N$ is used as a proxy for the grid spacing for our irregular grid. An estimate of the error for a given less-refined grid with $\Delta = \Delta_0$ and a particular value of the domain width $\phi_m = \phi_0$ is the average error in the ℓ_∞ norm over many values of ϕ_m for which a chosen high-resolution grid was computed. If the highest-resolution grid was computed with $\phi_m \in (\phi_{\min}, \phi_{\max})$ and $\Delta = \Delta_{\text{high}}$, then the error in the lower-resolution solution with $\Delta = \Delta_0$ and $\phi_m = \phi_0$ is

$$E(\Delta_0, \phi_0) = \frac{1}{\phi_{\max} - \phi_{\min}} \int_{\phi_{\min}}^{\phi_{\max}} \int_{-X}^{X} \left| \eta_{\text{num}}(\Delta_0, \phi_0) - \eta_{\text{num}}(\Delta_{\text{high}}, \hat{\phi}) \right| \, \mathrm{d}x \, \mathrm{d}\hat{\phi}, \tag{3.2.13}$$

where $X = x_s(\phi_m)$ is the physical extent of the domain, $\eta_{\text{num}}(\Delta, \phi_m)$ is a piece-wise continuous polynomial, calculated using MATLAB's `spline()`, fitted to the numerical solution with grid spacing parameter equal to Δ and domain width ϕ_m.

Newton's method was used to find almost-highest solutions for different grids with $\Delta = 0.0275, 0.0241, 0.0201, 0.0149$ and $\Delta_{\text{high}} = 0.00688$. The approximate error was evaluated for two free-surface problems, one being an almost-highest unforced solitary wave, the other being an almost-highest forced type-III wave. On

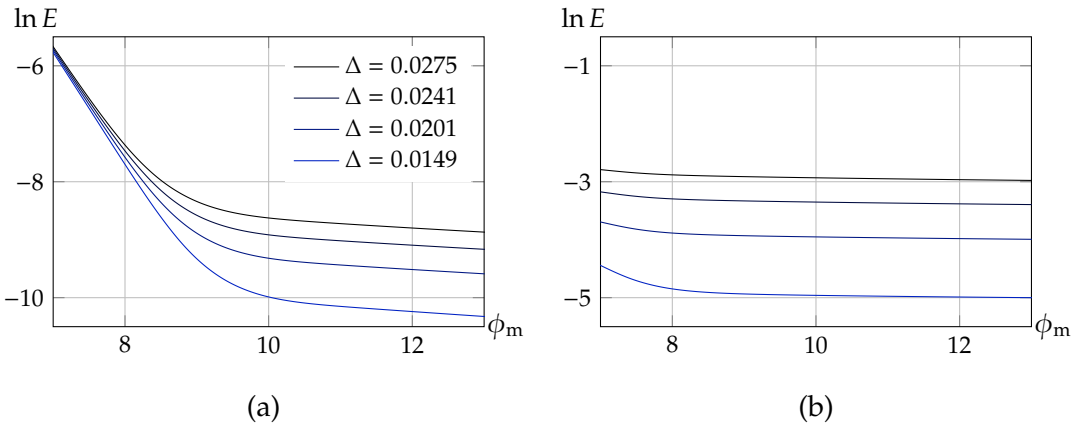

(a) (b)

Figure 3.2.2: Estimate of the average error E for $u_s(0) = 0.05$, $\Delta_{\text{high}} = 0.00688$, $\phi_{\text{min}} = 7$ and $\phi_{\text{max}} = 13$ with $B = 2.8$. Panels (a) and (b) show results for the unforced almost-highest wave with $F = 1.29089$ and the forced type-III wave with $F = 1.32$ respectively.

any branch of solutions there are two parameters to fix, so we fixed $u_s = 0.05$ at the crest and took $F = 1.29089$ for the unforced wave and $F = 1.32$ for the forced wave. The system of equations for Newton's method includes an additional equation to fix the value of u_s at the crest of the wave, compared to the under-determined system which we use to explore the solution space in this chapter. The forcing parameter A is thus found as part of the solution.

The value of the inner integral in (3.2.13) was computed by fitting splines to the free surface (using MATLAB's `fit()` function) for twenty evenly spaced values of ϕ_m in the range $(7, 13)$, then applying MATLAB's `quad()` routine. The outer integral was then computed by the same spline-fitting and numerical integration routine.

The logarithm of the approximate error as a function of ϕ_m is shown in figure 3.2.2 for the two types of wave. The almost-highest unforced wave is shown in panel (a), and the almost-highest type-III wave is shown in panel (b). The error is very stable for $\phi_m > 10$, with the majority of the change in the error being

attributed to changes in grid-spacing in this region. This was observed in all the calculations presented in this chapter and in the following chapter where topographical disturbances are investigated.

We observed during computations throughout that the continuation method would fail to converge to a solution for values of ϕ_{m} significantly greater than those considered here. We conjecture that this is a result of the exponential decaying free-surface quantities being of similar magnitude to the numerical integration error. This would cause the failure of the requirement that the solution be a regular point of the system. Nevertheless, accurate free-surface profiles were clearly obtained with values of $\phi_{\mathrm{m}} \approx 10$, with the the number of grid points being the predominant driver of error.

The effect of the clustering parameter δ is investigated in a very similar manner. For a given less-refined grid with $N = N_0$ and a particular value $\delta = \delta_0$ the average error is determined over the values of δ for which a chosen high-resolution grid was computed. If the high-resolution grid was computed for $\delta \in (\delta_a, \delta_b)$ and $N = N_{\mathrm{high}}$ grid points, then the error for a grid with $N = N_0$ points and $\delta = \delta_0$ is

$$E(N_0, \delta_0) = \frac{1}{\delta_b - \delta_a} \int_{\delta_a}^{\delta_b} \int_{-X}^{X} \left| \eta_{\mathrm{num}}(N_0, \delta_0) - \eta_{\mathrm{num}}(N_{\mathrm{high}}, \hat{\delta}) \right| \, \mathrm{d}x \, \mathrm{d}\hat{\delta} \qquad (3.2.14)$$

where again $X = x_s(\phi_{\mathrm{m}})$ is the physical extent of the domain, $\eta_{\mathrm{num}}(N, \delta)$ is a piecewise continuous polynomial calculated using MATLAB's `spline()` fitted to the numerical solution given by a grid with N points and δ as the clustering parameter.

The continuation method was well suited to finding the required solutions. The solutions were obtained by fixing u_s at the crest of an almost-highest unforced solitary, with $F = 1.29089$. The value of A comes as part of the solution, and δ acts as the parameter for the one-parameter family of solutions. The value of the inner integral was computed, again, by fitting splines to the free-surface solutions found for a discrete set of values in $\delta \in (0.005, 0.2)$ (the discrete values are not

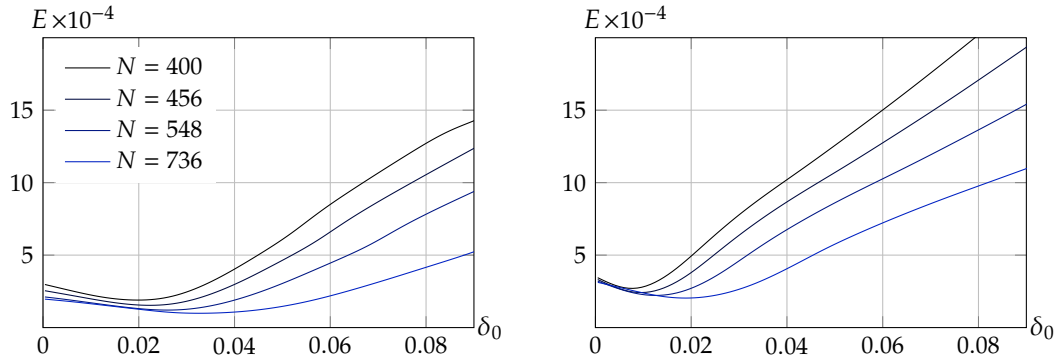

Figure 3.2.3: Estimate of the average error E for $F = 1.2909$, $N_{\text{high}} = 1600$, $\delta_a = 0.005$ and $\delta_b = 0.1$ with $B = 2.8$. Panels (a) and (b) show results for velocity $u_s(0) = 0.08$ and $u_s(0) = 0.05$ at the crest respectively.

necessarily the same for each continuation performed) for $N = 400, 456, 548, 736$, and $N_{\text{high}} = 1600$ and applying MATLAB's `quad()` routine. The outer integral was then computed by the same spline fitting and numerical integration routine.

The results in figure 3.2.3 show that values of δ near to 0.01 yield a minimum in the computed error for profiles with small velocities at the crest. The results also suggest that too small a value of δ may adversely impact the convergence of solutions for $u_s(0)$ near zero. The value of δ is taken to be 0.01 for the rest of the calculations in this chapter, and for the calculations performed in the following chapter for topographical disturbances.

3.3 Results

3.3.1 Weakly nonlinear model discussion

The solutions to the forced KdV equation are explored first so that the fully nonlinear results can be classified with reference to these solutions. According to

the weakly nonlinear model the solution's orbit within the phase plane given by (2.5.35) must begin and end with the saddle point at the origin for the supercritical flows studied here; this is the mathematical manifestation of the physical requirement that the free surface must approach a uniform stream with unit depth in both far upstream and downstream directions.

When the amplitude of forcing A is positive there are two types of solutions, as found by Grimshaw & Smyth [27] and Miles [47], here denoted as type I and II; these are illustrated in the phase-plane diagram of figure 3.3.4(b). The orbit in the phase plane for these two types of solution starts with the saddle point, moving in a clockwise direction along the homoclinic orbit in the upper half of the phase plane. The jump condition (2.5.34) when $A > 0$ gives a jump downwards in the phase plane. For the same value of $A > 0$ there are two positions at which the phase-plane trajectory can jump vertically downwards onto the homoclinic orbit in the lower half of the phase plane. The orbit through the phase plane for both type I and II solutions then continues along the homoclinic orbit (in the lower-half plane), returning to the saddle point. The weakly nonlinear type I solution has a vertical jump to the left of the centre, and as $A \to 0$ the solution approaches a uniform stream. On the other hand, the weakly nonlinear type II solution has a vertical jump to the right of the centre, and as $A \to 0$ the solution approaches the unforced solitary wave solution. Hence, the solution types I and II can be classified as perturbations of a uniform stream and (single) solitary wave, respectively.

The weakly nonlinear analysis in the phase plane shown in figure 3.3.4(d) predicts three types of solution III, IV and V when $A < 0$. Solution types III and IV were found as solutions to narrow disturbances by Miles [47], amongst others, while type V was found as a solution to the fKdV equation for a narrow disturbance by Malomed [44]. Starting with the saddle point, the solution types III and IV both traverse the homoclinic orbit from the upper half to the lower half

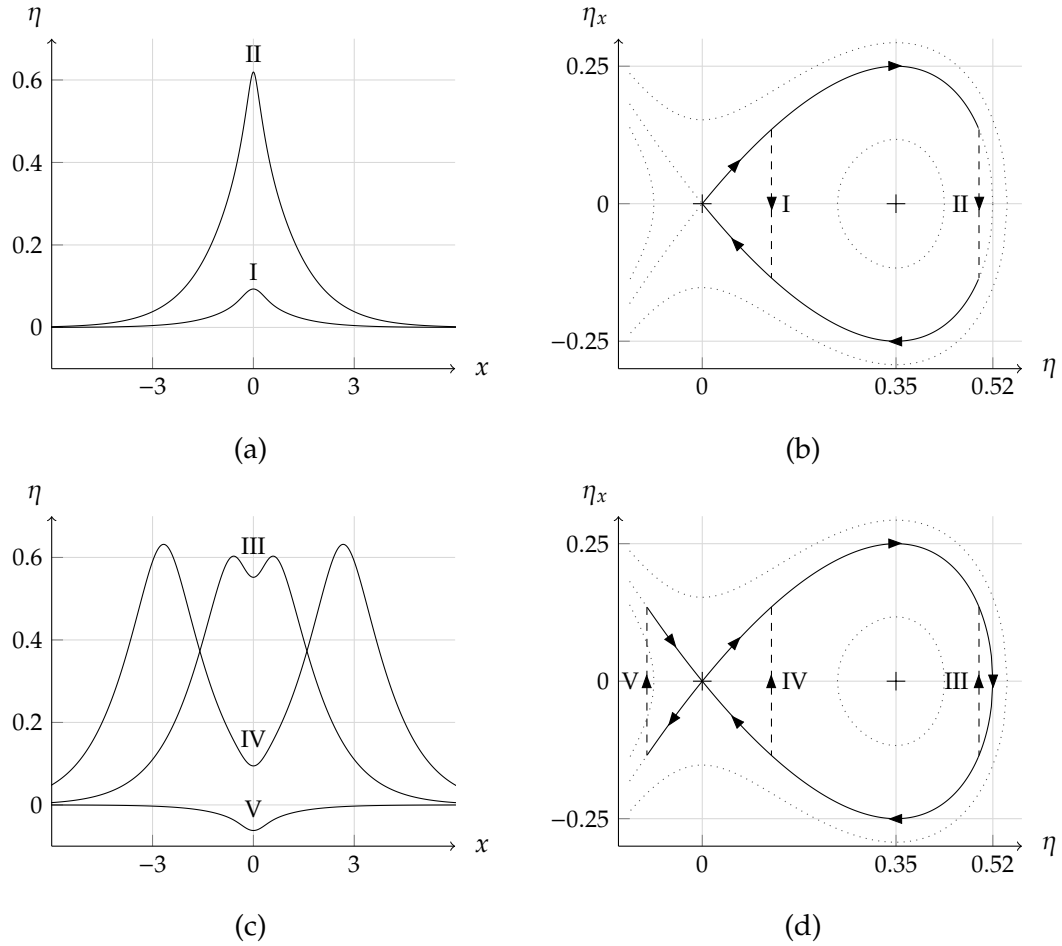

Figure 3.3.4: Forced solutions for the Froude number $F = 1.26$. Shown are (a) the nonlinear profiles for $A = 0.09$; here the profile labelled type II is a forced solitary wave with $\eta(0) = 0.62$ and the profile labelled type I is a perturbation of a uniform stream with $\eta(0) = 0.093$; (b) the weakly nonlinear phase portrait corresponding to (a) with $\eta(0) = 0.12$ and $\eta(0) = 0.50$, for the flow types I and II respectively; (c) the nonlinear profiles for $A = -0.09$. The profiles labelled types III and IV are forced solitary waves with $\eta(0) = 0.55$ and $\eta(0) = 0.091$ respectively. The flow type V is a perturbation of a uniform stream with $\eta(0) = -0.063$; and (d) the weakly nonlinear phase portraits corresponding to (c) with $\eta(0) = 0.50$, $\eta(0) = 0.12$ and $\eta(0) = -0.099$, for the flow types III, IV and V respectively.

of the phase plane, before jumping vertically upwards back onto the homoclinic orbit in the upper half of the phase plane. The orbit in the phase plane for these two solution types then continues around the homoclinic orbit terminating at the saddle point. The type III solution exhibits a vertical jump to the right of the centre, and as $A \to 0$ the solution approaches the unforced solitary wave solution. The type IV solution has a vertical jump to the left of the centre, and as $A \to 0$ the solution approaches two unforced solitary waves that are infinitely far apart. The type III and IV solutions can therefore be classified as perturbations of a single solitary wave and two solitary waves, respectively. The last type V solution, which exhibits a jump between two unbounded phase-plane trajectories that intersect with the saddle point, can be classified as a perturbation of a uniform stream.

For $F = 1.26$ and the values of A given in the caption, the fully nonlinear solutions plotted in figure 3.3.4(a) and (c) can be compared with the weakly nonlinear phase-plane diagrams of figure 3.3.4(b) and (d) respectively. The qualitative agreement between the weakly and fully nonlinear calculations is excellent. Due to the similarity in the solution space the fully nonlinear profiles, even the very steep profiles, are classified according to their weakly nonlinear counterparts; we will elaborate on some of the finer details regarding the classification of very steep waves next.

3.3.2 Fully nonlinear solution space

In figures 3.3.5(a)–(d) each panel shows two sets of solutions for a fixed value of F plotted as curves in the $(A, \eta(0))$-plane, obtained from the nonlinear (solid curve) and weakly nonlinear (dotted curve) calculations. In addition a set of almost-highest solutions is plotted (two dashed curves) which have a fixed, but small, velocity at the crest rather than a fixed value of F. For $1 < F < 1.26$ the qualitative nature of the solution space in the $(A, \eta(0))$-plane was found to be

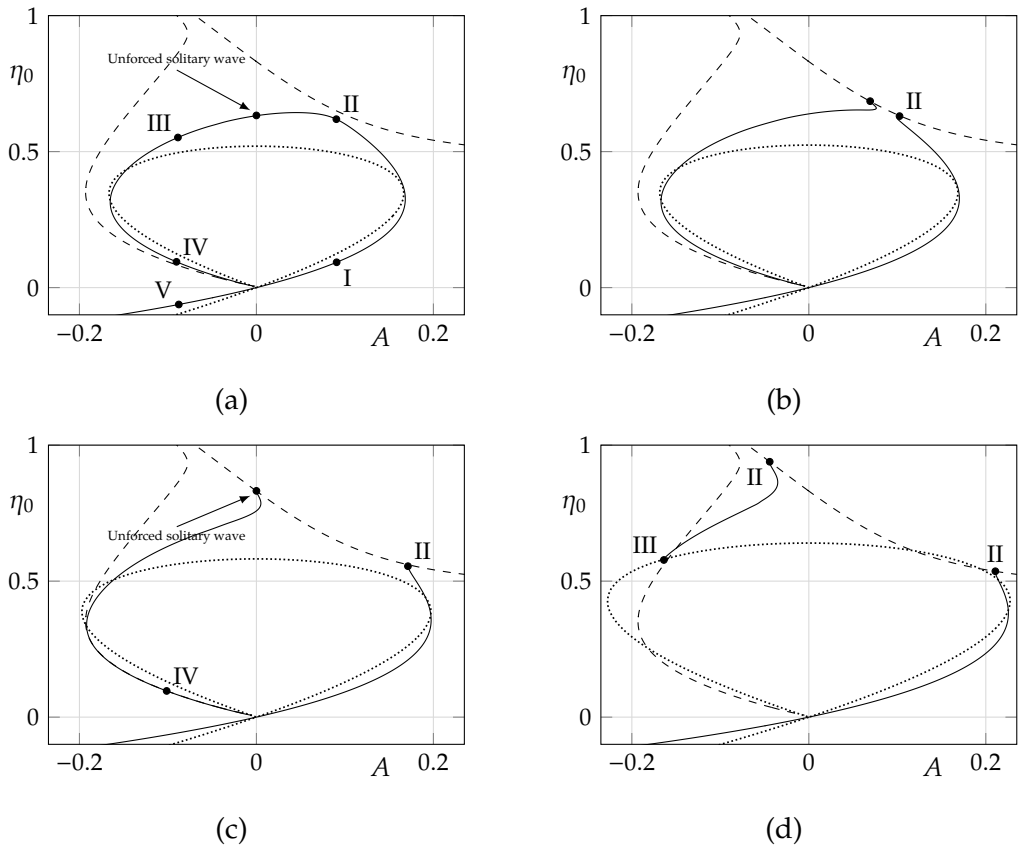

Figure 3.3.5: Plots of the variation of $\eta(0)$ versus forcing amplitude for the four values of Froude number $F = \{1.26, 1.262, 1.2909, 1.32\}$. The solid curves are derived from the fully nonlinear calculations. The dotted curves indicate values derived from the weakly nonlinear analysis. The dashed curves in (a)–(d) are the locus of the 'near-limiting' values, with $u = 0.05$ at the wave crests. The markers in (a) indicate the location in parameter space of the unforced solution and the five types of forced solution shown in figure 3.3.4, whereas in (b) they identify the forced almost-highest solitary waves, in (c) the upper and two lower markers denote the unforced and forced (type indicated next to marker) almost-highest solitary waves respectively, and finally in (d) all markers denote forced almost-highest solitary waves, with types indicated.

the same for the fully nonlinear and weakly nonlinear system, with the 'loop' contracting towards the origin as $F \to 1$, with a tail in the lower-half plane as $A \to -\infty$. The number of parameters required to determine a fully nonlinear solution is exactly as per the weakly nonlinear solution. The weakly nonlinear results, whilst still providing good qualitative agreement with the fully nonlinear calculations, begin to diverge from the fully nonlinear results as F increases away from 1. For $F > 1.26$ the solid curve obtained from the numerical continuation of the nonlinear problem becomes disconnected (see figures 3.3.5(b)–(d)), which is not predicted by the weakly nonlinear analysis.

We note that all of the almost-highest waves are perturbations of either one or two solitary waves, not uniform streams, and are classified according to their corresponding weakly nonlinear counterparts as being of either type II, III or IV. The upper dashed curve in figure 3.3.5 are the almost-highest type II waves which have a single crest, while the dashed curve which emanates from the origin into the left-hand side of the upper half of the (A, η_0)-plane begins with solutions of type IV with two crests, as it is traversed upwards, it reaches a turning point after which the solutions are all considered of type III, with a cusp-like appearance at the crest. The key difference between the type-II and type-III solutions is the presence of the cusp, the presence of which is maintained on the almost-highest branch as the height increases up to the limit of the computational scheme used here, near $\eta(0) \approx 1.3$.

The almost-highest forced type-II waves do not all have $F = F_{\mathrm{u}}$, the Froude number corresponding to the highest unforced solitary wave. The markers in figure 3.3.5(b) indicate two almost-highest waves with $F = 1.262$, where the branch of solutions for fixed F is now disconnected. As the value of the Froude number increases, to $F = 1.2909 \approx F_{\mathrm{u}}$ in figure 3.3.5(c), and $F = 1.32$ in figure 3.3.5(d), the distance between the two markers on the upper almost-highest solution branch

in the $(A, \eta(0))$-plane increases. The left-most marker in figure 3.3.5(b), when $F = 1.262$, corresponds to a type-II solution shown in figure 3.3.7(a), and the corresponding marker for $F = F_{\mathrm{u}}$ in figure 3.3.5(c) indicates the unforced wave shown in figure 3.3.6(a). Finally, as this marker moves towards the position shown in figure 3.3.5(d) for $F = 1.32$, it corresponds to a type-II solution shown in figure 3.3.9(a). This last solution is new, and is classified as a perturbation of a single solitary wave, but differs from the corresponding weakly nonlinear solution as it lacks a cusp at the centre of the wave; this is a result of the non-singular and smooth pressure disturbance in the fully nonlinear calculations.

The almost-highest type-IV solutions all have $F \approx F_{\mathrm{u}}$, which can be explained by the fact that the position of the two wave crests for wave form IV are a considerable distance away from the centre of the free-surface pressure distribution (2.1.2). As the wave crests are not affected by the localised forcing of the pressure and are therefore effectively unforced, they retain the limiting value of F being very close to F_{u}. The lower marker on the branch of almost-highest type IV solutions in figure 3.3.5(c) corresponds to the profile (solid curve) in figure 3.3.8(a). Once the solutions along this branch are considered of type III, the value of F for the almost-highest wave varies. It can be seen that as the type-III marker moves up to its location in figure 3.3.5(d) the value of F has increased to 1.32 for the almost-highest wave (shown in figure 3.3.10(a)); as F increases further, so does the height of the centre of the wave.

The results presented in figure 3.3.6–3.3.10 show the detail in the solution space; clearly demonstrating the non-uniqueness for a fixed forcing when the waves are very steep. These solutions were computed using solutions found in figure 3.3.5(c)–(d) as starting points, with the amplitude of forcing fixed as previously described in §3.2. The layout of the panels (a)–(d) in figure 3.3.7–3.3.10 is described next, with reference to the well known results of the unforced case shown in figure

3.3.6.

Figure 3.3.6(a) shows the elevation of the free surface for two unforced nonlinear waves, broken and solid curves respectively, that are both close to the Stokes limiting configuration, for the same value of the Froude number $F = F_{\mathrm{u}}$. The broken and solid curves plotted in figure 3.3.6(b) show the angle θ the free surface makes with the horizontal for each of the two profiles shown in figure 3.3.6(a). Following Longuet-Higgins & Fox [40] and others, we define the parameter

$$\omega = 1 - (u_s(\phi_c)F)^2, \tag{3.3.15}$$

where ϕ_c is the location of the wave-crest. This parameter represents a rescaled wave-height, with a maximum value $\omega = 1$, corresponding to waves with a Stokes limiting configuration. Figure 3.3.6(c) shows a plot of the Froude number against the wave-height parameter ω, close to the Stokes limiting configuration.

A plot of the total energy $E = T + V$ versus ω is shown in figure 3.3.6(d). The total energy E is evaluated using the numerical solution for the free-surface on the irregular grid using the following quantities;

$$\begin{aligned}
\text{mass} = M &= \int_{-\infty}^{\infty} \eta \,\mathrm{d}x; \\
\text{kinetic energy} = T &= \int_{-\infty}^{\infty}\int_{0}^{1+\eta} \frac{1}{2}\left((u+1)^2 + v^2\right)\,\mathrm{d}y\,\mathrm{d}x; \\
\text{potential energy} = V &= \frac{1}{F^2}\int_{-\infty}^{\infty} \frac{1}{2}\eta^2\,\mathrm{d}x; \\
\text{circulation} = C &= \int_{-\infty}^{\infty} (u+1, v)\cdot \mathrm{d}\mathbf{x} = \left[\phi(x,1) - x\right]_{x=-\infty}^{x=\infty}.
\end{aligned}$$

The circulation C is estimated by using the values of ϕ and x on the free surface at the end-points of the truncated domain rather than at $x = \pm\infty$, while M and V are estimated using the trapezoidal rule on the free surface. The kinetic energy T is calculated using the result from Longuet-Higgins & Fenton [39],

$$2T = M - C. \tag{3.3.16}$$

One of the striking features of the unforced solutions is the oscillatory nature of the values of F and E as the solution approaches the limiting configuration, i.e. as $\omega \to 1$; see figure 3.3.6(c) and (d). For a grid size with $N = 1000$, these results show the first two turning points of the oscillation; it has been conjectured by Longuet-Higgins & Fox [40] that there are infinitely many oscillations (decreasing in amplitude) as $\omega \to 1$ in the unforced case. The solid lines in figure 3.3.6(c) and (d) are nearly coincident with the cross markers which show the numerical results of Longuet-Higgins & Tanaka [41]. The agreement in the values for the Froude number F is excellent, while the energy E obtained from these results is slightly less accurate due to the use of the trapezoidal rule to estimate the mass M and potential energy V; nevertheless the presence of at least two local extrema as $\omega \to 1$ is clear. By using a more refined grid with twice as many grid points, the third turning point of F and E could be obtained by this method.

We now have evidence of the oscillatory behaviour which has been observed in the unforced case also being present in the forced solutions as they approach the limiting configuration; see figures 3.3.7–3.3.10(c) and (d). Two local extrema were observed for both F and E for all the branches observed as $\omega \to 1$. It is possible that further local extrema, or even infinitely many, could be found as $\omega \to 1$, much like the unforced case [40], although this cannot be properly established by these numerical results. We do not pursue this matter here.

Another feature that is common between the forced and unforced solutions is that all solution-types which are perturbations to solitary waves, approach the Stokes limiting configuration of an included angle of 120° and a stagnation point at their crests, although there is an additional effect on the crest due to the nearby pressure disturbance found for the type III solutions. The angle of the computed free surfaces (figures 3.3.6(b)–3.3.10(b)) illustrate the near-Stokes limiting configuration by way of a rapid change from $\pi/6$ to $-\pi/6$ near the crest,

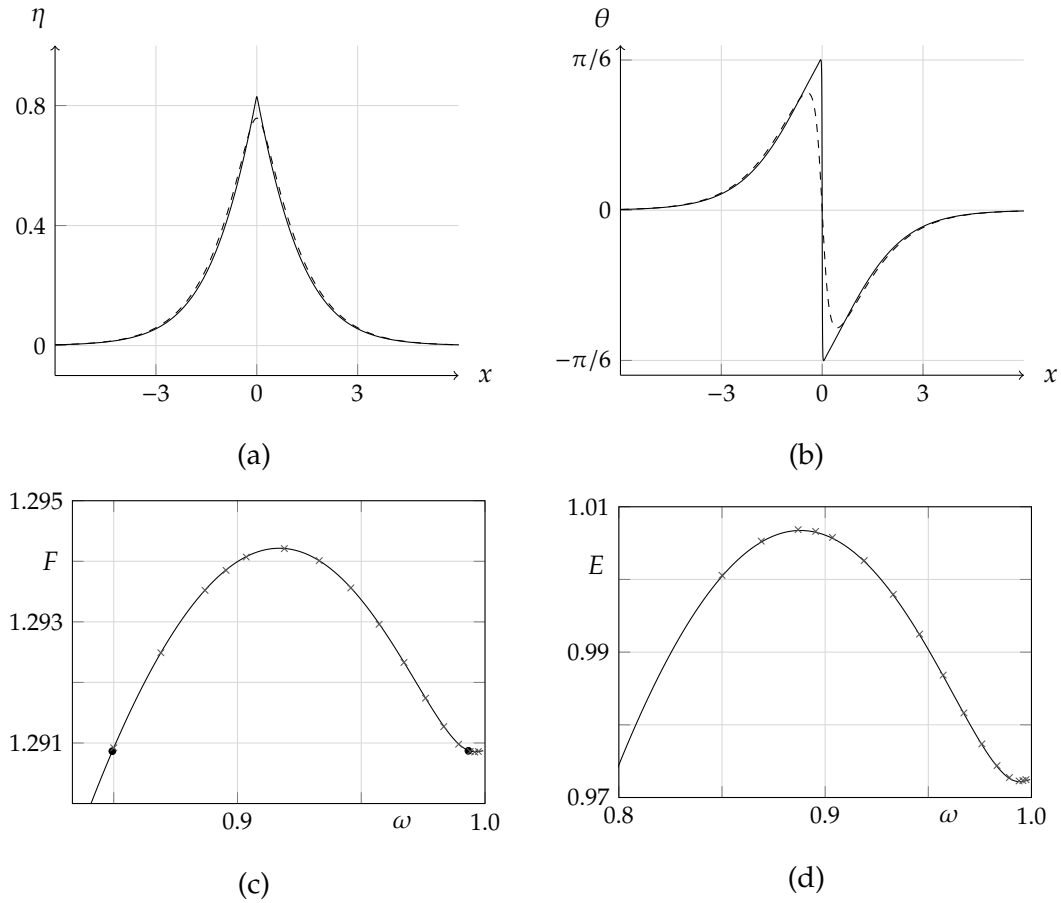

Figure 3.3.6: Results for unforced solitary waves. Shown are (a) the free-surface profiles for a value of the Froude number $F = 1.2909$, solid and dashed curves are for values of $\omega = 0.995$ and $\omega = 0.849$, respectively; (b) a plot of θ versus x for (a) ; (c) and (d) plots of the Froude number F and wave energy E versus ω defined in 3.3.15, respectively. Circular markers in (c) indicate the location of the profiles shown in (a), while crosses indicate the numerical results obtained by Longuet-Higgins & Tanaka [41] for almost-highest waves.

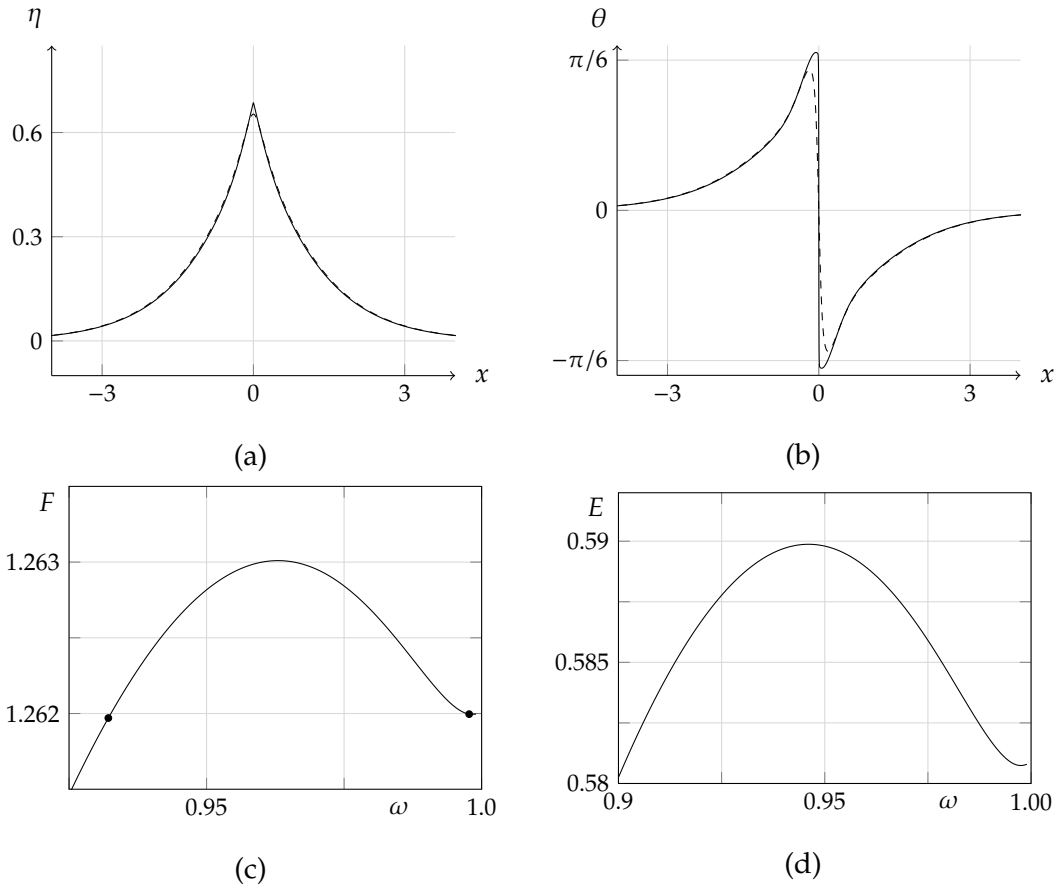

Figure 3.3.7: Forced solitary waves of type II, with amplitude of forcing $A = 0.07$. Shown are (a) nonlinear profile for a value of the Froude number $F = 1.262$, the solid and dashed curves are for values of $\omega = 0.998$ and $\omega = 0.932$, respectively; (b) plot of free-surface angle θ versus x for (a); (c) and (d) plots of the Froude number F and wave energy E versus ω, respectively. Markers in (c) indicate location of profiles shown in (a).

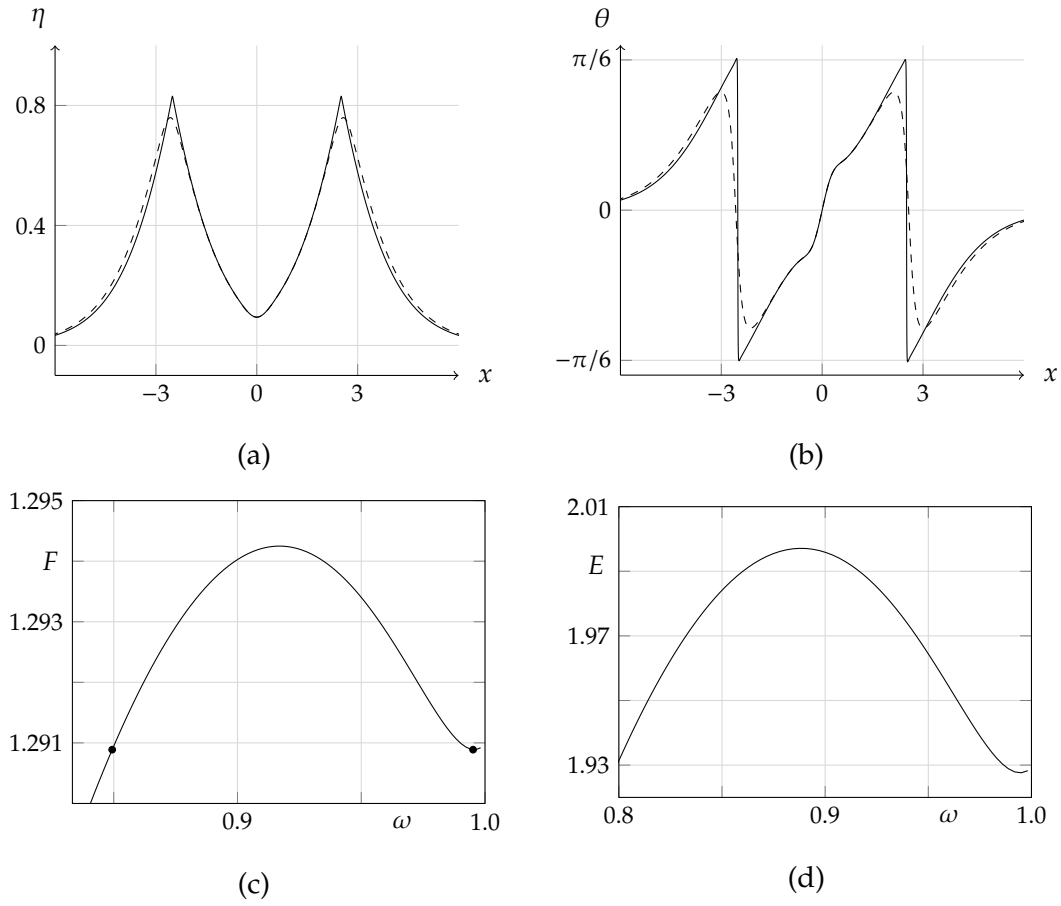

Figure 3.3.8: Forced solitary waves of type IV, with amplitude of forcing $A = -0.10$. Shown are (a) Free-surface profile for a value of the Froude number $F = 1.2909$, the solid and dashed curves are for values of $\omega = 0.995$ and $\omega = 0.850$, respectively; (b) plot of θ versus x for (a); (c) and (d) plots of the Froude number F and wave energy E versus ω, respectively. Markers in (c) indicate location of the profiles shown in (a).

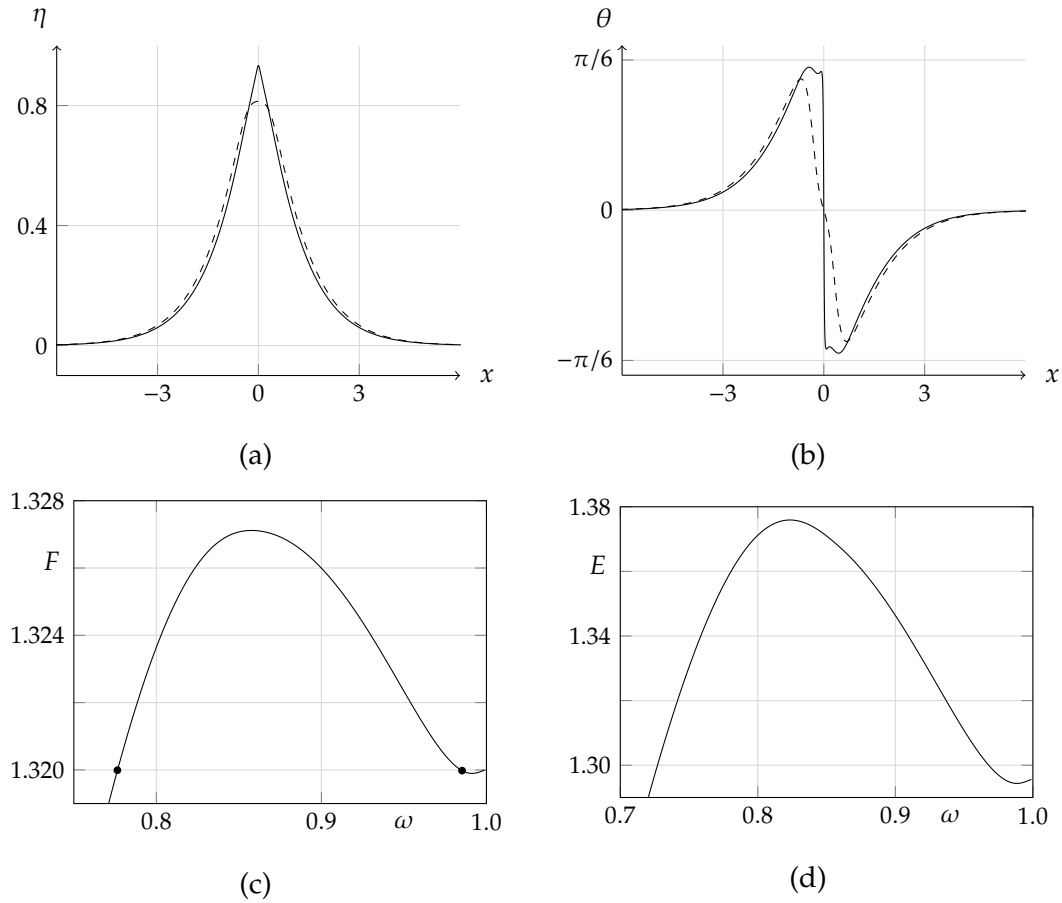

Figure 3.3.9: Forced solitary wave of type II with amplitude of forcing $A = -0.0441$. This type of solution is not predicted by the weakly nonlinear analysis. Shown are (a) Nonlinear profiles for a value of the Froude number $F = 1.320$, solid and dashed curves are for values of $\omega = 0.985$ and $\omega = 0.776$, respectively; (b) Plot of θ versus x for (a); (c) and (d) plots of the Froude number F and wave energy E versus ω, respectively, markers in (c) indicate the location of the profiles shown in (a).

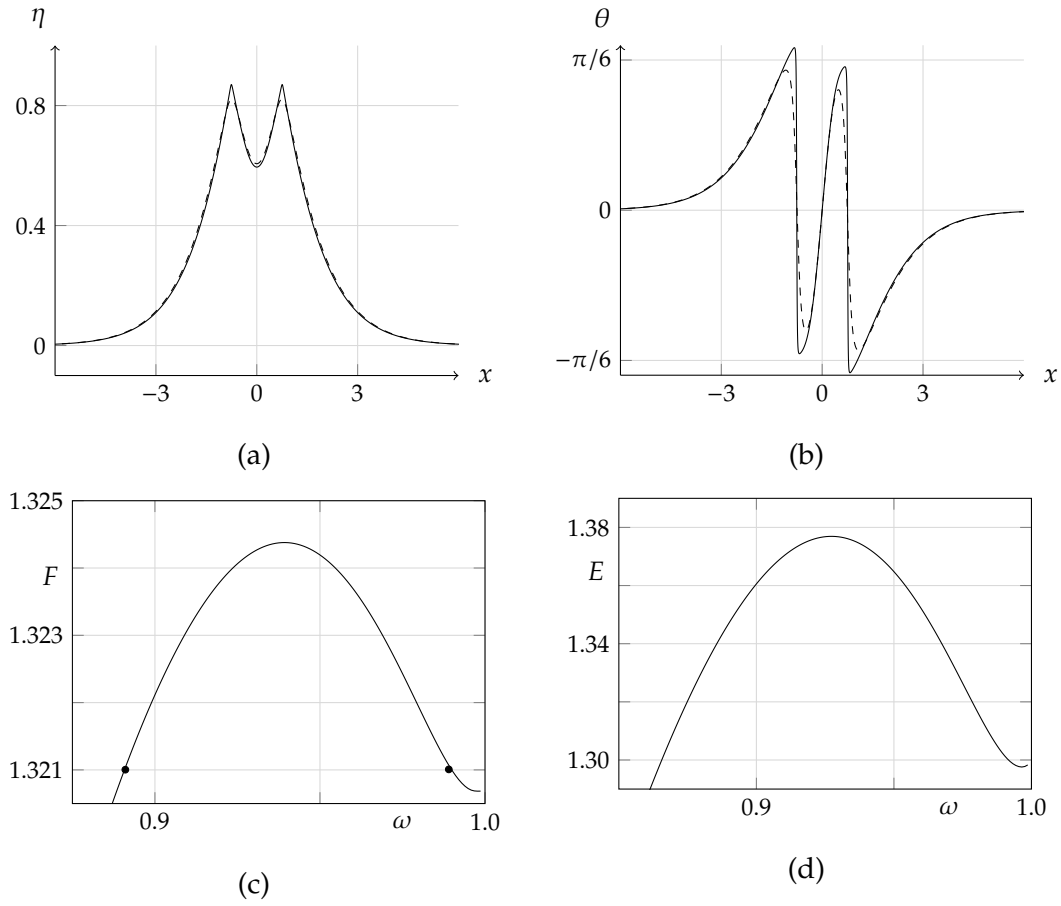

Figure 3.3.10: Forced solitary wave of type III with amplitude of forcing $A = -0.157$. This type of solution is not predicted by the weakly nonlinear analysis. Shown are (a) Nonlinear profiles for a value of the Froude number $F = 1.321$, solid and dashed curves are for values of $\omega = 0.989$ and $\omega = 0.891$, respectively; (b) Plot of θ versus x for (a); (c) and (d) plots of the Froude number F and wave energy E versus ω, respectively, markers in (c) indicate the location of the profiles shown in (a).

except in the case of figure 3.3.10(b). At the crests of the solution shown in figure 3.3.10(b), the plot shows a rapid change in θ of similar magnitude, but shifted vertically. This indicates that the corner flow has the same included angle but the left and right crests are perturbed by a small rotation; counter-clockwise for the left crest, and clockwise for the right. This is consistent with a modified Stokes' analysis, as we now demonstrate.

To proceed with the analysis, we adopt a reference frame given by the complex coordinate $\tilde{z} = \tilde{x} + \mathrm{i}\tilde{y}$ where $\tilde{x} = x - x_c$ and $\tilde{y} = y - (1 + \eta_c)$. x_c is the horizontal displacement of the crest relative to the pressure disturbance, and η_c is the displacement of the crest from a uniform stream. In this reference frame the crest is at the origin in the $\tilde{z}$ plane. Dropping the tilde notation from here on (but maintaining the new reference frame), the complex potential near the crest is assumed to be of the form $f(z) = \phi(z) + \mathrm{i}\psi(z) = Re^{\mathrm{i}\tau}z^n$ for real numbers R and τ with the index $n > 1$ to be determined.

In these coordinates, equation (2.1.2) is

$$p(x; A, B, x_c) = \frac{AB}{\sqrt{\pi}} e^{-(B[x+x_c])^2}.$$

Expanding the pressure disturbance in x about $x = 0$ using a Taylor series gives

$$p(x; A, B, x_c) = \hat{A}\left(1 - x\hat{B}\right) + \cdots$$

where $\hat{A} = AB\pi^{-1/2}e^{-(Bx_c)^2}$ and $\hat{B} = 2Bx_c$, and here $\cdots$ denotes higher-order terms.

Bernoulli's equation (2.1.7), under the assumption that for small x the streamline of the free surface is asymptotically $y = m_+x$ downstream, and $y = m_-x$ upstream, combined with the expansion of the pressure term, gives

$$R^2n^2((1 + {m_\pm}^2)x^2)^{n-1} + \frac{2}{F^2}\left(m_\pm x + \eta_c + \hat{A}\left(1 - x\hat{B} + \cdots\right)\right) = 1. \tag{3.3.17}$$

As $x \to 0$ the leading-order component of (3.3.17) yields $2(\eta_c + \hat{A})/F^2 = 1$. To determine the index n, we proceed to higher-order terms and balance the $O(x^{2n-2})$

terms with the $O(x)$ term in (3.3.17), this yields the value $n = 3/2$. Substituting this value in to (3.3.17) it follows that

$$R = \frac{2}{3F}\sqrt{\frac{\pm 2\left(\hat{A}\hat{B} - m_{\pm}\right)}{\sqrt{1 + {m_{\pm}}^2}}},$$

where the $\pm$ is taken on the downstream and upstream sides respectively, and $\hat{A}\hat{B} > m_+$ for $x > 0$, and $\hat{A}\hat{B} < m_-$ for $x < 0$. As R is a constant, the following equation needs to be satisfied

$$(\hat{A}\hat{B} - m_+)\sqrt{1 + {m_-}^2} + (\hat{A}\hat{B} - m_-)\sqrt{1 + {m_+}^2} = 0. \tag{3.3.18}$$

For the assumed form of the potential and the flow domain $\mathrm{Im}\,(f) \in (-1, 0)$ (a condition imposed by the non-dimensionalisation chosen here), it follows that if the downstream streamline of the free surface is given by $z_+(r) = re^{\mathrm{i}\theta_+}$, and the upstream streamline is given by $z_-(r) = re^{\mathrm{i}\theta_-}$ then

$$\theta_+ = -\frac{2}{3}\tau \quad \text{and} \quad \theta_- = -\frac{2}{3}(\tau + \pi).$$

As $f_z = \phi_x - \mathrm{i}\phi_y$ and ϕ_y/ϕ_x is the slope of the streamline, then since

$$\frac{\mathrm{d}f}{\mathrm{d}z} = \frac{3R}{2}e^{\mathrm{i}\tau}z^{1/2}$$

a relationship between τ and $m_\pm$ is found by substituting z_- and z_+ into the above expression and applying the previous two equations relating τ and $\theta_\pm$;

$$\tan\left(\frac{2}{3}\tau\right) = -m_+ \quad \text{and} \quad \tan\left(\frac{\pi}{3} - \frac{2}{3}\tau\right) = m_-. \tag{3.3.19}$$

Solving equations (3.3.18) and (3.3.19) serves to determine the slope $m_\pm$ of the downstream and upstream surfaces, which must have an included angle of 120°. These provide the same result as that of Stokes when $x_c = 0$ (and when $A = 0$), i.e. when the pressure disturbance is at the location of the crest (or when there is no pressure disturbance). In this case the flow has a crest with a 120° included angle and it is symmetric in the sense that $-m_+ = m_- = \tan(\pi/6)$.

When $x_c \neq 0$ and $A \neq 0$ then the solutions to (3.3.18) and (3.3.19) suggest a crest that will be re-orientated, but still having a 120° included angle. When x_c is positive, the crest is rotated slightly clockwise and when x_c is negative the crest will be rotated counter-clockwise, similar to figure 3.3.10(b). As $|x_c|$ gets large, the solutions will limit to $-m_+ \to m_-$ and $m_- \to \tan(\pi/6)$, so the symmetric result will be observed for crests that are far from the pressure disturbance, as in figure 3.3.8(b).

3.4 Conclusion

The solution space for the forced waves and the presence of almost-highest forced solitary waves has been established. The forced solutions that approach the Stokes limiting configuration consist of perturbations of either one or two solitary waves. For all values of the Froude number $F > 1.262$, almost-highest type II waves with amplitude of forcing $A > 0$ exist, as seen in figures 3.3.5(b)–(d) (right-most markers). The almost-highest unforced and forced type IV waves, where $A < 0$, exist for the value $F = F_{\mathrm{u}}$. When the Froude number $F > F_u$ there are almost-highest type II and III waves with $A < 0$, as shown in figure 3.3.5 (d) (left-most and upper markers).

The nearby forcing for the almost-highest type III solution has the effect of altering the orientation of the limiting configuration of the crests, visible in figure 3.3.10(b). For single crested waves the limiting configuration is symmetric about a vertical axis, and the crest has an included angle of 120°. For the type III wave the included angle is still 120° at each crest, however the downstream crest is rotated slightly clockwise and the upstream crest is rotated slightly counter-clockwise from a horizontal orientation. This result is consistent with the modified Stokes' analysis presented at the end of §3.3.

We have shown that, like unforced waves, the total energy of the forced waves passes through local maxima and minima as the wave-height is increased. This raises a question about the stability of the forced waves, given that for unforced waves the first local maxima is associated with a superharmonic, i.e. short wavelength, instability [32, 40, 60].

The stability of the forced solutions prior to reaching the almost-highest waves is investigated in Chapter 5. The weakly nonlinear theory provides a model of the behaviour in this regime [14, 28]. The linearisation of the fKdV about steady solutions is considered numerically [18], as well as the results of time-dependent simulations using spectral or finite-difference code for the fKdV equation with a Gaussian forcing term.

Chapter 4

Waves past a localised topographical disturbance

4.1 Introduction

The solution space of almost-highest waves subject to a topographical disturbance is presented in this chapter. The topography is assumed flat except for a localised disturbance like a bump or a dip in the channel, the latter case is shown schematically in figure 4.1.1. As for the case of the pressure disturbances, we only consider

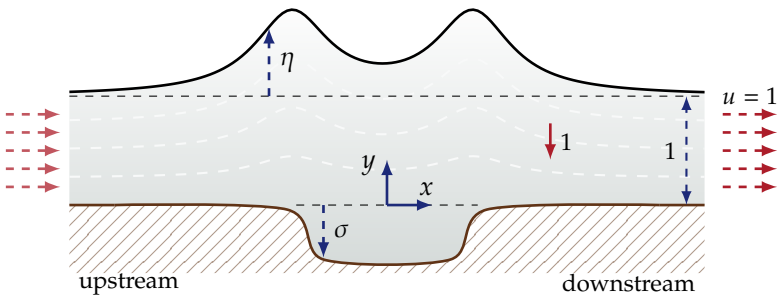

Figure 4.1.1: Schematic of the flow considered in this chapter, with zero pressure on surface, topography given by equation (2.1.3) and symmetry about $x = 0$.

supercritical flow ($F > 1$), and the topography is assumed to be symmetric about the vertical axis, where the shape of the topography is given by equation (2.1.3). For comparison with the results for a pressure disturbance, only symmetric steady solutions are considered, and so this symmetry is utilised in the formulation of the free-surface problem. The specific details of the numerical procedure for finding solutions to the fully nonlinear model are given in §4.2, using the numerical methods outlined in Chapter 2.

The time-dependent response of resonant flow past a topographical disturbance has received considerable attention due to the phenomenon of the generation of upstream advancing solitary waves [4, 13, 27, 36, 70, 71]. The consistent result of these investigations, using weakly nonlinear and fully nonlinear approaches, has been that the free surface near to the disturbance will tend towards a perturbation to a uniform stream, however the solution space of steady solutions is still not entirely established.

For the steady supercritical flow past a bump, the perturbations to uniform streams and solitary waves were computed by Forbes & Schwartz [23] and Vanden-Broeck [65] using a boundary-integral method. Dias & Vanden-Broeck [15] and Elcrat & Miller [21] also computed limiting configurations for a triangle shaped obstacle with a boundary-integral method, but did not explicitly comment on whether the non-uniqueness observed for the unforced flows as they approach limiting configurations was observed. Using the weakly nonlinear theory, a parametric map of these solutions was found by Ee & Clarke [18].

Perturbations to solitary waves were found via weakly nonlinear theory by Shen [53] as solutions to flow past a trench, and a parametric map of these solutions was determined by Ee *et al.* [20]. Some corresponding fully nonlinear profiles have been computed using boundary-integral methods [8, 10], however very steep waves near limiting configurations have yet to be computed.

In §4.3 we find that the space of solutions differs considerably from that found for a pressure disturbance, in particular when the amplitude of forcing is negative, i.e. for a flow past a trench. The solutions for flow past a trench extend into a region with very deep trenches where, for a fixed value of F, an increase in the amplitude of the topographical disturbance no longer has a significant impact on the shape of the free surface. It is found that only the flow near the topography is affected by the increase in the amplitude of the forcing. The true physical flow past a very deep trench would likely differ from these results. In the real setting it would be expected that the boundary layer would separate from the topography, and viscous effects which dominate this region are not modelled in potential flow considered here.

As the wave-height increases the solutions identified as a perturbation to a solitary wave with a single crest, or a perturbation to two solitary waves, approach the Stokes limiting configuration of a wave with a 120° included angle and stagnation point at the crest, or crests in the latter case. In the case of a perturbation to a solitary wave with a cusp, the solutions approach a wave with a single crest as the wave-height increases. We find that as the topographically forced solutions approach a Stokes limiting configuration, many properties of the wave are non-unique with respect to the height of the wave, as per the results for unforced waves [40, 43]. In §4.4 some concluding remarks are made about the results and potential future work.

4.2 Formulation

In contrast to the calculations for flow past a pressure disturbance in the previous chapter, which utilised equation (2.2.22), we use equation (2.2.24) to form the system of equations for the free surface. This equation gives $\tau_s(\phi)$ explicitly using

$\theta_s(\phi)$, rather than $u_s(\phi)$ via the integral transform of $v_s(\phi)$.

The symmetry exploited in the formulation of equation (3.2.6) for the waves past a pressure disturbance is also used here, and so again only one half of the wave is needs to be computed. By exploiting the symmetry for the free surface, namely

$$\theta_s(-\phi) = -\theta_s(\phi) \quad \text{and} \quad \tau_s(\phi) = \tau_s(-\phi),$$

the principal-value integral in (2.2.24) is transformed by an appropriate change of variables to a familiar form;

$$\tau_s(\phi) = \underbrace{\frac{1}{2} \fint_0^\infty G(\phi, \hat{\phi})\, \mathrm{d}\hat{\phi}}_{=I_1(\phi)} - \underbrace{\int_{-\infty}^{\infty} \frac{\theta_b(\hat{\phi})}{e^{\pi\hat{\phi}} + e^{\pi\phi}} e^{\pi\hat{\phi}}\, \mathrm{d}\hat{\phi}}_{=I_2(\phi)} \quad \text{for } -\infty < \phi < \infty, \quad (4.2.1)$$

where

$$G(\phi, \hat{\phi}) = \frac{\theta_s(\hat{\phi})}{e^{\pi(\phi+\hat{\phi})} - 1} + \frac{\theta_s(\hat{\phi})}{1 - e^{\pi(\phi-\hat{\phi})}} + \frac{\theta_s(\hat{\phi})}{e^{\pi(\hat{\phi}-\phi)} - 1} + \frac{\theta_s(\hat{\phi})}{1 - e^{-\pi(\phi+\hat{\phi})}}. \quad (4.2.2)$$

The principal-value integral in equation (4.2.1) is denoted $I_1(\phi)$. This is treated in a similar manner to the corresponding integral in equation (3.2.1) from the pressure-disturbance calculations presented in the previous chapter, except for a difference in the evaluation of the contributions from the far field which will be discussed next. Following this the non-principal-value integral in equation (4.2.1), denoted $I_2(\phi)$, is examined. In the pressure-disturbance calculations the analogous non-principal value integral was exactly zero, however here it will be evaluated numerically as the angle of the topography $\theta_b(\phi)$ is generally non-zero.

The semi-infinite domain for the term $I_1(\phi)$ in equation (4.2.1) is split into a finite and a semi-infinite segment to prepare for the use of the trapezoidal rule (B.5), so

$$I_1(\phi) = \frac{1}{2} \fint_0^{\phi_\mathrm{m}} G(\phi, \hat{\phi})\, \mathrm{d}\hat{\phi} + \frac{1}{2} \int_{\phi_\mathrm{m}}^{\infty} G(\phi, \hat{\phi})\, \mathrm{d}\hat{\phi} \quad \text{for } -\phi_\mathrm{m} < \phi < \phi_\mathrm{m} \quad (4.2.3)$$

where $\phi_{\mathrm{m}} \gg 1$ is the domain truncation parameter. By removing the singularity and applying equations (2.2.23), (D.11) and (D.12) to approximate the contribution from the far-field, equation (4.2.3) yields

$$\begin{aligned} I_1(\phi) \approx \frac{1}{2}\int_0^{\phi_{\mathrm{m}}} \coth(\pi(\hat{\phi}+\phi)/2)(\theta_s(\hat{\phi})+\theta_s(\phi))\,\mathrm{d}\hat{\phi} \\ + \frac{1}{2}\int_0^{\phi_{\mathrm{m}}} \coth(\pi(\hat{\phi}-\phi)/2)(\theta_s(\hat{\phi})-\theta_s(\phi))\,\mathrm{d}\hat{\phi} + \frac{\theta_s(\phi)}{\pi}\ln\left|\frac{\sinh(\pi(\phi_{\mathrm{m}}-\phi)/2)}{\sinh(\pi(\phi_{\mathrm{m}}+\phi)/2)}\right| \\ + \int_{\phi_{\mathrm{m}}}^{\infty} \arctan\left(\frac{De^{-\lambda_0\hat{\phi}}\sin\lambda_0}{1+De^{-\lambda_0\hat{\phi}}\cos\lambda_0}\right)\frac{e^{\pi\hat{\phi}}}{e^{\pi\hat{\phi}}-e^{\pi\phi}}\,\mathrm{d}\hat{\phi} \\ + \int_{-\infty}^{-\phi_{\mathrm{m}}} \arctan\left(\frac{-De^{\lambda_0\hat{\phi}}\sin\lambda_0}{1+De^{\lambda_0\hat{\phi}}\cos\lambda_0}\right)\frac{e^{\pi\hat{\phi}}}{e^{\pi\hat{\phi}}-e^{\pi\phi}}\,\mathrm{d}\hat{\phi}. \quad (4.2.4) \end{aligned}$$

As per equation (3.2.1), the singular term is well-enough behaved provided the grid does not attempt to evaluate $I_1(\phi)$ for $\phi \approx \phi_{\mathrm{m}}$. As θ_s decays exponentially a larger value of ϕ_{m} helps reduce the chance of any difficulty associated with subtractive cancellation.

The last two integrals in (4.2.4) are the contributions from the far-field, which we denote as $I_3(\phi)$ and $I_4(\phi)$ respectively. A convenient expression in terms of special functions was not found for these terms, unlike the corresponding terms in the calculation of $u_s(\phi)$ given by (3.2.6). As there is no simple expression for the integral, the far-field terms are computed by converting the domain of integration to a finite interval using a change of variables, and applying standard numerical integration routines.

The mapping applied to the integral $I_3(\phi)$ can be viewed as two separate mappings, the first is simply returning to the α variable from (2.2.8), and then a second mapping is used to smooth the behaviour of the integrand and reduce the appearance of any sharp gradients. These mappings are given by

$$e^{\pi\hat{\phi}} = \hat{\alpha}(\hat{\xi}) = e^{\pi\phi_{\mathrm{m}}} + \frac{1-\hat{\xi}^{\gamma}}{\hat{\xi}^{\gamma}}.$$

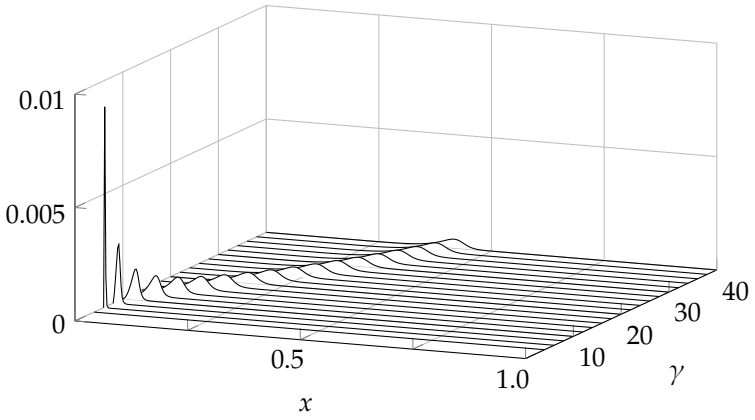

Figure 4.2.2: Integrand of I_3 from equation (4.2.4) after a transform from $\hat{\phi} \to \hat{\xi}$, for values $\phi = 10.9$, $D = 0.5$, $\lambda = 0.9$ and $\phi_m = 11$

By applying these mappings, the finite domain form of the integral is

$$I_3(\phi) = \frac{\gamma}{\pi} \int_0^1 \arctan\left(\frac{De^{-\lambda_0 \hat{\alpha}(\hat{\xi})/\pi} \sin \lambda_0}{1 + De^{-\lambda_0 \hat{\alpha}(\hat{\xi})/\pi} \cos \lambda_0} \right) \frac{1}{\hat{\alpha}(\hat{\xi}) - e^{\pi\phi}} \frac{1}{\hat{\xi}^{\gamma+1}} \, \mathrm{d}\hat{\xi}. \tag{4.2.5}$$

The integrand from the preceding equation is shown for varying γ in figure 4.2.2 to determine its sensitivity to changes in γ. For a typical value of ϕ_m, λ and a value of ϕ close to ϕ_m (where the integrand obtains steeper gradients), the behaviour of the integrand over the domain appears reasonable for $\gamma > 10$. Based on this observation, we chose to use a value of $\gamma = 25$ for the calculations in this chapter.

The mapping for the integral $I_4(\phi)$ is simply a mapping back to the α variable, $e^{\pi\hat{\phi}} = \hat{\alpha}$. Using this change of variables in the expression for $I_4(\phi)$ we obtain

$$I_4(\phi) = \frac{1}{\pi} \int_0^{e^{-\pi\phi_m}} \arctan\left(\frac{-De^{\lambda_0 \hat{\alpha}/\pi} \sin \lambda_0}{1 + De^{\lambda_0 \hat{\alpha}/\pi} \cos \lambda_0} \right) \frac{1}{\hat{\alpha} - e^{\pi\phi}} \, \mathrm{d}\hat{\alpha}. \tag{4.2.6}$$

This integrand displayed smooth behaviour and manageable gradients for typical values of D, λ_0 and ϕ_m, and for all values of ϕ required by the system of equations.

Equations (4.2.5) and (4.2.6) were efficiently computed with a relative error of 10^{-7} using adaptive 21-point Gauss-Kronrod quadrature methods supplied by GSL [24], requiring about three hundred function evaluations or less.

The topography given by (2.1.3) could be solved for by applying a similar discretisation scheme and iterative procedure as for the free surface, however this is considered computationally expensive. Rather than specify an exact topography, we approximate $\theta_b(\phi)$ as given in (2.1.3) in a way that retains two key properties; the general appearance of a smooth trench or a bump, and the width of the disturbance must be approximately constant when l is fixed. We now outline the method to compute the non-principal value integral $I_2(\phi)$ in (4.2.3). The precise shape for the topography given by equation (2.1.3) is not important in what follows, so some approximations are made such that an efficient expression is found for the function $\theta_b(\phi)$ which is seen in the expression for $I_2(\phi)$. The approximations used maintain the important features of the topographical disturbance such as its localisation and the general trench or bump-like appearance.

First we utilise the approximation that in equation (2.1.3) the variable x can be replaced by ϕ to a reasonable degree of accuracy, particularly when the topography has small curvature. Using this substitution we obtain

$$\sigma(\phi) = \frac{A}{2l}\left(\tanh S(\phi + \phi_c) - \tanh S(\phi - \phi_c)\right), \tag{4.2.7}$$

where the unknown quantity ϕ_c is the location of the downstream point of inflexion in the topography. To maintain the localised nature of the disturbance the following equation must be satisfied

$$x_b(\pm\phi_c) = \pm l/2. \tag{4.2.8}$$

The angle of the topography θ_b is then approximated by using the approximation $\frac{\mathrm{d}}{\mathrm{d}x}\sigma(x) \approx \frac{\mathrm{d}}{\mathrm{d}\phi}\sigma(\phi)$, thus

$$\theta_b(\phi) \approx \arctan\left(\frac{\mathrm{d}\sigma}{\mathrm{d}\phi}\right). \tag{4.2.9}$$

The precise shape of the topography will now come as part of the solution to the free surface, rather than being specified by (2.1.3). However, the value of ϕ_c

must be found as part of the solution, and so (4.2.8) should be included in our system of equations. For this reason the calculation of $x_b(\phi_c)$ is required, and the numerical method we use for this is outlined in §4.2.1.

Given that we now specify the topography using (4.2.9), the expression for $I_2(\phi)$ is

$$I_2(\phi) = \int_{-\infty}^{\infty} \arctan\left(\frac{AS}{2l}\left[\operatorname{sech}^2 S(\hat{\phi}+\phi_c) - \operatorname{sech}^2 S(\hat{\phi}-\phi_c)\right]\right) \frac{e^{\pi\hat{\phi}}}{e^{\pi\hat{\phi}}+e^{\pi\phi}}\,\mathrm{d}\hat{\phi}. \tag{4.2.10}$$

The integral in equation (4.2.10) is non-singular and is evaluated, like $I_3(\phi)$ and $I_4(\phi)$, by using a mapping to a finite domain, $\tilde{\xi} \in [-1, 1]$. The mapping used for this is given by

$$\hat{\phi}(\tilde{\xi}) = \frac{\phi_c \tanh^{-1}(\tilde{\xi})}{\tanh^{-1}(1/2)}.$$

This has the property that $\tilde{\xi} = \pm 1/2 \mapsto \hat{\phi} = \pm\phi_c$, which assists in maintaining the general shape of the integrand for all values of ϕ_c. A typical calculation may have parameter values $\phi_c = 0.5$, $S = 10$ and $A = 0.1$. The integrand from (4.2.10) is evaluated at varying ϕ for these parameter values in figure 4.2.3, demonstrating the behaviour of the integrand in the finite domain. Using the same adaptive Gauss-Kronrod routine, the integral can be computed with a relative error of 10^{-7} typically using three hundred function evaluations or less.

4.2.1 Inflexion point of topography

The value of $x_b(\phi_c)$ is computed using the analogue of equation (2.2.11) for the topography, namely

$$x_b(\phi_c) = \int_0^{\phi_c} e^{-\tau_b(\phi)} \cos\theta_b(\phi)\,\mathrm{d}\phi. \tag{4.2.11}$$

The integrand is the product of two factors, $e^{-\tau_b(\phi)}$ which can be evaluated

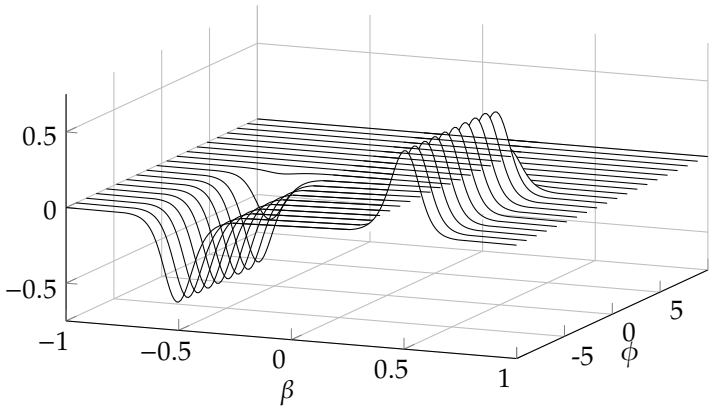

Figure 4.2.3: Plot of the integrand of (4.2.10) after transforming from $\hat{\phi} \to \tilde{\xi}$ for $\phi_c = 0.5$, $S = 10$ and $A = 0.1$

using the boundary integral result given by (2.2.21), and $\theta_b(\phi)$ which is given by equation (4.2.9).

Using equation (2.2.21), we find

$$\tau_b(\phi) = \underbrace{\int_{-\infty}^{\infty} \frac{\theta_s(\hat{\phi})}{e^{\pi\hat{\phi}} + e^{\pi\phi}} e^{\pi\hat{\phi}} \, \mathrm{d}\hat{\phi}}_{I_5(\phi)} - \underbrace{\fint_{-\infty}^{\infty} \frac{\theta_b(\hat{\phi})}{e^{\pi\hat{\phi}} - e^{\pi\phi}} e^{\pi\hat{\phi}} \, \mathrm{d}\hat{\phi}}_{I_6(\phi)}. \tag{4.2.12}$$

The first integral $I_5(\phi)$ is a non-principal-value integral and is evaluated by using the trapezoidal rule over the truncated domain determined by the computational grid discussed in §4.2.2. The contributions from both far upstream and far downstream are given by mapping the semi-infinite domains to a finite domain and applying the linearised result for θ_s. The mappings used are the same used to derive equations (4.2.5) and (4.2.5) for $I_3(\phi)$ and $I_4(\phi)$ respectively.

The second integral $I_6(\phi)$ is a principal-value integral and is evaluated by truncating the domain and removing the singularity. There is considerable freedom for choosing the truncated domain, as unlike the integrals over the free surface, the angle of the topography is known for all $\phi \in \mathbb{R}$. For this integral the truncation is chosen so that the contributions from far upstream and far downstream

are negligible, and no effort is spent on mapping the semi-infinite upstream or downstream domains. The domain is truncated at $\phi_n = \max(2\phi_c, \phi_m)$, that is either at the usual limit from the computational domain of the free surface, or at least twice as far in ϕ from the inflexion of the topography, whichever is greater. The truncated integral is then computed using standard routines supplied by GSL.

4.2.2 Numerical procedure

An algebraic system of equations is formed by equating the dynamic boundary condition (2.2.12) evaluated at the mid-points $\phi_{i+1/2}$ with the same equation evaluated at the final point $\phi_{N-1/2}$. We again use the regular grid in the variable β (and hence an irregular grid in ϕ) given by equations (3.2.7)–(3.2.9). Using the transformed velocity τ_s the equations are

$$\left[\exp(2\tau_s(\phi)) + \frac{2}{F^2} y_s(\phi)\right]_{\phi=\phi_{N-1/2}}^{\phi=\phi_{i+1/2}} = 0 \tag{4.2.13}$$

for $i = 0, 1, \ldots, N-2$, using $p \equiv 0$ on the free surface.

The values of $\tau_s(\phi_{i+1/2})$ for $i = 0, 1, \ldots, N-1$ are calculated by applying the trapezoidal rule to the principal-value integral in (4.2.4) and evaluating the other terms as outlined in the previous subsections. As there is no fixed value of $y_s(\phi)$, the quantity $y_s(\phi_{i+1/2}) - y_s(\phi_{N-1/2})$ is calculated via the mid-point rule and averaging, the same approach taken to derive equation (3.2.12). The resulting expression is;

$$\begin{aligned} y_s(\phi_{i+1/2}) - y_s(\phi_{N-1/2}) \approx{}& \frac{1}{4}\exp(-\tau_s(\phi_{i+1/2}))\sin(\theta_s(\phi_{i+1/2}))\varphi'(i+1/2) \\ &- \frac{1}{2}\sum_{j=i}^{N-2}\exp(-\tau_s(\phi_{j+1/2}))\sin(\theta_s(\phi_{j+1/2}))\varphi'(j+1/2) \\ &- \frac{1}{4}\exp(-\tau_s(\phi_{N-1/2}))\sin(\theta_s(\phi_{N-1/2}))\varphi'(N-1/2). \end{aligned}$$

The solution space of the algebraic system of equations is explored with the predictor-corrector method from §2.4. The correct number of unknowns and equations must be identified, with one more unknown than equations required by the predictor-corrector method. We fix the steepness parameter for the topography, and the distance between the inflexion points of the topography, so $S = 10$ and $l = 1$ is used throughout this chapter. The choice for l ensures that the width of the topographical disturbance is similar to the width in the pressure-disturbance calculations from Chapter 3. The clustering parameter for the irregular grid δ is fixed at 0.01 again, as in Chapter 3.

For solution branches with a fixed value of F, presented in §4.3, the unknowns in the system are the amplitude of forcing A, the topography parameter ϕ_c, the quantities D and λ_0 from the linearised far-field solution, the angle of the free surface $\theta_s(\phi_i)$ for $i = 1, \ldots, N$, where $\theta_s(\phi_0 = 0) = 0$ is already known due to symmetry, and the unknowns required by the transform $\varphi(\beta)$ from §2.3.1, $\lambda_{[j]}$. There are thus $N + 4$ unknowns, excluding the $\lambda_{[j]}$ that vary in number depending on the number of crests.

The first $N + 2$ equations in the system are; the $N - 1$ equations (4.2.13); two equations matching the linearised solution for $\theta_s(\phi_{N-1/2})$ and $\theta_s(\phi_{N-3/2})$ given by (3.2.4); and the equation for λ_0 given by (3.2.5). To make $N + 3$ equations, the equation which ensures localised topography, (4.2.8), is included in the system. The system also has one equation for each $\lambda_{[j]}$, given by equation (2.3.26), thus maintaining one more unknown than equations as required.

As before, two-crest solutions are detected along these fixed-F branches by searching for any i such that $\theta_s(\phi_{i+1})\theta_s(\phi_i) < 0$ with $\theta_s(\phi_i) > 0$. When this occurs, the solution for which an additional crest was detected is interpolated onto a new grid with the extra unknown $\phi_{[2]}$ and the extra equation $\theta_s(\phi_{[2]}) = 0$, and the continuation algorithm proceeds from this starting point for the new system

of equations.

There are two other types of solution branch which are used to examine the solution space. Branches with fixed amplitude of forcing A are computed using the same system of equations as above by allowing F to be an unknown that is determined as part of the solution. The almost-highest branches, those with a small velocity at the crest, are computed by allowing both A and F considered unknown, and the equation $u_{\min} - \min_i e^{\tau_s(\phi_i)} \cos\theta_s(\phi_i) = 0$ is included in the system with $u_{\min}$ a fixed constant.

4.3 Results

The solutions for the fully nonlinear model of a flow with a topographical disturbance are classified using the counterparts from the weakly nonlinear theory. The solution space is explored in the $(\hat{A}, \eta(0))$-plane, where $\hat{A}$ is the area of the topographical disturbance. The weakly nonlinear theory predicts that the topographical disturbance will behave the same as the pressure disturbance for F close to one. This is found to be true for the nonlinear solutions, and is a useful starting point for navigating the nonlinear solution space of the topographical disturbances.

The area of the topographical disturbance, $\hat{A}$, is given by

$$\hat{A} = \int_{-\infty}^{\infty} y_b(\phi)\,\mathrm{d}\phi. \tag{4.3.14}$$

The parameter $\hat{A}$ is calculated after the free surface has been found. The right-hand-side of equation (4.3.14) is calculated numerically by applying domain truncation and adaptive Gauss-Kronrod quadrature (supplied by GSL) to the equation

$$y_b(\phi) = \int_{-\infty}^{\phi} e^{-\tau_b(\phi)} \sin\theta_b(\phi)\,\mathrm{d}\phi.$$

The $\tau_b(\phi)$ term in the above integrand is evaluated as discussed in §4.2.1.

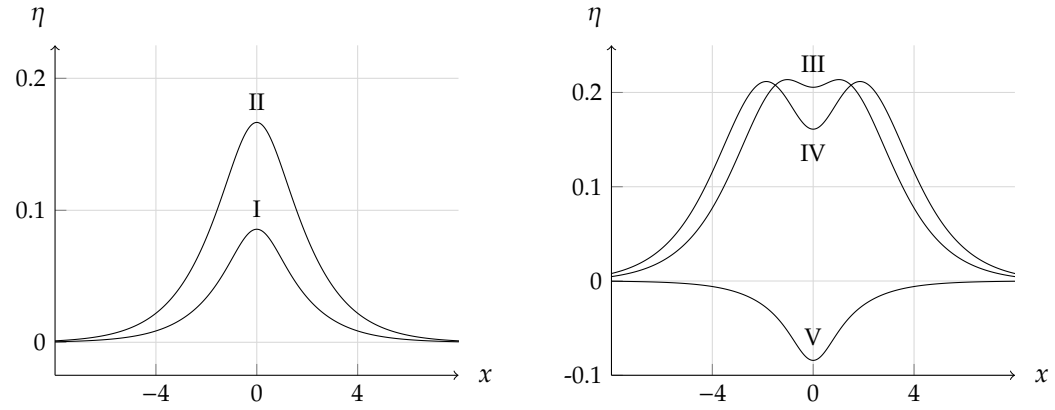

Figure 4.3.4: Forced solitary waves past topographical disturbances with $F = 1.1$. Shown are (a) nonlinear profiles of type-I and type-II waves for $\hat{A} = 0.04$, and $\eta(0) = 0.0858$ and 0.167 respectively, and (b) nonlinear profiles of waves of type III, IV and V for $\hat{A} = -0.07$, and $\eta(0) = 0.206, 0.162$ and -0.0843 respectively.

We now recall the qualitatively different solution types. For a bump in the channel, when $\hat{A} > 0$, the weakly nonlinear theory predicts two types of solution, type I and II, which are a perturbation to a uniform stream and solitary wave respectively. An example of the nonlinear profiles of these two types of wave is shown in figure 4.3.4(a) for flow past a bump with amplitude of forcing $\hat{A} = 0.04$, with Froude number $F = 1.1$.

For a trench in the channel, when $\hat{A} < 0$, the weakly nonlinear theory predicts three qualitatively different types of solution, the cusped perturbation to a solitary wave, the perturbation to two solitary waves and the dip-like perturbation to a uniform stream, these are type III, IV and V respectively. Nonlinear examples of these obtained by the boundary-integral method are shown in figure 4.3.4(b) for flow past a trench with an amplitude of forcing $\hat{A} = -0.07$ and Froude number $F = 1.1$.

4.3.1 Fully nonlinear solution space

Each panel in figure 4.3.5(a)–(d) shows two sets of solutions for a fixed value of F plotted as curves in the $(\hat{A}, \eta(0))$-plane, obtained from the nonlinear (solid curve) and weakly nonlinear (dotted curve) calculations. Just as for the flow past a pressure disturbance, the number of parameters in the fully nonlinear and weakly nonlinear systems match. In addition to the fixed-F branches, the set of almost-highest solutions with a fixed small velocity, $|u| \approx 0.03$, at the crest are shown as dashed curves in figures 4.3.5(a)–(d).

The solution space when $F = 1.1$ is presented in figure 4.3.5(a), with the different solution types identified in the weakly nonlinear theory indicated by circular markers. The corresponding free-surface profiles are plotted in figure 4.3.4(a) and (b). The location of the different solution types I–V, at least qualitatively, is very similar to the flow with $F = 1.26$ past a pressure disturbance shown in the previous chapter in figure 3.3.5(a).

For very deep trenches, a difference in the amplitude of forcing parameter $\hat{A}$ no longer corresponds to significant differences in the free-surface profile, imposing a limitation on the solution space we can explore in these results. The phenomenon is featured in figure 4.3.5(b) and (c), where $F = 1.16$ and $F = 1.24$ respectively, by the near horizontal appearance of the fixed-F branch as the amplitude of forcing $|\hat{A}|$ grows. The near horizontal trend of the set of solutions in the $(\hat{A}, \eta(0))$-plane is also observed in the set of almost-highest solutions, plotted in figure 4.3.5(b)–(d), as the trench gets deeper.

The lack of influence on the free surface of increasingly deep trenches is demonstrated by comparing the free surface of a flow with an amplitude of forcing $\hat{A} = -0.5$, to that of a flow with a larger amplitude of forcing, $\hat{A} = -1.0$. Taking the Froude number to be $F = 1.16$ as an example, for each solution type, II, IV and V, two profiles with these differing amplitudes of forcing are marked on figure

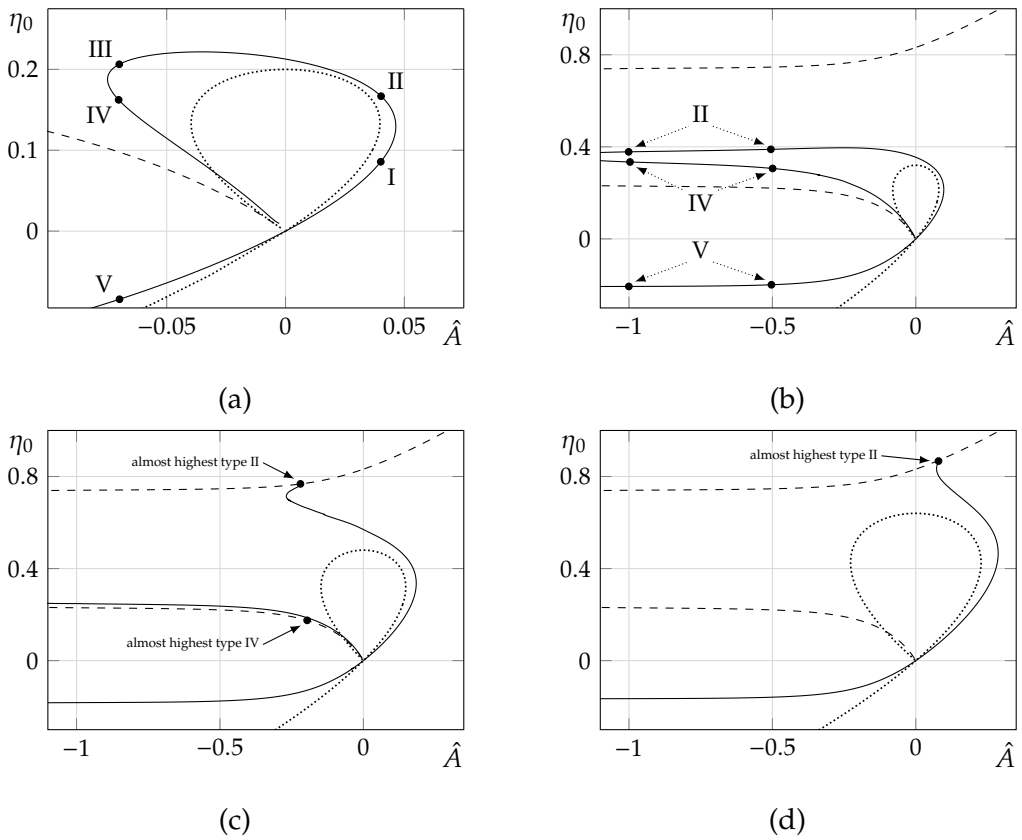

Figure 4.3.5: Plots of the variation of $\eta(0)$ versus forcing amplitude $\hat{A}$ for the four values of Froude number $F = \{1.10, 1.16, 1.24, 1.32\}$. The solid curves are derived from the fully nonlinear calculations. The dotted curves indicate values derived from the weakly nonlinear analysis. The dashed curves in (b)–(d) are the locus of the 'near-limiting' values, with $|u| = 0.03$ at the wave crests. The markers in (a) indicate the location in parameter space of the five types of forced solution shown in figure 4.3.4, whereas in (b) they identify the free-surface flows shown in figure 4.3.6(c)–(b), and in (c) and (d) all markers denote forced almost-highest solitary waves.

4.3.5(b). The difference in the displacement of the free surface at the centre of the wave is small within solution types, roughly 3%, 9% and 4% for types II, IV and V respectively.

The free-surface profile, channel topography and interior streamlines of these solutions are plotted in figure 4.3.6(c)– (b). The streamlines were calculated using the method outlined in Appendix E, using the fully nonlinear solution for the free surface. The flow for a smaller trench is shown with solid lines, while the flow past a deeper trench is plotted as dashed curves. The difference in the topography is visibly larger than the differences observed in the streamlines of each flow. This indicates that, for deep trenches, the topography has limited influence on the flow except in the region where ψ is small, that is, the flow very near the topography.

As a result of this behaviour when the trench is deep, the solution space when $1.16 \leq F \leq F_u$ extends into a region where the boundary-integral method requires a large and eventually impractical number of grid points to converge. In this region of the parameter space, the solution is no longer strongly influenced by the parameter $\hat{A}$ and so the system of equations gains, numerically, an extra degree of freedom. The additional degree of freedom in this deeper trench regime causes the corrector procedure to fail due to the fact that the solution no longer corresponds to a regular point as required by the procedure, as discussed in §2.4. Converged solutions were found for trenches with amplitude up to $\hat{A} \approx -1.1$.

In theory, a larger number of grid points could compute more of the solution space with this method, although there are other physical reasons for not pursuing this. In most physical flows, a boundary layer where viscous effects are present would form near the topography, which may or may not remain attached depending on the topography. In the case of these more extreme topographical disturbances, it is expected that the boundary layer would separate at the upstream corner. This separation would create a large region where viscous effects

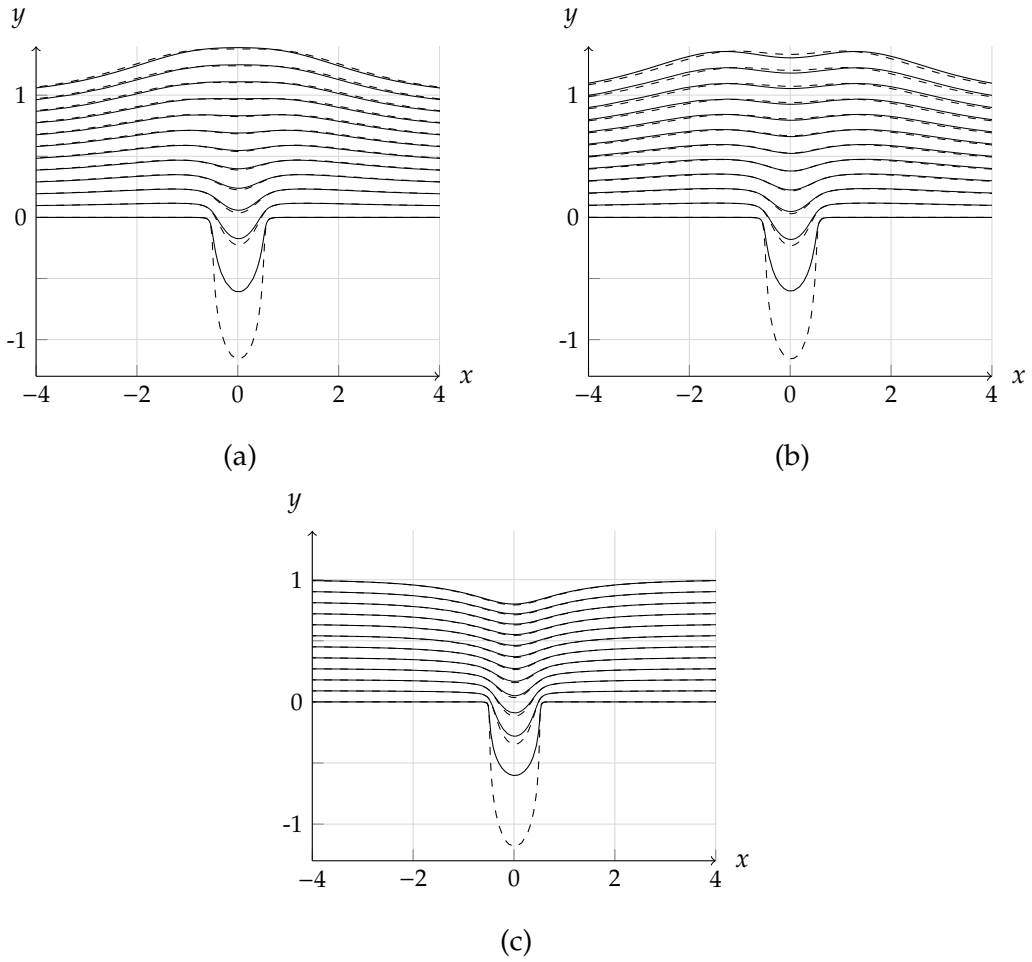

Figure 4.3.6: Nonlinear free-surface profile, topography and interior streamlines for three types of flow with $F = 1.16$. Plotted in (a), (b) and (c) are the type II, IV and V flows, respectively, with solid curves corresponding to a flow with $\hat{A} = -0.5$ and dashed curves to a flow with $\hat{A} = -1.0$.

are important, fundamentally changing the flow, and this is not modelled by a potential flow model. Another possibility is that the flow becomes subcritical in the very deep trench, although this type of bifurcation was not detected in the region we were able to compute.

In the flow past a pressure disturbance, the boundaries of the solution space were generally determined by almost-highest solutions, and so we discuss these next.

The almost-highest branches, shown as dashed curves in figure 4.3.5(a)–(d), contain either perturbations to a single solitary wave, type II, along the upper branch, or a perturbation to two solitary waves, type IV, along the lower branch. No approach towards a limiting configuration was made by solutions which were considered a perturbation to a single solitary wave with a cusp and two peaks, a type-III solution. We suggest that the main reason the almost-highest type-III waves were not observed is due to the fact that, in general, a cusp was not present at the crest of a solution unless the trench was sufficiently deep. Type-II waves persist for flow past a trench along the fixed-F branches in figures 4.3.5(a)–(c) as the branches continue into the $\hat{A} < 0$ half-plane. Once the local maximum of $\eta(0)$ is reached along that branch, the solutions with a cusp appear, an example of which is indicated by a circular marking on the $F = 1.1$ branch from figure 4.3.5(a), with corresponding profile shown in figure 4.3.4(b). It is possible that if more of the solution space were available, a type-III almost-highest solution could be observed.

Almost-highest type-II waves for flow past a trench are found to exist for $1.22 < F < F_u$. The value of F for the type-II almost-highest waves is given by $F \approx \sqrt{2\eta(0)}$. At $F \approx F_u$ the almost-highest solution is on the $\hat{A} = 0$ axis, and the value of F decreases as the almost-highest branch is followed in figure 4.3.5(c) into the $\hat{A} < 0$ half-plane. At the circular marker shown in figure 4.3.5(c), the value

of the Froude number is $F = 1.24$, and the Froude number reaches $F = 1.22$ at $\hat{A} = -1.1$. The almost-highest branch likely extends beyond $\hat{A} < -1.1$, and as we were unable to evaluate trenches of this depth, the range of values of $F < 1.22$ such that these almost-highest type-II waves exist were not established by these results. Again, starting from the unforced almost-highest solution and proceeding along the almost-highest branch to the right, the value of F is now increasing from $F \approx F_u$. At the circular marker in figure 4.3.5(d) the value of F is 1.32. It is inferred that almost-highest waves past a bump exist for all $F > F_u$.

The variation of F is very small for the almost-highest type-IV waves compared to the type-II case. At the circular marker shown on the lower branch in figure 4.3.5(c), the value of F is 1.2906, and towards the origin the value of F approaches $F_u = 1.2909$. The reason that F remains very close to F_u for the type-IV waves is because the two crests are at some distance from disturbance, and so are locally very similar to the unforced limiting configuration, as for the same type of waves in flow past a pressure disturbance. Like the type-II almost-highest waves, this branch extends into the region of deep trenches, and so it was not possible to establish all the values of F for which the almost-highest type-IV waves exist.

The space of solutions for flow past a bump is relatively straightforward. The type-I waves were found for all values of F shown in figure 4.3.5(a)–(d), and for each fixed value of F they exist for all values of $\hat{A}$ before the turning point in the branch where the solutions are then classified as type II. This is qualitatively consistent with the results of the weakly non-linear analysis.

For flow past a trench, no type-III solutions were found for $F > 1.16$, and no type-IV solutions were found for $F > F_u$. The result for the type-IV waves is consistent with those for the pressure disturbance, as the two crests reach a limiting configuration at $F \approx F_u$. The type-V solutions are found by following the fixed-F branch from the origin of panels 4.3.5(a)–(d) into the lower half-plane

where $\eta(0) < 0$. These solutions do not approach a limiting configuration as $|\hat{A}| \to \infty$ and according to the weakly nonlinear analysis should exist for all values of $\hat{A} < 0$. Here converged nonlinear solutions were found for $\hat{A} > -1.2$ for all the values of F shown.

We note that the weakly nonlinear theory does not perform as well for flow past a bump or trench as it did for the flow past a pressure disturbance. This can be attributed to two assumptions in the derivation of the fKdV equation (2.5.35) with the jump condition (2.5.34). Firstly, Lee *et al.* [36] found that at higher order the topographical disturbance introduces additional dispersive effects that the pressure disturbance does not experience in a generalised-Boussinesq model, and that the pressure disturbance has a larger influence on the free surface than a topographical disturbance for forcings that are considered equivalent in the lower order fKdV model. In effect, the balance of nonlinearity and dispersion assumed in the derivation of the fKdV for a topographical disturbance does not remain valid for as large a region of the solution space. Secondly, the fKdV equation requires that the amplitude of forcing is small compared to the wave height, which is not true for flow past a deep trench.

The detail of the solution space near the almost-highest waves is presented in figures 4.3.7–4.3.9. We find that topographical disturbances also admit non-uniqueness for a fixed value of the original forcing parameter A. We chose to fix the parameter A rather than the area of the topography $|\hat{A}|$ in order to reduce computational effort. For these branches finding the free-surface profiles required a considerable number of grid points, up to $N = 1600$, and the additional equation to compute $\hat{A}$ proved too costly. It was checked that the variation on $\hat{A}$ was small, in the third significant digit, and did not alter the qualitative nature of the results.

The almost-highest solutions presented in figures 4.3.7–4.3.9 were computed using solutions to the free-surface found in figure 4.3.5(c)–(d) as starting points.

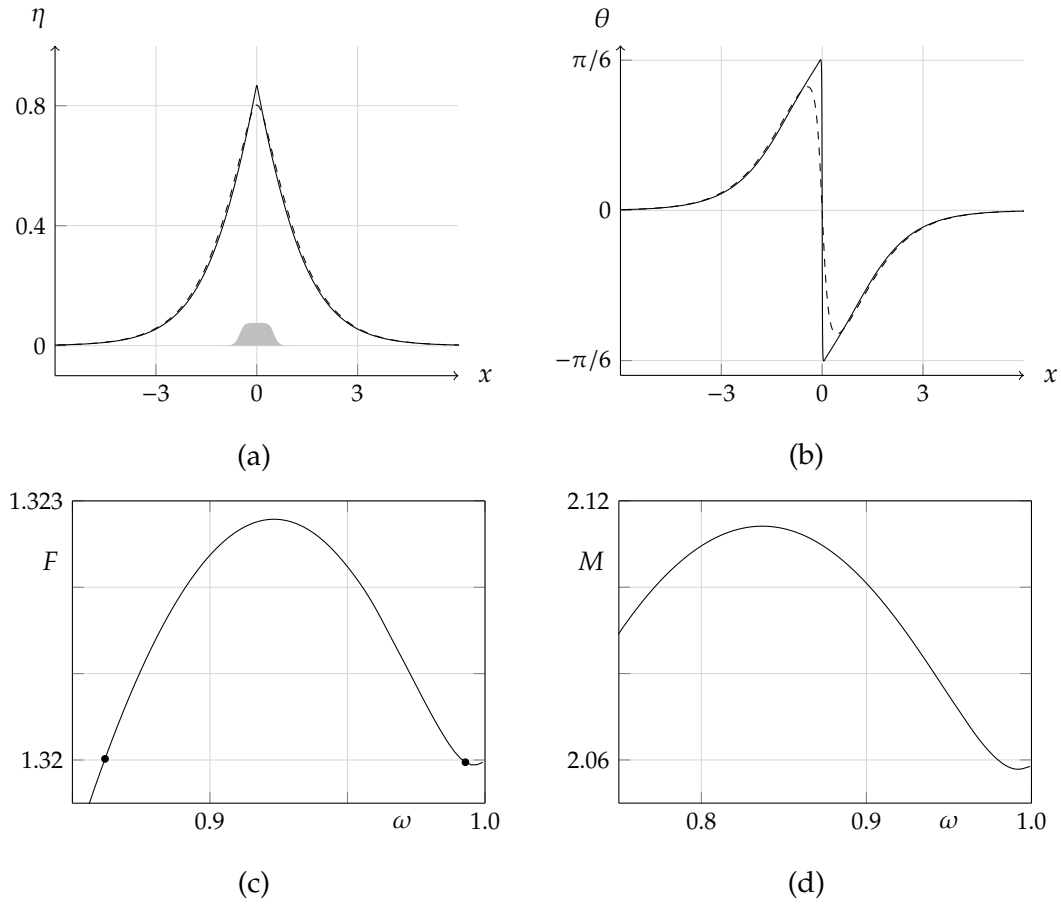

Figure 4.3.7: Forced solitary wave of type II with the area of the topography being $\hat{A} = 0.079$. Shown are (a) nonlinear profiles for a value of the Froude number $F = 1.32$, solid and dashed curves are for values of $\omega = 0.993$ and $\omega = 0.862$, respectively, shaded region shows the topography located at $y = 0$; (b) Plot of θ versus x for (a); (c) and (d) plots of the Froude number F and wave mass M versus ω, respectively, markers in (c) indicate the location of the profiles shown in (a).

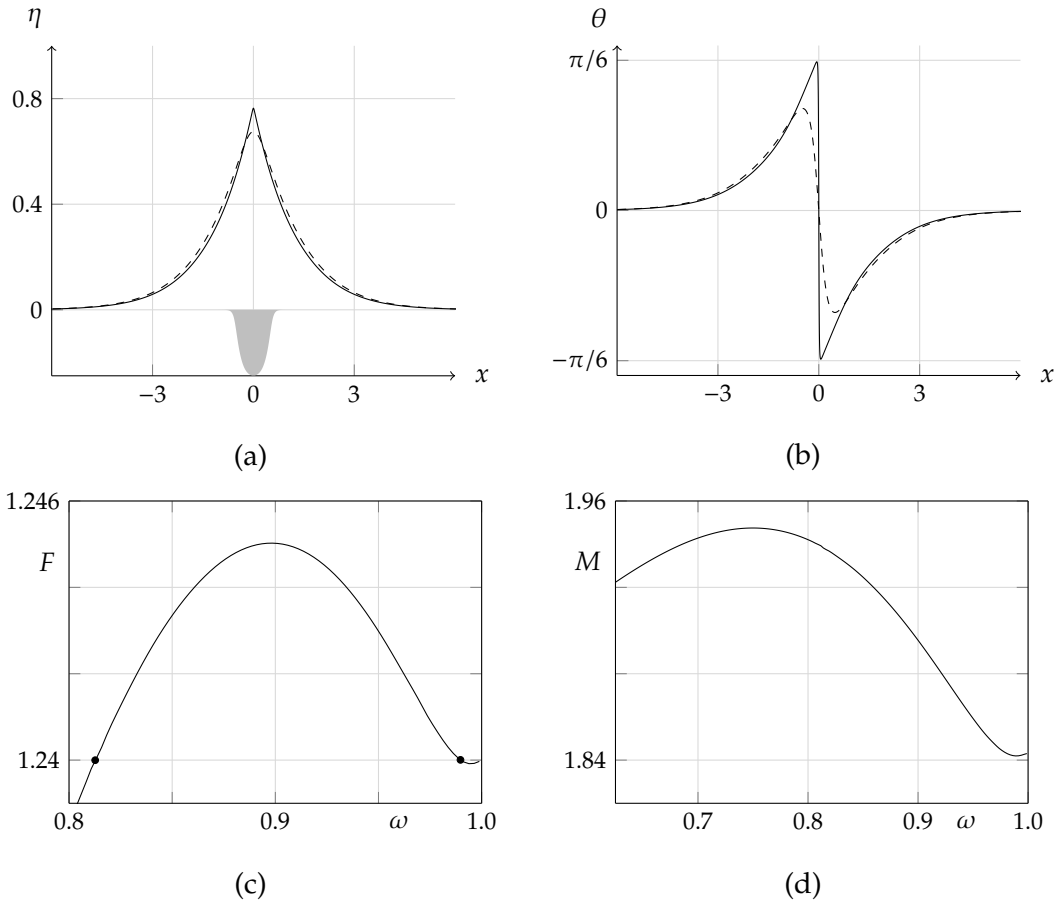

Figure 4.3.8: Forced solitary wave of type II with the area of the trench being $\hat{A} = 0.22$. This type of solution is not predicted by the weakly nonlinear analysis. Shown are (a) nonlinear profiles for a value of the Froude number $F = 1.24$, solid and dashed curves are for values of $\omega = 0.990$ and $\omega = 0.813$, respectively, shaded region shows the topography located at $y = 0$; (b) Plot of θ_s versus x for (a); (c) and (d) plots of the Froude number F and wave mass M versus ω, respectively, markers in (c) indicate the location of the profiles shown in (a).

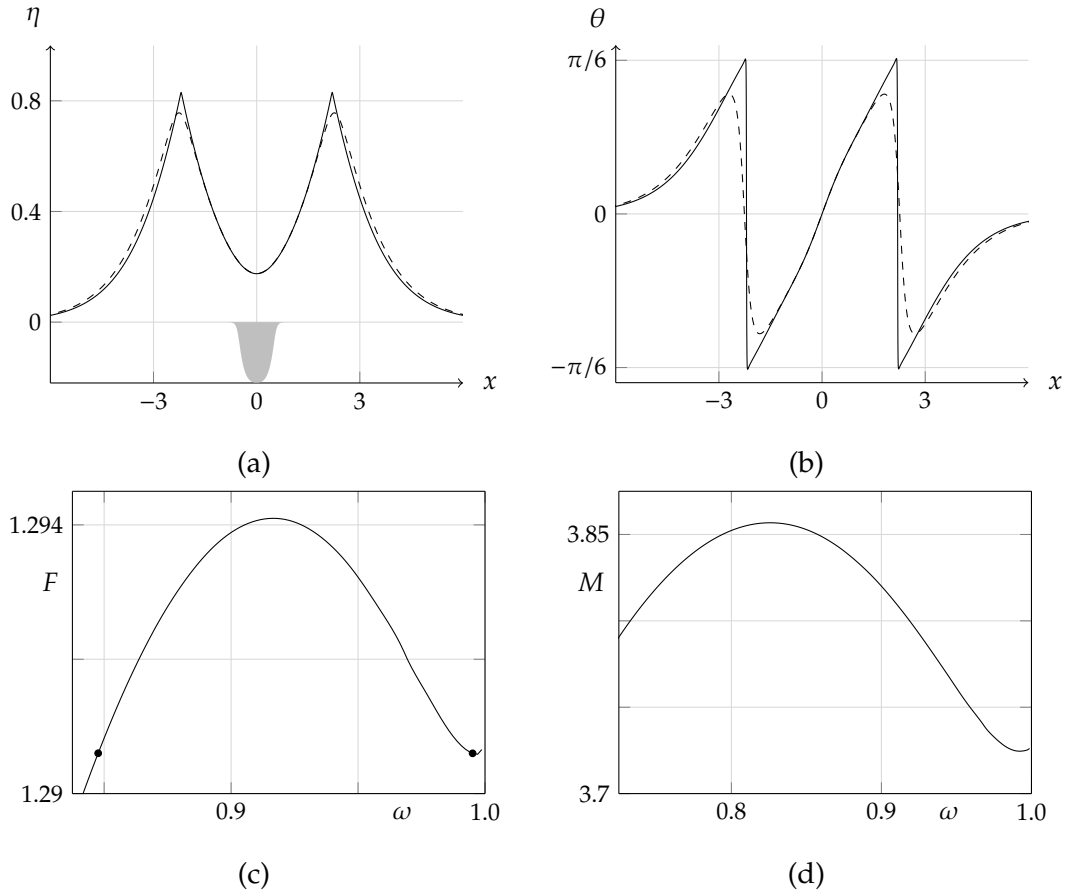

Figure 4.3.9: Forced solitary wave of type IV with the area of the trench being $\hat{A} = 0.196$. Shown are (a) nonlinear profiles for a value of the Froude number $F = 1.2906$, solid and dashed curves are for values of $\omega = 0.995$ and $\omega = 0.848$, respectively shaded region shows the topography located at $y = 0$; (b) Plot of θ_s versus x for (a); (c) and (d) plots of the Froude number F and wave mass M versus ω, respectively, markers in (c) indicate the location of the profiles shown in (a).

The layout of the panels (a)–(d) in figure 4.3.7–4.3.9 is similar to the corresponding results for the almost-highest waves presented in figures figure 3.3.7–3.3.10 from the previous chapter. Respectively the panels (a)–(d) contain; plots of the free-surface elevation for two nonlinear waves with the same value of F but different values of the parameter ω defined by equation (3.3.15); a plot of the angle of the two free surfaces from panel (a); a plot of the value of the Froude number F versus ω for the almost-highest waves; and a plot of the mass M of the wave versus ω for the almost-highest waves. The mass of the wave for flow past topography is defined here as

$$M = \int_{-\infty}^{\infty} \eta \, \mathrm{d}x,$$

which is calculated by applying the trapezoidal rule to the free surface over the truncated domain.

To locate these solutions in figure 4.3.5, note that the profiles plotted as solid lines in figure 4.3.8(a) and figure 4.3.9(a) are indicated respectively by the upper and lower circular markers in figure 4.3.5(c), while the solid-line profile in figure 4.3.7(a) corresponds to the circular marker in figure 4.3.5(d).

As with the unforced flow and the flow past a pressure disturbance, the perturbations to solitary waves for a flow past a trench approach the Stokes limiting configuration of an included angle of 120° and a stagnation point at their crest as the re-scaled wave-height ω approaches one. The included angle at the crest of 120° is observed in the plot of the angle given by the solid line in figures 4.3.7–4.3.9(b), where a rapid change in the angle from $\pi/6$ to $-\pi/6$ at the location of the crests is observed.

The oscillatory behaviour of the variables F and M with respect to a parameter such as ω has now been observed in the solutions for flow past topography, see figures 4.3.7–4.3.9(c) and (d). Two local extrema were observed for both F and

M for all types of forced solution as $\omega \to 1$. Further local extrema could, in theory, be computed with more grid points, however whether infinitely many local extrema exist or not cannot be determined by these numerical results. It was also found that the location of the extrema for the type-IV solution were the same to three significant figures as for unforced flow, providing further evidence that the behaviour at the crest for this type of solution is not heavily influenced by the topographical disturbance.

4.4 Conclusion

The fully nonlinear solution space for symmetric supercritical flow past topographical disturbances was explored, except in the regime of very deep trenches which could not be computed. Given a unit-width disturbance, for a fixed value of F the set of solutions in the $(\hat{A}, \eta(0))$-plane consisted of either one or two branches of solution.

For $1 < F < 1.16$ there was one connected branch, as shown in figure 4.3.5(a), containing all five types of solution. For $F > 1.16$ no type-III waves were observed, and for $F > F_u$ no type-IV waves were observed. For $1.16 \leq F \leq 1.22$ there are two branches (see figure 4.3.5(b)), both extending into the region of deep trenches. The type-IV solutions were found on an isolated branch, while the other branch contained waves of types I, II and V. For $1.22 < F \leq F_u$ there are also two branches, shown for $F = 1.24$ in figure 4.3.5(c), both extending into the domain of deep trenches. The type-IV solutions, again, were found on an isolated branch from the rest of the solutions, while the other branch ends at a type-II solution with a limiting configuration. For $F > F_u$, shown for $F = 1.32$ in figure 4.3.5(c), there was a single branch which contained solutions of type I, II and V, ending at a type-II wave with $\hat{A} > 0$ with a limiting configuration. All the type-V solutions extend

into the domain of very deep trenches, and it is suggested that they exist for all $\hat{A} < 0$.

The reason that the waves past a deep trench could not be determined by this method is due to the fact that free surface was no longer strongly influenced by the parameter $\hat{A}$ for such a trench, see figure 4.3.6. The system of equations gains, numerically, an extra degree of freedom in this regime, and so fails to converge. There is an additional physical consideration in the deep trench regime, that is the presence of large velocities near the boundary, suggesting a boundary layer would form in this flow which would then require viscous effects to model. The presence of a bifurcation such as the flow becoming subcritical in the trench was not observed, but is posed as another possible bifurcation in this regime.

Almost-highest type-II and type-IV waves were found. In contrast to the flow past a pressure disturbance, no almost-highest type-III waves were observed for flow past a trench. Similarly to the almost-highest unforced waves and the almost-highest waves due to a pressure disturbance, properties such as the Froude number and the mass of the wave pass through local maxima and minima as the wave-height is increased for the almost-highest presented in this chapter, see figures 4.3.7–4.3.9. These turning points in the flow quantities may also coincide with the presence of an instability, as per the unforced case Kataoka [32], Longuet-Higgins & Fox [40], Tanaka [60], which could be considered in future research.

Although the nonlinear results do depart considerably from the weakly nonlinear, the stability analysis in Chapter 5 is also relevant to the topographical disturbance case, particularly when the waves are not too steep and when the flow is close to critical, that is $F \approx 1$. A linearised analysis based on the method for unforced waves given by Tanaka [60] is discussed as future work in Chapter 6.

Chapter 5

Weakly nonlinear unsteady response to flow past forcing

5.1 Introduction

The time-dependent fKdV equation (2.5.31) is used in this chapter to investigate the stability of the solutions identified in Chapter 3 and 4 before they approach the Stokes limiting configuration. Here the forcing term is given by a Gaussian function as in equation (2.1.2).

The weakly nonlinear theory is capable of reproducing many of the key features of the fully nonlinear unsteady response, at least in the time-period before any wave-breaking phenomena are observed [13, 36, 26]. As covered in the introduction, one of the striking features of near critical forced flow is the generation of upstream propagating waves observed by Ertekin [22] and Wu [70]. This phenomenon has been observed using weakly nonlinear models and fully nonlinear models.

The stability analysis performed by Camassa & Wu [12] finds that the waves which are considered perturbations to uniform streams are stable using both

linearised as well as some nonlinear approaches, and that the forced perturbations to solitary waves with a single crest are unstable. Using weakly nonlinear theory the same result has been observed by Chardard *et al.* [14] and Grimshaw & Smyth [27]. Grimshaw & Maleewong [26] also confirm this behaviour, providing a comparison between the fully nonlinear evolution of the perturbation to a solitary wave with the behaviour predicted by weakly nonlinear theory. They found the two to be in good agreement for small disturbances with the Froude number close to unity.

The cusped and double-hump solutions, that is the type-III and type IV waves, to the fKdV model have not been previously considered, and so are investigated here in two ways. The first is to perturb the steady states by multiplying them by a constant close to one and then compute the evolution of the free surface. This is performed by discretising the fKdV equation, the same approach used by Chardard *et al.* [14], Grimshaw & Maleewong [26] and others (see references therein). A discrete Fourier method is employed to determine spatial derivatives, and time stepping is performed using the explicit fourth order Runge-Kutta formula. The details of this method are outlined in §5.2.

The second approach is to identify the presence of growing modes using a linearised perturbation analysis to determine if the steady solutions are linearly unstable. The perturbations obey an unforced KdV equation with a spatially varying coefficient; see Camassa & Wu [12], Ee & Clarke [18], given by (5.2.3). The associated eigenvalue and eigenfunction problem is then solved numerically on a discrete periodic grid by exploiting Fourier approximations to the derivatives using standard matrix methods, the same approach as was used by Ee & Clarke [18]. After the modes are determined, the accuracy of the linearised analysis is considered by using the fastest growing mode as a perturbation to the full fKdV system.

The first approach, presented in §5.3.1, finds that the negatively forced perturbations to solitary waves are unstable. The perturbed cusped waves, identified as type-III, coalesce then generate an upstream solitary wave. The same behaviour is also observed for the type-IV wave, which is a perturbation to two solitary waves, except in the case of an initial state which has enough energy to generate two upstream waves, rather than one upstream wave. The region near the forcing eventually attains the shape of the stable perturbation to a uniform stream.

The eigenvalues and eigenmodes and the response of the system to the fastest growing mode, identified by our linearised analysis, are discussed in §5.3.2. Eigenvalues with positive real part are found for all perturbations to one or two solitary waves. The rate of growth of the unsteady response is largest for the positively forced type-II wave, this causes the linearised analysis to break down at the earliest time of all the identified types of wave. The type-III wave has the slowest perturbation growth, and so the fKdV and the predicted linear growth agree while the cusp coalesces, while the fastest growing mode for a type-IV solution has similar growth rate to the positively forced solitary wave, and we find here that effects not accounted for by the linear solution are significant before the two waves coalesce.

Determination of the precise growth rates of the unstable modes for the waves of type III and IV using the linearised analysis is confounded when using a periodic domain as we have here. For these wave types, there is a decaying spatial oscillation present in the eigenmodes with non-zero real part. The rate of spatial decay may cause the oscillation to leak from the downstream domain into the upstream domain, making the eigenvalue and eigenmode sensitive to the choice of domain. The implications of this and possible future work is discussed in §5.4.

5.2 Formulation

5.2.1 Spectral collocation method for the time-dependent fKdV equation

The behaviour of the free surface as modelled by the fKdV equation (2.5.31) on the infinite domain is approximated by using a periodic domain. The spatial derivatives are approximated on a discrete periodic domain using a spectral collocation method and the discrete Fourier transform. Once an initial steady profile is found, an explicit time-stepping scheme is employed to simulate the unsteady flow.

Let η have period of $2W$, and take the spatial domain to be $[-W, W]$, so that the computational grid is given by

$$x_j = W(j - N)/N$$

for $j = 1, \ldots, 2N$.

An initial steady solution to the fKdV equation (2.5.31) with the Gaussian forcing is found by solving two boundary-value problems using the `chebfun` package Trefethen [63]. The first boundary-value problem is to find an 'inner' solution; the solution near the crest. The inner solution is then used for the second boundary-value problem, which is to find a solution on the larger and periodic domain. The initial guess for the inner solution is found by taking the forcing term to be a δ function with equivalent amplitude, resulting in the sharp crested or cusped solutions via the jump condition (2.5.34). The inner solution for the smooth Gaussian forcing function is then found using `chebfun`'s boundary-value problem (BVP) class with linearised boundary conditions.

In the second problem, periodic boundary conditions are imposed, and the solution is found using the same BVP solver supplied by `chebfun`. The initial guess

is given by extending the inner solution found above to the rest of the domain. This is achieved by matching it with the solution to the far-field linearised fKdV. Typically, we use a domain of width $W = 100$ or more so that the unsteady calculations are terminated before the waves propagating upstream and downstream approach the extents of the periodic domain.

The spectral derivative is approximated on the spatial grid using the discrete Fourier transform (DFT). The DFT of the function $\eta(x,t)$ is

$$\widehat{\eta}(k,t) = \sum_{j=1}^{2N} \eta(x_j,t)e^{-ikx_j}$$

for $-N+1 \leq k \leq N$. Let $s = \pi/W$, then by taking the discrete Fourier transform of the fKdV equation (2.5.31) an expression for $\widehat{\eta_t}$ is given by

$$\widehat{\eta_t} = s\left(\frac{1}{6}s^2\widehat{\mathrm{D}^3\eta} + \frac{3}{4}\widehat{\mathrm{D}\eta^2} - (F-1)\widehat{\mathrm{D}\eta} + \frac{1}{2}\widehat{\mathrm{D}p}\right) \tag{5.2.1}$$

for $-N+1 \leq k \leq N$ and $(\widehat{\mathrm{D}\eta})$ is the discrete spectral derivative of η. The nth-order spectral derivative is, for a suitable function $u(x)$, given by

$$(\widehat{\mathrm{D}^n u})(k) = \begin{cases} (ik)^n\widehat{u}(k), & k \neq N, \text{n even}, \\ (iN)^n\widehat{u}(N), & k = N, \text{n even}, \\ 0, & k = N, \text{n odd}, \end{cases} \tag{5.2.2}$$

for wavenumbers $-N+1 \leq k \leq N$ (see [62]).

Time stepping is performed by applying the fourth-order explicit Runge-Kutta method to generate $\widehat{\eta}(k, t_0+\Delta t)$ from the values given by $\widehat{\eta}(k,t_0)$ for a fixed, small time step of size Δt. That is, the profile is evolved in Fourier space rather than in the spatial domain. The fast Fourier transform (FFT) is used to find an initial profile in Fourier space $\widehat{\eta}(k,t_0)$, and at each time step all the spatial derivatives on the right-hand-side of the discrete form of the fKdV equation (5.2.1) are efficiently computed as per equation (5.2.2). The only term from the right-hand-side that

requires some extra effort is the $\widehat{\mathrm{D}\eta^2}$ term. This is calculated by applying the inverse FFT on $\widehat{\eta}(k, t_0)$, then taking the square of the result and applying the FFT to find $\widehat{\eta^2}(k, t_0)$, and finally applying the spectral derivative.

Both the spatial grid and the size of the time-steps were varied to check the independence of the resulting unsteady response. Calculations were done with different choices of period $2W$, N and different time steps Δt. Only the results shown obtained from the highest resolution grid, and with the smallest time-step attempted, are shown here.

5.2.2 Linearised stability analysis

The linearised stability analysis is formulated by introducing a small perturbation variable $C(x, t)$ such that $\eta(x, t) = \eta_s(x) + C(x, t)$ exists, where η_s is a solution to the steady fKdV equation (2.5.32);

$$\eta_{sxxx} + 9\eta_s\eta_{sx} - 6(F-1)\eta_{sx} = -3p_x.$$

By substituting $\eta = \eta_s + C$ and the above equation into the fKdV equation and linearising, the perturbation variable C must satisfy

$$6C_t - C_{xxx} - 9(C\eta_s)_x + 6(F-1)C_x = 0, \tag{5.2.3}$$

which can be written as

$$C_t = \mathcal{L}(C), \tag{5.2.4}$$

where the operator

$$\mathcal{L}\{\phi(x)\} = \frac{\partial}{\partial x}\left(\frac{1}{6}\frac{\partial^2\phi}{\partial x^2} + \frac{3}{2}\eta_s(x)\phi(x) - (F-1)\phi(x)\right); \tag{5.2.5}$$

noting that the problem here is treated with periodic boundary conditions on the finite domain $[-W, W]$, and that this is a non-self-adjoint operator.

As equation (5.2.4) is linear, separable solutions of the form $e^{\lambda t}X_\lambda(x)$ can be found, and then the general solution is given by a sum of eigenfunctions of $\mathcal{L}$, assuming the eigenfunctions form a basis in a suitable function space. Setting

$$C(x,t) = \sum_{\lambda\in\Lambda} e^{\lambda t}X_\lambda(x) \tag{5.2.6}$$

where Λ is the set of all the eigenvalues from the eigenvalue problem;

$$\lambda X_\lambda = \mathcal{L}\{X_\lambda\}. \tag{5.2.7}$$

When η_s is real and symmetric it can be shown from the definition of $\mathcal{L}$ that

$$\mathcal{L}\{\phi(-x)\} = -\mathcal{L}\{\phi(x)\} \quad \text{and} \quad \mathcal{L}\{\phi\}^* = \mathcal{L}\{\phi^*\}.$$

It then follows that if λ and $X_\lambda(x)$ are an eigenvalue and eigenfunction pair for the operator $\mathcal{L}$, then $-\lambda$ and $X_\lambda(-x)$ is also an eigenvalue and eigenfunction pair, and so are $\pm\lambda^*$ and $(X_\lambda(\pm x))^*$. So a symmetric solution η_s of the fKdV equation is linearly unstable whenever there is a non-zero real part for any eigenvalue of the associated operator $\mathcal{L}$.

The eigenvalues and eigenfunctions of $\mathcal{L}$ can be determined using standard matrix methods by assuming that the operator is well approximated by the discrete and finite dimensional form of the operator given by the spectral derivative matrix. Trefethen [62] provides the discrete form of the minimal oscillation (or band-limited) spectral derivative operator D_{ij} and the second derivative operator D^2_{ij} as;

$$D_{ij} = \begin{cases} \dfrac{\pi(-1)^{i-j}}{2W\tan(\pi(i-j)/2N)}, & i \neq j, \\ 0, & i = j; \end{cases}$$

$$D^2_{ij} = \begin{cases} \dfrac{-2\pi^2(-1)^{i-j}}{4W^2\sin^2(\pi(i-j)/2N)}, & i \neq j, \\ \dfrac{-2\pi^2(1+2N^2)}{12W^2}, & i = j, \end{cases}$$

which implies that $D_{ij}^2 \neq D_{ij}D_{ij}$ [62]. The matrix approximation to $\mathcal{L}$ on the finite grid is now denoted as

$$L_{ij} = -(F-1)D_{ij} + \sum_k \left(D_{ik}D^2{}_{kj} + \frac{3}{2}D_{ik}\delta_{kj}\eta_j \right).$$

The eigenvalues of L_{ij} are calculated using the standard function `eig()` from MATLAB [45].

5.3 Results

5.3.1 Evolution of perturbed steady solutions of the fKdV equation

Following Camassa & Wu [12] the wave-resistance coefficient C_r is introduced, which in physical terms provides a non-dimensional measure of the power being supplied or absorbed by the forcing. This can be useful in determining if there is oscillatory behaviour in the system (see [12]). The time-rate of change of the 'energy' of the fKdV equation is found by taking the product of (2.5.31) with η, and integrating over the spatial domain (and incorporating the condition that the functions η, η_x decay as $x \to \pm\infty$), to give;

$$\frac{\mathrm{d}}{\mathrm{d}t}\int_{-\infty}^{\infty} \eta^2 \,\mathrm{d}x = \int_{-\infty}^{\infty} p_x \eta \,\mathrm{d}x, \tag{5.3.8}$$

where the left-hand-side is time-rate of change of the energy of the system, and the right-hand-side is the definition of C_r.

The numerical simulation of the three steady solutions to the time-dependent fKdV equation which correspond to perturbations of solitary waves, types II–IV, demonstrates the instability of all three steady states; at least in the flow regime where the fKdV is a valid approximation. The system obtains either steady state of type I or V if $A \gtrless 0$, combined with some emission of waves which travel away

from the forcing. These results are summarised in figures 5.3.1–5.3.3 which we will now discuss, with reference to the known results for type II profiles shown in figure 5.3.1.

For positively forced waves, as observed by Camassa & Wu [12], Grimshaw & Maleewong [26], Shen *et al.* [56], the type-II waves are unstable to perturbations and will decay to a type-I solution near the region of forcing, with some emission of a finite number of waves. Figures 5.3.1(a) and (b) show the evolution of the free surface from the numerical simulation of the time-dependent fKdV with two different initial states. The initial states are the type-II solution with a normalised amplitude of 0.98 and 1.02. For the larger initial state a single solitary wave is emitted which advances upstream, combined with some radiation downstream in the form of a dispersive oscillatory wave. As seen by the positive value of C_r in figure 5.3.1(c), the fluid flow absorbs some energy from the forcing as it emits the upstream wave and decays to the stable solution in the forcing region. For the smaller initial state, no solitary wave is emitted upstream and energy is absorbed by the forcing as the solution smoothly decays to the type-I wave near the forcing, with the emission of a downstream solitary wave. The negative value of C_r observed in figure 5.3.1(d) indicates the system releases some energy to the forcing as the free-surface tends to the stable state.

For negatively forced solutions, the type-V solution is known to be stable [12, 44], and the profiles in figures 5.3.2 and 5.3.3 demonstrate that the type-III and type-IV waves are both unstable and emit waves both upstream and downstream as the free-surface attains a type-V-like profile near the forcing region. This is in contradiction to the suggestion by Malomed [44] that the cusped type-III wave may be stable. These results for the unsteady response to a small perturbation of this type of solution, which has a cusp, are new.

For the negatively forced solutions the emitted waves display complicated

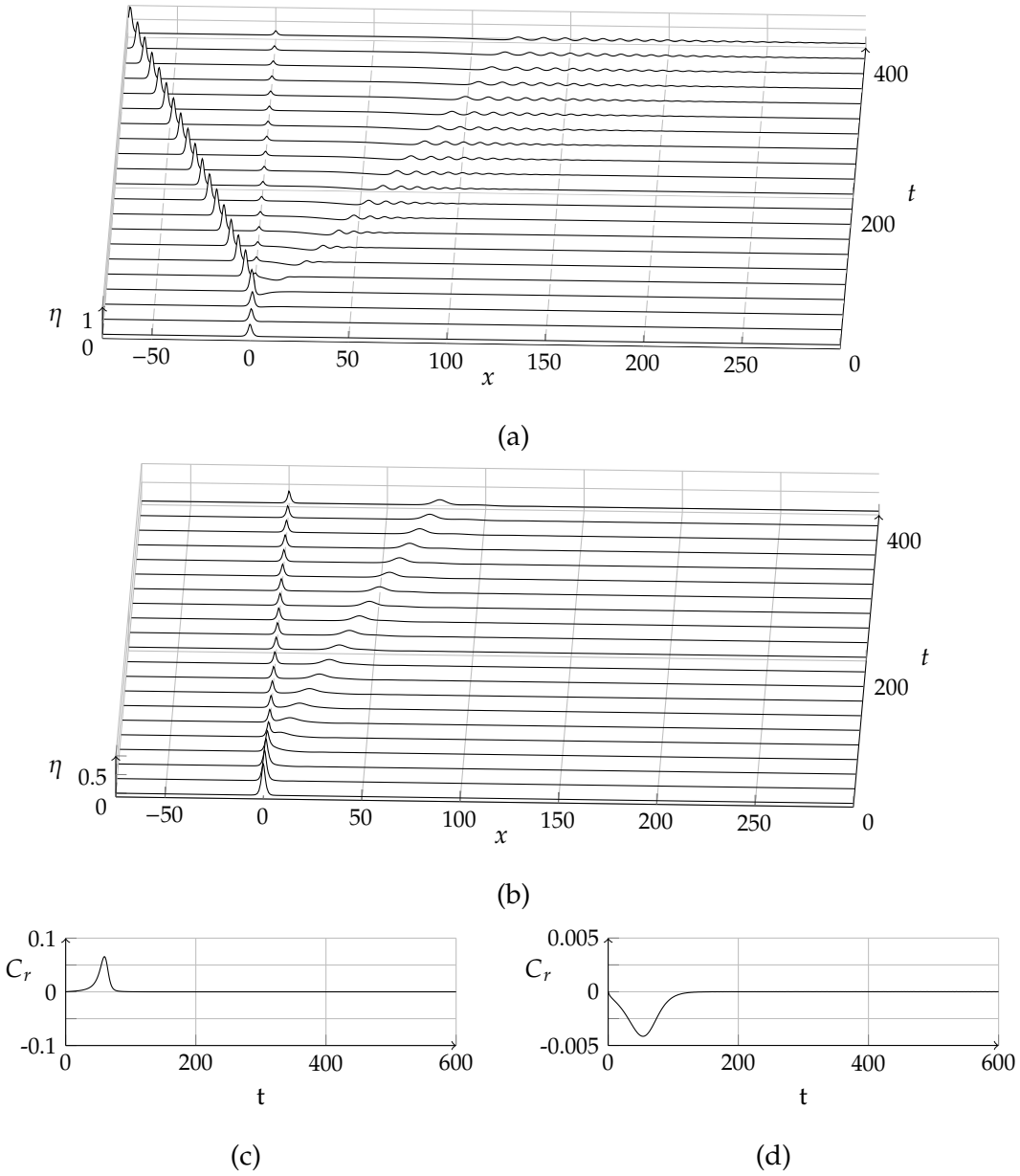

Figure 5.3.1: Perturbation to forced solitary wave of type II. Amplitude of forcing is $A = 0.13$, with domain width $W = 400$ and $N = 8192$ grid points, shown are (a) and (b) evolution of the free surface given initial states with normalised amplitude of 1.02 and 0.98 respectively; and (c) and (d) the wave-resistance coefficient as a function of time.

behaviour, and the choice of initial amplitude produced qualitatively different responses within solution types. The perturbed type-III waves emit a single solitary wave upstream, as well as nonlinear solitary-type waves and dispersive oscillatory waves downstream, this is shown in the evolution of the surface in figure 5.3.2(a) and (b). The cusp, although not visible on this scale, coalesces, before a single crested solitary wave is formed near the forcing. The larger initial state used in figure 5.3.2(a) shows some oscillation of the coalesced waveform about the forcing from time $T \approx 200$ before the final emission of the wave upstream at $T \approx 350$. As either the system or forcing absorbs energy, according to C_r shown in figure 5.3.2(c), the solitary-like wave near the forcing appears to be accelerated upstream or downstream respectively in figure 5.3.2(a). The wave-resistance C_r rapidly approaches zero from below as this solitary wave travels upstream, while the region near the forcing approaches the shape of the type-V solutions from thereon.

For the initial state with a smaller amplitude shown in figure 5.3.2(b) and (d) the solitary wave is emitted much sooner while travelling noticeably slower. There is only one oscillatory dispersive wave emitted in figure 5.3.2(b), as opposed to two that can be observed in figure 5.3.2(a) for the larger initial condition. In other respects, the behaviour for the smaller initial state is qualitatively very similar, with a somewhat diminished oscillation of the solitary mass near the forcing observed before the solitary wave is emitted upstream.

The final unstable solution, type IV, shown in figure 5.3.3(a)–(d), contains even more dramatic variation in the qualitative behaviour depending on the initial amplitude. For the smaller initial state shown in figure 5.3.3(b), the upstream and downstream humps are initially drawn towards the forcing, coalescing, and eventually emitted as a solitary wave upstream, similar to the type-III solution. The evolution of the larger initial state, shown in figure 5.3.3(a), shows the upstream

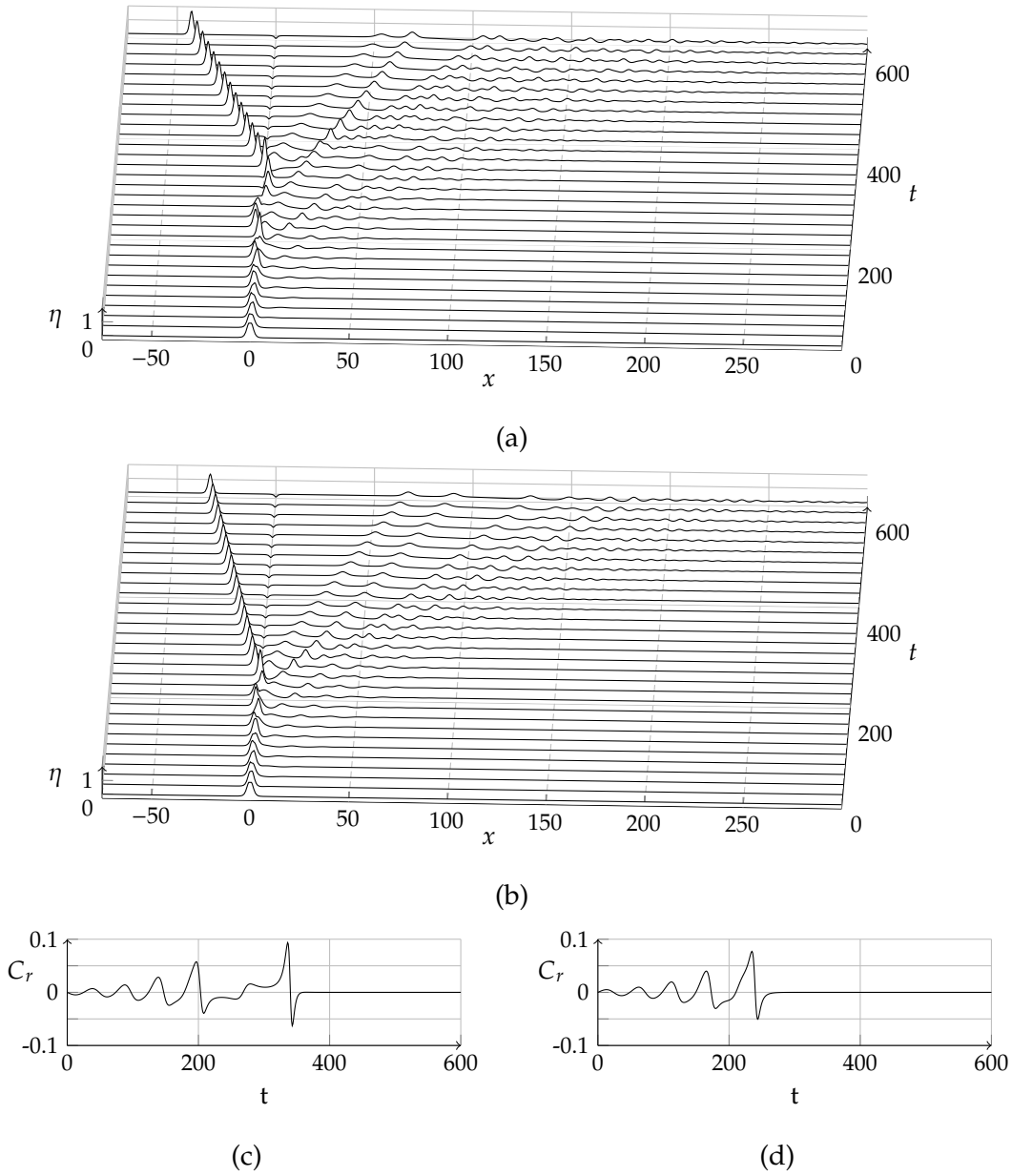

Figure 5.3.2: Perturbation to forced solitary wave of type III. Amplitude of forcing is $A = -0.13$, with domain width $W = 400$ and $N = 8192$ grid points, shown are (a) and (b) evolution of the free surface given initial states with normalised amplitude of 1.02 and 0.98 respectively; and (c) and (d) the wave-resistance coefficient as a function of time.

hump is very quickly emitted upstream. The same behaviour as observed for type-III solutions is seen with a remaining solitary-like wave near the forcing region from $T \approx 140$. This wave also accelerates upstream or downstream as the system or forcing absorbs energy respectively, and then finally heads upstream near $T \approx 300$. After this time, the type-V-like profile is observed near the forcing region from thereon.

All the solutions shown appear to tend to a steady stable state after the initial transients have decayed or been emitted, as supported by the rapid decay of the energy being absorbed by the system (or the forcing) shortly after the final solitary wave is generated. For any initial profile that resulted in the emission of an upstream supercritical solitary wave, the system absorbed energy in doing so, which can be confirmed by integrating the C_r curve over time.

5.3.2 Linearised stability analysis

The numerical results here agree with known result that the steady solutions given by perturbations to uniform streams, waves of type I and type V, are stable [12]. For these two types of wave, no eigenvalues with a real part larger in magnitude than 1.2×10^{-9} were found for the case of $F = 1.26$ and $A \in (0, 0.175)$. The eigenvalues which contained a real part less than 10^{-9} were found in pairs λ, λ^*, and so are assumed to be purely imaginary complex conjugate eigenvalues.

Meanwhile, the unstable solutions as identified in the previous section all demonstrate linear instability through the presence of eigenvalues which have significant non-zero real component. The eigenvalues for these solution types for fixed $F = 1.26$ are summarised in figure 5.3.4 over the range of A for which steady solutions exist. The results for the different wave types are presented in separate subfigures. For any eigenvalue with a significant real part, that is larger than 10^{-9}, the real component of the eigenvalue is plotted in figure 5.3.4(a), (b)

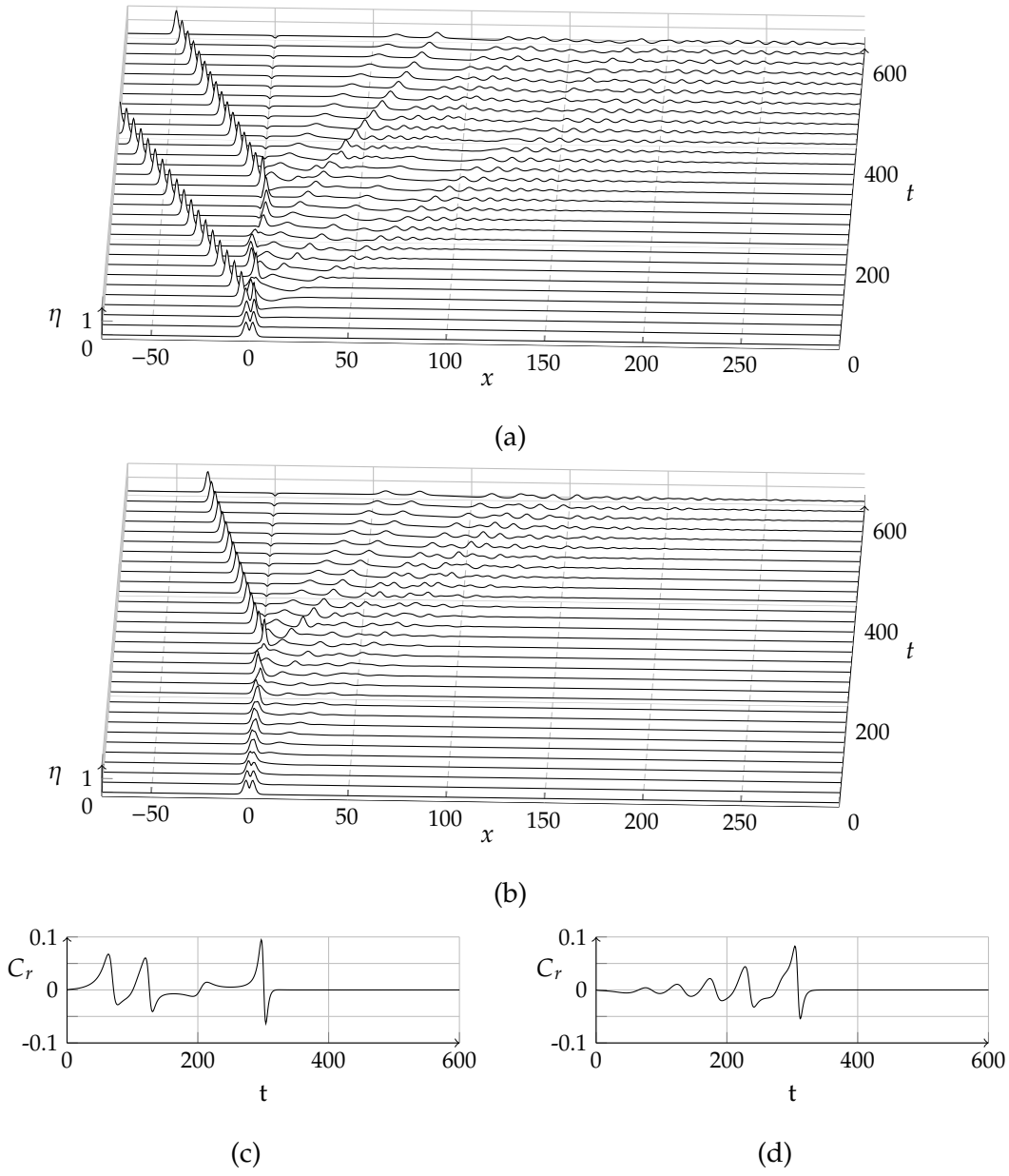

Figure 5.3.3: Perturbation to forced solitary wave of type IV. Amplitude of forcing given by $A = -0.13$, with domain width $W = 400$ and $N = 8192$ grid points, shown are (a) and (b) evolution of the free surface given initial states with normalised amplitude of 1.02 and 0.98 respectively; and (c) and (d) the wave-resistance coefficient as a function of time.

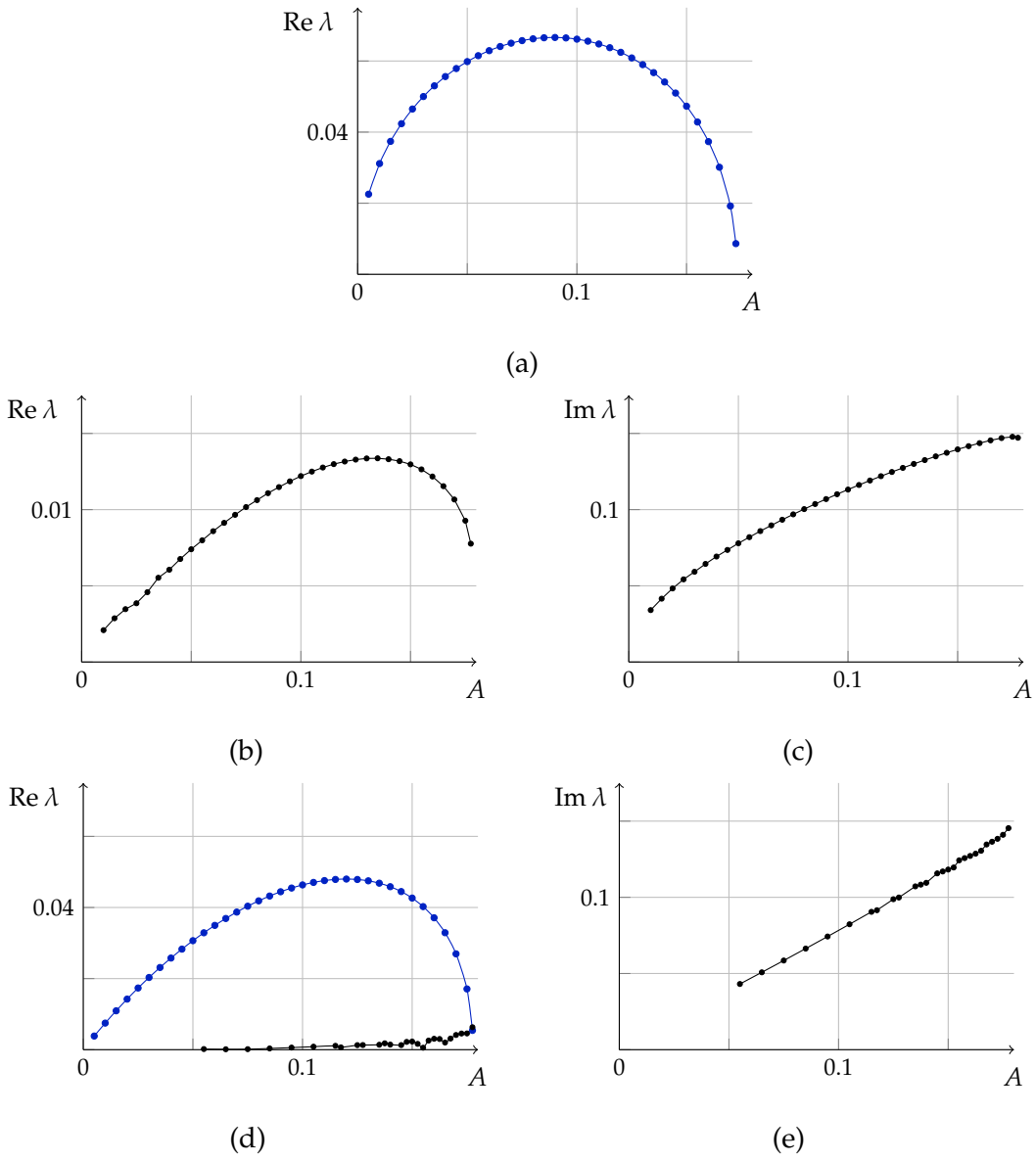

Figure 5.3.4: Markers indicate eigenvalues of (5.2.7) for $F = 1.26$ with significant positive real part found by MATLAB. Shown are (a) real part of eigenvalues for type-II waves, (b) and (c) real and imaginary parts for type-III waves and (d) and (e) real and imaginary parts for type-IV waves, with solid line fitted for illustrative purposes. Blue marker/line indicates a pure real eigenvalue, black marker/line indicates eigenvalue with a positive imaginary component. Eigenvalues with negative imaginary part not shown.

and (d) for type II, III and IV waves respectively, while the imaginary component of the eigenvalue is plotted in figure 5.3.4(c) and (e) for type III and IV waves respectively. Eigenvalues that appear as real pairs $\pm\lambda$ are shown in blue, whereas complex quartet eigenvalues $\pm\lambda, \pm\lambda^*$ are shown in black. Pairs and quartets of eigenvalues appear in the numerical results as expected from the symmetry of the operator $\mathcal{L}$ defined by equation (5.2.5). Any other eigenvalue calculated for $F = 1.26$ over this range of A appear to be purely complex conjugate pairs (or zero), with magnitude of their real part less than 1.2×10^{-9} as observed for all eigenvalues of the stable solutions.

The type-II wave has one linearly unstable eigenvalue with effectively zero imaginary component. Qualitatively similar results for other values of F near unity to the results shown for $F = 1.26$ in figure 5.3.4(a) were observed. For this type of wave the eigenvalue approaches zero on the approach to the unforced solitary wave solution, i.e. as $A \to 0$, which is known to be stable. It can also be seen that as we approach the stable uniform stream solution, that is as A approaches approximately 0.175, the eigenvalue approaches zero. Of all the types of wave, this type of wave has the largest rate of growth of linear instability.

The type-III wave has a complex quartet of eigenvalues, and like the type-II wave, the real part approaches zero as the stable unforced solitary wave is approached. In contrast, the real part does not approach zero as the type-IV wave is approached, for example as A approaches roughly 0.177 in figure 5.3.4(b) and (c) for the flow with $F = 1.26$. As the eigenvalues should depend continuously along the solution space for fixed F, this complex quartet of eigenvalues will be found within some region of the type IV solutions, too. This was observed in the numerical results as the complex quartet of eigenvalues for the type-III and type-IV waves approach the same value as A approaches approximately 0.177 in figure 5.3.4(d) and (e) for flow with $F = 1.26$. This was also observed for other

values of the Froude number.

The type-IV solution, in addition to possessing the complex quartet of eigenvalues, has a purely real pair of eigenvalues for all amplitudes of forcing. This real pair of eigenvalues approaches zero as either the type-III solution is approached, or as the limiting case of two solitary waves separated by a uniform stream is approached as $A \to 0$.

The behaviour of the eigenvalues for the complex quartets is difficult to determine for type-IV waves. With respect to the real part, there is an 'enveloping' effect, similar to that observed by Ee & Clarke [18] seen in figure 5.3.4(d), and to a lesser extent as $A \to 0$ for type III waves in figure 5.3.4(b). Additionally, the imaginary part does not appear to depend smoothly on A in figure 5.3.4(e) for type IV waves. These results are an artefact of the periodic domain assumption, which will be discussed in more detail after the general appearance of the eigenmodes and how well they perform as predictors of the evolution of the fKdV equation is determined.

The fastest growing mode can be used to determine the time scale of the validity of the linearised theory. Using these modes as an initial perturbation to the steady solution, the evolution of the perturbation given by $\eta(x,t) - \eta_s(x)$ from the full fKdV equation (2.5.31) can be compared to the expected growth from the linear theory (5.2.4).

Of all three unstable solution types, the type-II wave has the fastest growing linear instability, and so the agreement between the linearised theory breaks down at the earliest time. The eigenmode corresponding to a positive real-part eigenvalue when $F = 1.26$ and $A = 0.155$ is shown in figure 5.3.5(a). The evolution of the perturbation using the full fKdV equation is computed using the spectral method before, and compared to the growth predicted by the linear theory. The results from both computations for a type-II wave are shown in figure 5.3.5(b)

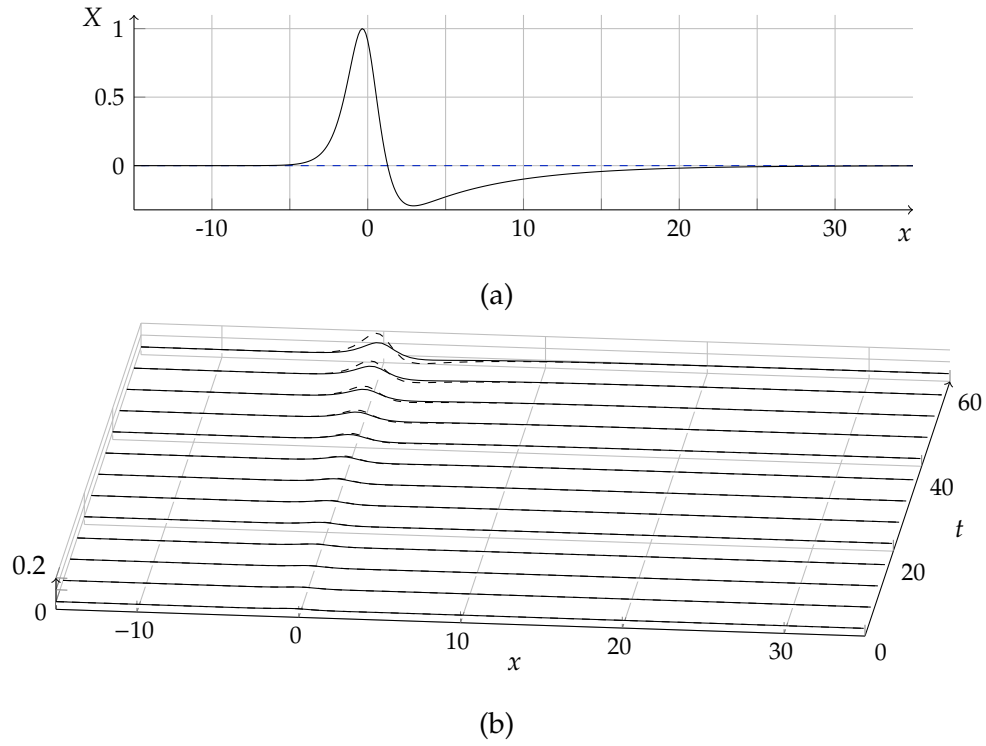

Figure 5.3.5: Linearised results for type-II solution with $F = 1.26$ and $A = 0.155$. Shown are (a) eigenmode corresponding to eigenvalue with significant positive real part, black line for the real part of eigenmode, blue dashed line for the imaginary part and (b) evolution of the eigenmode as a perturbation using the linear theory (solid line) and the full fKdV equation (dashed lines).

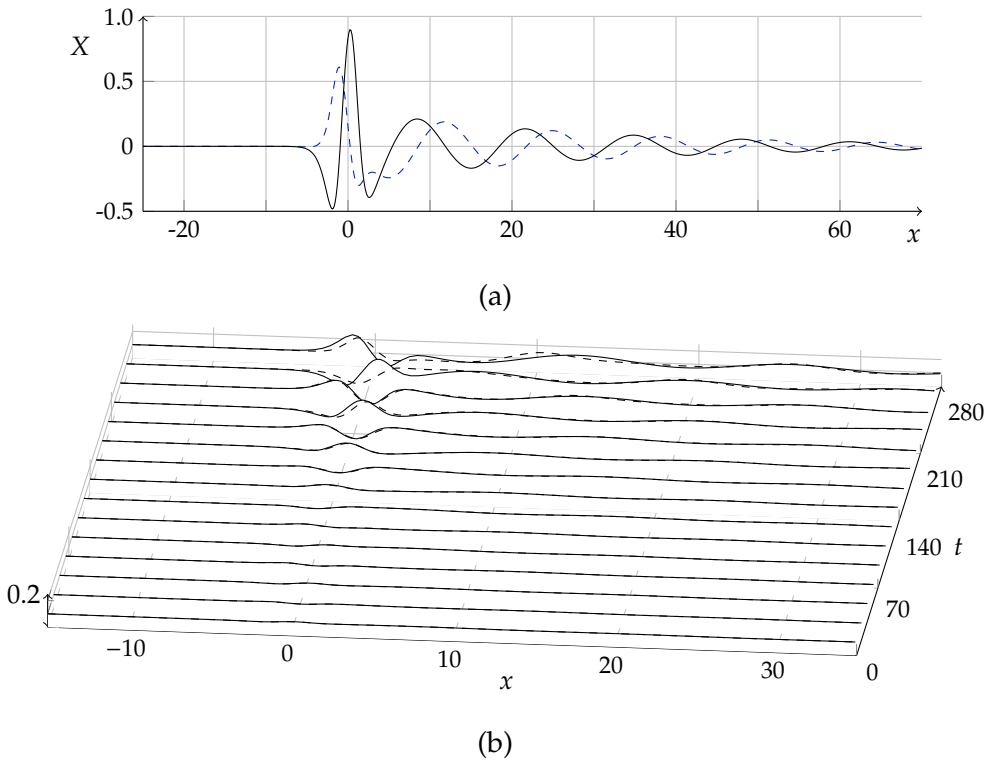

Figure 5.3.6: Linearised results for type-III solution with $F = 1.26$ and $A = -0.155$. Shown are (a) eigenmode corresponding to eigenvalue with significant positive real part, black line for the real part of eigenmode, blue dashed line for the imaginary part and (b) evolution of the eigenmode as a perturbation using the linear theory (solid line) and the full fKdV equation (dashed lines).

when the eigenmode is used as a perturbation with L_∞ norm being 0.02. Due to the larger rate of growth, the linearised prediction begins to depart from the full fKdV solution at the earliest time in comparison with the other types of wave. At $t = 60$ the agreement worsens, and a solitary wave is emitted upstream shorty after much like the behaviour observed in figure 5.3.1(a); the solitary wave emission is not predicted by the linearised perturbation theory.

As the type-III wave has a complex quartet of eigenmodes, and we desire a real perturbation, we take the sum of the eigenmodes from a complex conjugate

pair with positive growth rate as a perturbation. The eigenmode with positive real and imaginary part is shown in figure 5.3.6(a) for $F = 1.26$ and $A = 0.155$. The growth rate of these modes is generally much less than for wave-types II and IV, and so the linear theory accurately predicts the response of the free surface for a longer period of time. This is seen in figure 5.3.6(b) where the behaviour of the two theories, again for $F = 1.26$ and $A = 0.155$, is similar up until about $t = 200$. At around $t = 200$ the two peaks have coalesced in both theories (not shown here). After this time, the oscillation of a solitary mass near the forcing occurs in the full fKdV model, as observed in the results for the simpler initial perturbation shown in figure 5.3.2(a) and (b), which the linear theory is unable to predict.

The fastest growing mode for the type-IV wave for most values of A is from the real pair of eigenvalues. This eigenmode is shown in figure 5.3.7(b), while the eigenmode corresponding to the eigenvalue with positive real and imaginary part from the complex quartet is shown in figure 5.3.7(b). The fastest mode is used as a perturbation for the type-IV waves, with the same value of F and A as before, and the evolution of the perturbation is shown in figure 5.3.7(c). The linear theory departs from the predictions of the full fKdV equation on a similar time-scale to the type-II solution, as the growth rate is relatively similar. The coalescence of the two waves is correctly predicted by the linear theory, but beyond $t = 80$ the size of the perturbation is such that the linear theory is no longer valid, the emission of a solitary wave upstream in the full fKdV model follows shortly after.

The presence of a decaying spatial oscillation and how it is affected by the periodic domain is an important feature of the eigenmodes corresponding to a complex-quartet eigenvalue. The decaying oscillation is shown in figure 5.3.6(a) and figure 5.3.7(a) for the wave-types III and IV respectively. When this spatial oscillation decays rapidly, as in the type-III waves, the computed eigenvalues are consistent over a wide range of domain sizes. For the type-IV waves, the rate of

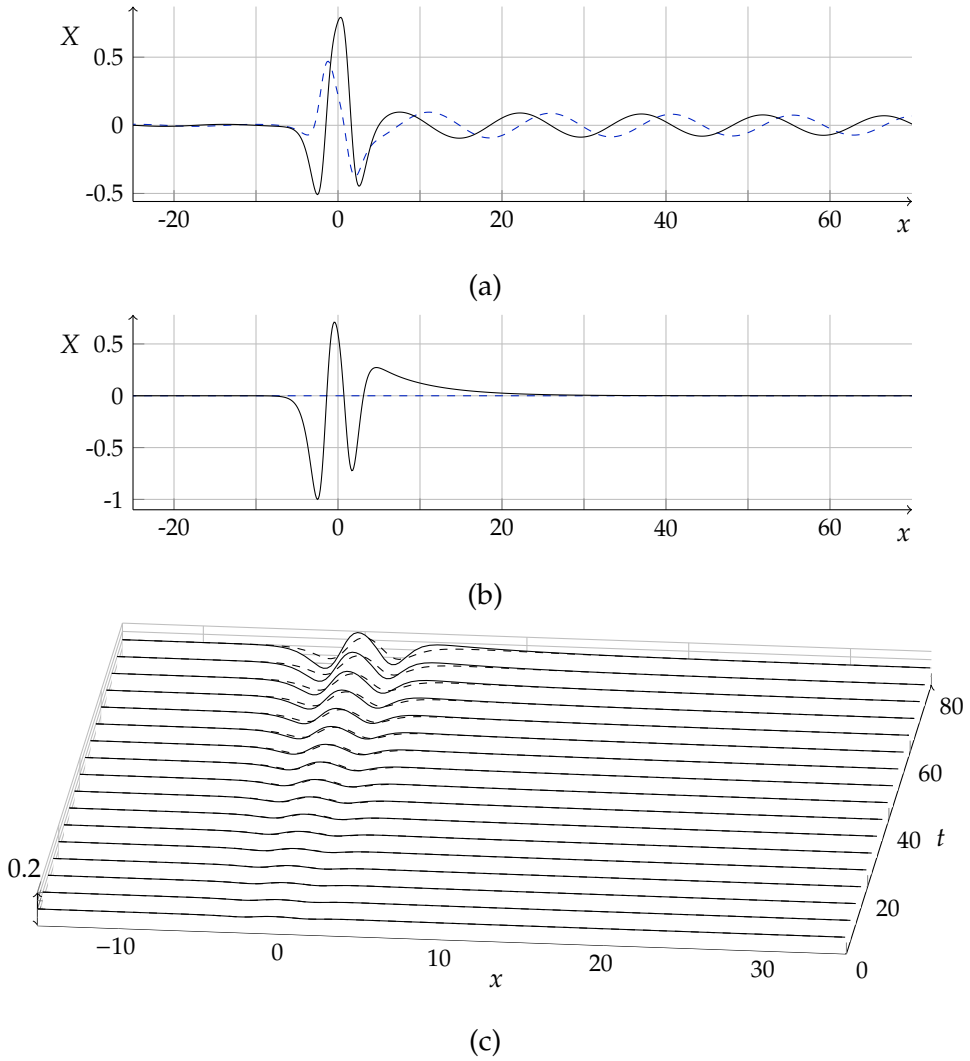

Figure 5.3.7: Linearised results for the type-IV solution with $F = 1.26$ and $A = -0.155$. Shown are (a) and (b) eigenmodes corresponding to eigenvalue with significant positive real part from the complex quartet and real pair respectively, black line for the real part of eigenmode, blue dashed line for the imaginary part; and (c) evolution of the eigenmode in (b) as a perturbation using the linear theory (solid line) and the full fKdV equation (dashed lines).

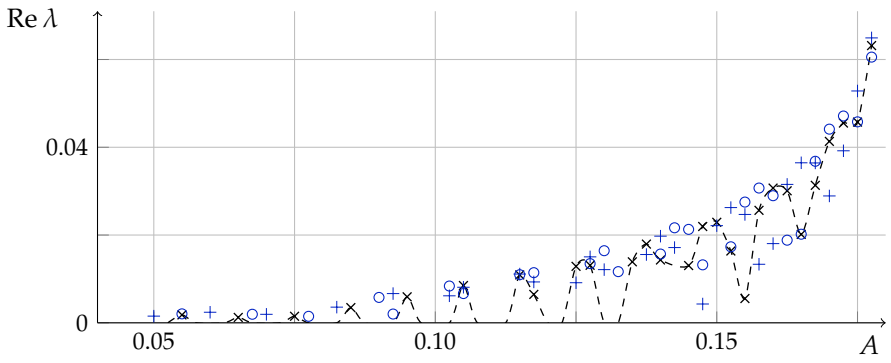

Figure 5.3.8: Real part (positive value only) of the complex quartet eigenvalues for type-IV solutions with $F = 1.26$. The $\circ$, $+$ and $\times$ markers indicate $W = 99.96, 110.04$ and 120 respectively, with fixed spatial sampling W/N. Dashed line follows the $W = 120$ eigenvalues, returning to the A axis where no complex quartet found.

spatial decay is generally smaller, and so the oscillation will reach the edge of the periodic domain and then wrap-around and appear at the other end.

The results for the eigenvalues using this numerical method is sensitive to the width of the domain. The lack of convergence over different domain sizes with fixed spatial sampling rate Δx for type-IV waves is shown in figure 5.3.8. For a fixed domain width, the real part of the eigenvalues intermittently tend to zero as A decreases. Each time this occurs a complex quartet of eigenvalues returns to the imaginary axis (cf. the dashed line in figure 5.3.8 returning to the A axis), and then another pair of pure-imaginary complex conjugate eigenvalues with a smaller wavenumber depart from the imaginary axis to form the new complex quartet as A continues to decrease. This behaviour gives the appearance of jumps in the imaginary part of the eigenvalues as A varies, as shown for the type-IV waves in figure 5.3.4(e).

Changes in domain size were the main driver of the changes in the eigenvalues, and so it can be concluded that the decaying spatial oscillation's incompatibility with a periodic boundary condition is responsible for the envelope effect on the

eigenvalues. Although the linear theory still indicates instability, the rate of growth of the perturbation cannot be accurately ascertained by the numerical approach used here. While it is possible that these may be spurious eigenvalues, we note that such eigenvalues are found for the case of type-III waves with a small forcing in Camassa & Wu [12].

5.4 Conclusion

The negatively forced perturbations to solitary waves, of either type III or type IV, are unstable. The type-III solution generates a solitary wave upstream after coalescing and oscillating about the forcing position for some initial interval of time, shown in figure 5.3.2(a) and (b). The downstream flow contains a mixture of solitary-like waves and dispersive wave trains. The type-IV solution behaves similarly but for the generation of two upstream waves when the initial state has enough mass, as shown in figure 5.3.3(a).

The linearised stability analysis agrees with previous investigations; the type-I and type-V solutions have no eigenvalues with non-zero real part, and are thus linearly stable. The significant eigenvalues for type-II waves appear as real-valued pairs, while type-III waves have a complex quartet, and type-IV waves have both a real valued pair and a complex quartet of eigenvalues. For the linear operators with complex-quartet eigenvalues, the numerical approach for calculating eigenvalues and eigenmodes breaks down as the rate of decay of the spatially oscillating mode associated with the complex quartet, seen in figure 5.3.6(a) and figure 5.3.7(a), decreases. This is a result of the assumption of a periodic domain in the linearised analysis, and so the downstream wave train of the eigenmode does not decay sufficiently fast to not interfere with the upstream portion of the eigenmode. This limits the significance of the results for the complex

quartet of eigenvalues obtained, in particular for the type-IV waves.

One potential remedy for the complex-quartet eigenvalue calculation is to relax the periodicity assumption and try a spectral collocation method with a different set of basis functions (such as Hermite exponential functions or Laguerre basis functions) [52]. This could then be extended further to a linearised stability analysis of the fully nonlinear problem, similar to that undertaken by Tanaka [60].

As a final comment, these results are more applicable to the pressure disturbance problem than for the flow past a topographical disturbance, as the latter departs from the weakly nonlinear analysis very rapidly as F or A get larger. The linearised stability analysis of the fully nonlinear problem could provide a much more accurate picture of the stability of the solutions to flow past a topographical disturbance. This future work is discussed in the next chapter.

Chapter 6

Conclusions

6.1 Summary of findings

In Chapter 2 a boundary-integral method for solving the fully nonlinear model of the flow past a disturbance in the channel was derived. A numerical method for finding the fully nonlinear solutions using an irregular discretisation was presented, with an analysis of the error given in Appendix B which extends a result of Noble & Beighton [48]. The forced Korteweg de-Vries equation with a jump condition was presented as a weakly nonlinear model, which is used in the classification of the fully nonlinear solutions.

The solutions to flow past a pressure disturbance were then considered in Chapter 3. Efficient expressions to approximate the contributions of the far-upstream and far-downstream flow were employed in the boundary integrals, based on the linearised solution in the far-field presented in Appendix D. The solution space was then presented by considering one-parameter families of solution with a fixed value of F, shown in figure 3.3.5. All the types of flow identified by the weakly nonlinear model were identified, which we enumerate as type I–V. Waves types I and V waves are perturbations to uniform streams, being waves of elevation and

depression respectively. Wave types II and type III are perturbations to a single solitary wave, where the type-II wave has a single crest and the type-III wave has a cusp-like appearance with two peaks. Type-IV waves are perturbation to two solitary waves, with two distinct crests.

The fully nonlinear solutions which were perturbations to solitary waves, that is type-II, III and IV, were found to approach a Stokes limiting configuration as the wave-height increased, as shown in figure 3.3.7–3.3.10. New results showing that quantities such as the speed and total energy of these wave, shown in figures 3.3.7-3.3.10(c) and (d), are not unique with respect to wave-height in the almost-highest regime.

An previously unobserved effect due to the presence of the nearby pressure disturbance was found for the almost-highest type-III wave. The peaks of the wave had a 120° included angle, but were not symmetric about a vertical axis, as evidenced by in figure 3.3.7(b), a slight clockwise/anti-clockwise rotation of the configuration was observed down/upstream. This was explained by a modified analysis of the Stokes limiting configuration using an approximation of the pressure disturbance when the cusp is small.

The solution space of the topographical disturbances was explored in Chapter 4, as summarised in figure 4.3.5. The solution space differed from that of the pressure disturbance solutions, particularly for large disturbances. The free-surface is no longer strongly influenced by changes in the size of the trench as the trench gets very deep. This was seen in figure 4.3.6, and would cause the continuation method to fail to converge for $\hat{A} < -1.1$, due to the practical limit on the size of the grid. We obtained almost-highest solutions for type II waves for flow past a bump or a trench, see figures 4.3.7 and 4.3.8, and type IV waves for flow past a trench, see figure 4.3.9. For the trenches that could be computed, no almost-highest solution corresponding to a type III wave, those with a cusp, and a Stokes limiting

configuration at each peak was found.

The non-uniqueness with respect to quantities such as the speed and mass of the flow as the wave-height increases was also observed for the first time, see figures 4.3.7-4.3.9(c) and (d). For the type-IV waves, for flow with either of the pressure or topographical disturbances considered, the location of the turning points and the form of the two crests were observed to be almost exactly that of the unforced solutions. This indicates that these properties are more local to the crest and not influenced by the forcing which is far from the crest.

The stability of the five different solution types was then reviewed in Chapter 5 using the time-dependent fKdV equation. Weakly nonlinear solutions for the steady fKdV with a Gaussian forcing function were found numerically using `chebfun` [63]. The evolution of the free surface given a perturbed steady solution was used to examine stability. The perturbations to uniform streams were found to be stable, as determined previously [12, 27], while the perturbations to solitary waves were unstable.

The type-II waves for flow past a positive amplitude forcing behaved as expected, see figure 5.3.1, with the emission of an upstream solitary wave and a downstream dispersive oscillatory wave when the initial state had enough mass, or, for an initial state with less mass a single solitary mass propagates downstream. The region near the forcing returns to the stable perturbation to a uniform stream.

The type-III waves past a negative amplitude of forcing displayed a more complex unsteady response, see figure 5.3.2. This included the coalescence of the cusp, followed by emission of a solitary wave upstream and a combination of solitary masses and dispersive oscillatory waves downstream. The region near the forcing eventually attains the form of the perturbation to a uniform stream. The unsteady response for the type-IV waves is similar, except for the case where the initial state is such that two solitary waves are emitted upstream, see figure 5.3.3,

one of which is emitted almost immediately along with a dispersive wave-train downstream.

A linearised analysis of the fKdV equation was also performed, confirming the instability of the perturbations to solitary waves via the presence of eigenmodes with significant positive real part. The linearised analysis was performed by applying a finite spectral approximation to the linear operator (5.2.5). The linear analysis showed the type-II solution has a real pair of eigenvalues, and is thus unstable. The type-III waves past a negative forcing had a complex quartet of eigenvalues, while the type-IV waves had both a real pair and a complex quartet of eigenvalues. This is the first time the instability of these latter two solution types has been demonstrated. The complex quartet of eigenvalues had smaller real part than the real pair, and so the linear analysis remained valid for a longer time than for the other solution types, see figures 5.3.5b–5.3.7c. The emission of the solitary wave upstream was generally an indicator of when the linearised theory would break down, as expected by such a nonlinear phenomenon.

The eigenmodes from a complex quartet of eigenvalues possess a spatially decaying oscillation, see figure 5.3.6(a) and figure 5.3.7(a), which combined with the assumption of periodicity, prevented the determination of the exact behaviour of the eigenvalues and eigenmodes, particularly for type-IV waves, or for type-III waves with a small forcing.

6.2 Future work

One of the aims of this research was to determine the entire solution space for the potential flow past a trench. As this was not fully determined, we suggest two further investigations into potential flow past a trench. The first is to investigate large trenches using the same numerical method here but with a larger grid.

Recently Pethiyagoda *et al.* [49] and Pethiyagoda *et al.* [50] utilised GPU hardware to implement Jacobian-free Krylov subspace methods to find solutions to the two-dimensional free surface of a model of the flow past a ship, using typically 721×241 grid points for a two-dimensional surface. Applying a similar approach here could provide enough grid points to explore the remainder of the solution space. The other avenue to explore is the solution space of a different weakly nonlinear model, the generalised-Boussinesq equation, which was derived for this same flow in Wu [70]. This could offer insight to the reasons for the difference between the fKdV and the fully nonlinear solution space.

The solution space of combined disturbances (e.g. pressure and topography) in the almost-highest wave regime is another area of potential investigation. Although combinations of topographical and pressure disturbances have been previously studied by others [7, 9, 17], their behaviour when almost highest waves are present is not yet understood. We hypothesise that trapped almost-highest waves might be observed between two disturbances, and that they are likely to be unstable, similar to the unforced and forced waves studied here, and the waves studied by Chardard *et al.* [14].

For the flows past a trench, it is clear that a boundary layer would form where viscous effects need to be modelled to understand realistic fluid flow. Still, the effect of viscosity is an open question in the almost-highest regime for either forced and unforced waves. The almost-highest solutions may be strongly affected by a dissipative force such as viscosity, as well as surface tension. Underlying currents or a stratified flow is another flow configuration for which the highest waves could be considered.

The evolution of perturbed steady solutions in Chapter 5 was based entirely on the weakly nonlinear fKdV model. Grimshaw & Maleewong [26] employed a method for computing the evolution of the fully nonlinear free surface for forced

waves. This approach could be used to examine the evolution of the steady states that we obtained in Chapter 3 and 4, particularly for the wave types III and IV which have not been considered previously.

In the unforced case, the non-uniqueness of the almost-highest waves has implications for the stability, as the local maxima of the energy as a function of wave-height is connected to the onset of a short wavelength instability [32, 60]. It may not be the case that the perturbations to uniform streams which are close to limiting configurations are stable, for example when A is large in figure 3.3.5(d). If these are unstable, the next question would be whether this is due to the presence of a turning point in some integral quantity such as the energy.

As a first step towards investigating this, the stability could be considered numerically using a linearised stability analysis based on the approach of Tanaka [60], which we briefly formulate here. Once a steady solution is obtained, that is, τ_s and θ_s are known for a steady flow, then the kinematic and dynamic boundary conditions given by (A.4) and Bernoulli's equation (A.9) can be linearised about the steady state to form an eigenvalue problem for the stability.

Let the steady states η_s and ϕ_s satisfy;

$$\begin{gathered}\frac{1}{2}(\phi_{sx}^2+\phi_{sy}^2)+\frac{1}{F^2}(1+\eta_s+p)=\frac{1}{2}+\frac{1}{F^2}\quad\text{and}\\ \eta_{sx}\phi_{sx}=\phi_{sy},\end{gathered}\tag{6.2.1}$$

and assume $\eta(x,t)=\eta_s(x)+\hat{\eta}(x,t)$ and $\phi(x,y,t)=\phi_s(x,y)+\hat{\phi}(x,y,t)$, where $\hat{\eta}$ and $\hat{\phi}$ are small perturbations. Assuming that the small perturbations are of the form $\hat{\eta}=e^{\lambda t}\widetilde{\eta}(x)$ and $\hat{\phi}=e^{\lambda t}\widetilde{\phi}(x)$ yields;

$$\begin{aligned}\lambda\widetilde{\phi}&=-e^{\tau_s}\frac{\mathrm{d}\widetilde{\phi}}{\mathrm{d}l}-\left(e^{\tau_s}\frac{\mathrm{d}}{\mathrm{d}l}(e^{\tau_s}\sin\theta_s)+\frac{1}{F^2}\right)\widetilde{\eta}\quad\text{and}\\ \lambda\widetilde{\eta}&=-e^{\tau_s}\frac{\mathrm{d}\widetilde{\eta}}{\mathrm{d}l}-\sec\theta_s\frac{\mathrm{d}\widetilde{\psi}}{\mathrm{d}l}-\widetilde{\eta}\sec\theta_s\frac{\mathrm{d}}{\mathrm{d}l}(e^{\tau_s}\cos\theta_s)\end{aligned}\tag{6.2.2}$$

by introducing a perturbation stream function $\widetilde{\psi}(x,y,t)$ such that $\widetilde{\phi}_y=-\widetilde{\psi}_x$, and l is the arclength along the free surface.

The preceding equation is the same as equation (7) in Tanaka [60] expressed in terms of the variables τ_s and θ_s. Given a symmetric steady state, it will follow that the eigenvalues appear in pairs/quartets as before, depending on whether they have non-zero real and imaginary part, much like the linearised analysis of the fKdV equation presented in Chapter 5.

Using the Schwarz reflection principle on the function $\widetilde{f} = \widetilde{\phi} + i\widetilde{\psi}$ and assuming that it vanishes at infinity, the contour integral enclosing the flow and its reflection of the function $\widetilde{f}(f)/(f - \phi + i)$ results in the following expression;

$$\widetilde{\psi}(\phi) + \frac{2}{\pi}\int_{-\infty}^{\infty} \frac{\widetilde{\psi}(\hat{\phi})}{(\hat{\phi}-\phi)^2+4}\,\mathrm{d}\hat{\phi} = \frac{1}{\pi}\fint_{-\infty}^{\infty} \frac{\widetilde{\phi}(\hat{\phi})}{\hat{\phi}-\phi}\,\mathrm{d}\hat{\phi} - \frac{1}{\pi}\int_{-\infty}^{\infty} \frac{(\hat{\phi}-\phi)\widetilde{\phi}(\hat{\phi})}{(\hat{\phi}-\phi)^2+4}\,\mathrm{d}\hat{\phi}.$$

From this expression, an operator G can be constructed which solves $\widetilde{\psi} = G(\widetilde{\phi})$. This allows for the approximation of the operator on the right-hand-side of the eigenvalue problem given by (6.2.2) as a matrix. The spatial derivatives can be approximated either using a spectral approach where the domain is assumed periodic, or a finite difference scheme as per Tanaka [60]. The eigenvalues could then, in theory, be found numerically. It may be the case that, as in Chapter 5, the periodic assumption could cause inaccuracies for operators with eigenmodes with slow decay, and so alternative basis functions for the approximation of the operator, such as Hermite exponential functions Shen *et al.* [52], may be useful.

6.3 Final remarks

Very steep waves in free-surface potential flows past two types of disturbance have been considered. The non-uniqueness of very steep waves for flow past a localised forcing has been established clearly, for the first time, by computing the free-surface profiles using a boundary-integral method. The forced solutions which are considered perturbations to one or two solitary waves have been shown

to be unstable in the domain of validity of a weakly nonlinear model given by the fKdV equation. This is the first observation of the instability of the cusped and double-crested solutions.

Appendix A

Equations of fluid motion

A.1 Governing Equations

Euler's equations of motion are a statement of the balance of momentum and force in a continuous medium. The equations are derived here using Reynolds' transport theorem and the divergence (Ostrogradsky-Gauss) theorem.

For the purpose of the derivation, consider a three-dimensional domain, rather than two-dimensional, with Eulerian coordinates $\mathbf{x}^* = (x^*, y^*, z^*)$. Let the velocity and pressure be functions of the spatial variable $\mathbf{x}^*$ and time t^* (as a dimensional quantity). Denote each component of a vector quantity $\mathbf{f} = (f_1, f_2, f_3)$, where the components are scalar functions of the spatial variables and the time variable, i.e. $f_i = f_i(x^*, y^*, z^*, t^*)$ for $i = 1, 2, 3$, the divergence is

$$\nabla_{\mathbf{x}^*} \mathbf{f} = \frac{\partial f_1}{\partial x^*} + \frac{\partial f_2}{\partial y^*} + \frac{\partial f_3}{\partial z^*},$$

and for a scalar quantity $f = f(\mathbf{x}^*, t^*)$;

$$\nabla_{\mathbf{x}^*} f = \left(\frac{\partial f}{\partial x^*}, \frac{\partial f}{\partial y^*}, \frac{\partial f}{\partial z^*} \right).$$

Definition 1. *The material derivative operator is*

$$\frac{D}{Dt^*} = \frac{\partial}{\partial t^*} + \mathbf{u}^* \cdot \nabla_{\mathbf{x}^*}$$

Theorem 1 (Reynolds' transport theorem)**.** *Given a flow with Eulerian coordinate* $\mathbf{x}^*$ *and a flow* $\mathbf{r}^*$ *(e.g. position of a fluid particle) with* $\partial \mathbf{r}^*/\partial t^* = \mathbf{u}^*$*, and some quantity* f *in the flow domain, differentiation (w.r.t. material derivative) outside an integral over any moving 'control' volume* V_{t^*} *in the flow can be brought inside the integral by the following equality,*

$$\frac{D}{Dt^*}\int_{V_{t^*}} f \,\mathrm{d}V = \int_{V_{t^*}} \frac{Df}{Dt^*} + f\nabla_{\mathbf{x}^*}\mathbf{u}^* \,\mathrm{d}V,$$

where $\mathrm{d}V$ *indicates the usual volume integral.*

Theorem 2 (Divergence theorem)**.** *For a vector quantity* $\mathbf{f}$*,*

$$\int_{S_{t^*}} \mathbf{f}\cdot\mathbf{n}\,\mathrm{d}A = \int_{V_{t^*}} \nabla_{\mathbf{x}^*}\mathbf{f}\,\mathrm{d}V,$$

where $\mathrm{d}A$ *is usual oriented surface area integral, with* S_{t^*} *being the surface of the volume* V_{t^*} *at time* t^**.*

Corollary 1 (Divergence theorem)**.** *Consider* $f = f(\mathbf{x}^*)$*. The divergence theorem applied to* $\sum_i \mathbf{e}_i \int_{S_{t^*}} (f\mathbf{e}_i)\cdot\mathbf{n}\,\mathrm{d}A$*, for the usual Cartesian coordinate basis* $\mathbf{e}_i$*, gives the following;*

$$\int_{S_{t^*}} f\mathbf{n}\,\mathrm{d}A = \int_{V_{t^*}} \nabla_{\mathbf{x}^*} f\,\mathrm{d}V.$$

Momentum is given by

$$\int_{V_{t^*}} \rho\mathbf{u}^*\,\mathrm{d}V.$$

Let $\mathbf{u}^* = (u_1^*, u_2^*, u_3^*)$, and let the force in the system be $\mathbf{F} = (F_1, F_2, F_3)$. Using Reynolds' transport theorem and Newton's second law of motion, for $i = 1, 2, 3$,

$$\frac{D}{Dt^*}\int_{V_{t^*}} \rho u_i^*\,\mathrm{d}V = \int_{V_{t^*}} \frac{D}{Dt^*}(\rho u_i^*) + \rho u_i^*\nabla_{\mathbf{x}^*}\mathbf{u}^*\,\mathrm{d}V = F_i.$$

Pressure and gravity are the only forces considered, so we can use the corollary of the divergence theorem 1 to find an expression for the force due to pressure $\mathbf{F}_p$,

$$\int_{S_{t^*}} -p^*\mathbf{n}\,\mathrm{d}A = \int_{V_{t^*}} -\nabla_{\mathbf{x}}p^*\,\mathrm{d}V = \mathbf{F}_p.$$

Then including gravity,

$$\int_{V_{t^*}} \frac{D}{Dt^*}(\rho u_i^*) + \rho u_i^* \nabla_{\mathbf{x}^*} \mathbf{u}^* \, \mathrm{d}V = \int_{V_{t^*}} -(\nabla_{\mathbf{x}^*} p^*)_i \, \mathrm{d}V,$$

$$\Rightarrow \quad \frac{\partial}{\partial t^*}(\rho u_i^*) + \nabla_{\mathbf{x}^*}(\rho u_i^* \mathbf{u}^*) = -(\nabla_{\mathbf{x}^*} p^*)_i + \begin{cases} 0 & \text{for } i = 1, 3 \\ -\rho g & \text{for } i = 2, \end{cases} \tag{A.1}$$

where the last equation follows using the monotone convergence theorem or similar argument.

A.1.1 Conservation of mass

$$\int_{V_{t^*}} \frac{D}{Dt^*}(\rho) + \rho \nabla_{\mathbf{x}^*} \mathbf{u}^* \, \mathrm{d}V = 0,$$

$$\Rightarrow \quad \frac{\partial \rho}{\partial t^*} + \nabla_{\mathbf{x}^*}(\rho \mathbf{u}^*) = 0.$$

If ρ is constant, i.e. the flow is incompressible, then this simplifies to

$$\nabla_{\mathbf{x}^*} \mathbf{u}^* = 0. \tag{A.2}$$

A.1.2 Irrotational flow

Irrotational flow is defined as flow for which the curl of the velocity field is zero;

$$\left(\frac{\partial}{\partial x^*}, \frac{\partial}{\partial y^*}, \frac{\partial}{\partial z^*} \right) \times \left(u_1^*, u_2^*, u_3^* \right) = \mathbf{0},$$

$$\Rightarrow \quad \frac{\partial u_3^*}{\partial y^*} - \frac{\partial u_2^*}{\partial z^*} = \frac{\partial u_3^*}{\partial x^*} - \frac{\partial u_1^*}{\partial z^*} = \frac{\partial u_2^*}{\partial x^*} - \frac{\partial u_1^*}{\partial y^*} = 0. \tag{A.3}$$

From here on, it is assumed that the flow is irrotational, and that the flow is invariant in the z^* direction, so all partial derivatives with respect to z^* vanish, and the velocity and pressure are now functions of x^*, y^* and t^*.

A.1.3 No-penetration kinematic boundary condition

The material derivative of a quantity f on either the bottom topography or the free surface must be zero. Applying this condition to the quantity $f = y^* - [H + \eta^*(x^*, t^*)]$ on the free surface, where it is assumed for the moment that the location of the free surface may vary over time, gives the kinematic condition

$$\eta_{t^*} + \mathbf{u}^* \cdot (-\eta^*_{x^*}, 1) = 0 \quad \text{for } y^* = H + \eta^*(x^*, t^*). \tag{A.4}$$

Similarly, applying the zero material derivative condition to $f = y^* - \sigma^*(x^*)$ on the channel floor gives another kinematic boundary condition,

$$\mathbf{u}^* \cdot (-\sigma^*_{x^*}, 1) = 0 \quad \text{for } y^* = \sigma^*(x^*). \tag{A.5}$$

A.2 The two-dimensional potential flow model

Now using the non-dimensional variables from §2.1.1, the conservation of mass (A.2) states that

$$\frac{\partial u}{\partial x} + \frac{\partial v}{\partial y} = 0. \tag{A.6}$$

Let the streamfunction $\psi(x, y, t)$ be given by

$$\int_0^x v(\hat{x}, y, t)\, \mathrm{d}\hat{x} = -\psi(x, y, t).$$

By the fundamental theorem of calculus $-\frac{\partial}{\partial x}\psi(x, y, t) = v(x, y, t)$. Then

$$\begin{aligned} \int_0^x \frac{\partial}{\partial \hat{x}} u(\hat{x}, y, t)\, \mathrm{d}\hat{x} &= -\int_0^x -\frac{\partial}{\partial y}\frac{\partial \psi}{\partial \hat{x}}\, \mathrm{d}\hat{x}, \\ \Rightarrow \quad u(x, y, t) - u(0, y, t) &= \frac{\partial}{\partial y}\left[\psi(\hat{x}, y) + F(y, t)\right]_0^x, \\ &= \frac{\partial}{\partial y}\psi(x, y, t) - \frac{\partial}{\partial y}\psi(0, y, t). \end{aligned}$$

Thus the function ψ satisfies

$$u = \frac{\partial \psi}{\partial y} \quad \text{and} \quad v = -\frac{\partial \psi}{\partial x},$$

and any u, v given by such a function ψ describes incompressible flow. It can also be observed that the streamfunction is everywhere orthogonal to the velocity, and thus a streamlines (for a fixed moment in time) are given by the streamfunction ψ being equal to a constant.

The irrotational flow condition (A.3) in non-dimensional form is

$$\frac{\partial v}{\partial x} - \frac{\partial u}{\partial y} = 0.$$

Let the velocity potential $\phi(x, y, t)$ be given by

$$\int_0^x u(\hat{x}, y, t)\, \mathrm{d}\hat{x} = \phi(x, y, t),$$

then via a similar argument the function ϕ satisfies

$$u = \frac{\partial \phi}{\partial x} \quad \text{and} \quad v = \frac{\partial \phi}{\partial y}.$$

Together, the velocity and streamfunction satisfy the following two equations,

$$\frac{\partial \phi}{\partial x} = \frac{\partial \psi}{\partial y} \quad \text{and} \quad \frac{\partial \phi}{\partial y} = -\frac{\partial \psi}{\partial x}.$$

These are the Cauchy-Riemann equations [5], and so the *complex potential* function

$$f_t(z) = f_t(x + \mathrm{i}y) = \phi(x, y, t) + \mathrm{i}\psi(x, y, t) \tag{A.7}$$

is analytic for $f_t : \mathbb{C} \to \mathbb{C}$ for all $t \in \mathbb{R}$.

A.3 The dynamic boundary condition

Now assuming the irrotational flow of an incompressible fluid, the equations for the conservation of momentum (A.1) in non-dimensional variables are;

$$u_t + uu_x + vv_x + \frac{1}{F^2} p_x = 0, \text{ and}$$
$$v_t + uu_y + vv_y + \frac{1}{F^2} p_y + \frac{1}{F^2} = 0.$$

By integrating the two equations in x and y, the Bernoulli principle for this flow is

$$\frac{\partial \phi}{\partial t} + \frac{1}{2}(u^2 + v^2) + \frac{1}{F^2}(y + p) = \left[\frac{\partial \phi}{\partial t} + \frac{1}{2}(u^2 + v^2) + \frac{p}{F^2}\right]_{(0,0,t)}$$

throughout the flow domain.

Take the pressure on the free surface to be 0 far downstream, and as $x \to \infty$, the uniform stream is given by

$$(u, v) \to (1, 0) \quad \text{and} \quad \eta \to 0. \tag{A.8}$$

Using this condition in Bernoulli's equation it follows that throughout the flow

$$\frac{\partial \phi}{\partial t} + \frac{1}{2}(u^2 + v^2) + \frac{1}{F^2}(y + p) = \lim_{X \to \infty} \left.\frac{\partial \phi}{\partial t}\right|_{(X,1,t)} + \frac{1}{2} + \frac{1}{F^2}. \tag{A.9}$$

This equation is used as a dynamic boundary condition in order to close the problem of solving for the unknown free surface.

Appendix B

Trapezoidal rule error with removal of singularity

B.1 Error term for a class of Cauchy P.V. integrals

Noble & Beighton [48] prove the error in using the trapezoidal rule for a class of principal value integrals is second order in the width of the subintervals and is bounded. This proof is reproduced here, and then the extension to the case where a transform of variables is used, as in equation (2.2.22) or (2.2.24), is presented.

Consider the numerical evaluation of the following integral for some x with $a < x < b$,

$$\fint_a^b \frac{f(y)}{y-x}\,\mathrm{d}y.$$

To 'remove' the singularity, we first note that

$$\fint_a^b \frac{f(y)}{y-x}\,\mathrm{d}y = \int_a^b \frac{f(y)-f(x)}{y-x}\,\mathrm{d}y + f(x)\ln\left|\frac{b-x}{x-a}\right|. \tag{B.1}$$

Define

$$F(y;x) = \frac{f(y)-f(x)}{y-x},$$

then the trapezoidal rule, using n subintervals, applied to the principal-value integral above is

$$\fint_a^b \frac{f(y)}{y-x}\,\mathrm{d}y = f(x)\ln\left|\frac{b-x}{x-a}\right| + h\left[\frac{1}{2}F_0 + F_1 + \ldots + F_{n-1} + \frac{1}{2}F_n\right] + E, \tag{B.2}$$

where h is the subinterval width, $nh = b-a$, $y_i = a + ih$, and $F_i = F(y_i; x)$. To avoid issues with the limit as $x \to y_i$, we assume that $y_i \neq x$. From Krylov [34], the error term $E(x)$ is given by

$$E(x) = \sum_{n=1}^{\infty} \frac{B_{2n}}{(2n)!} h^{2n} \left[\frac{\partial^{2n-1}}{\partial y^{2n-1}} F(y;x)\right]_{y=b}^{y=a}, \tag{B.3}$$

where the B_{2n} are the Bernoulli numbers which are explicitly given by

$$B_{2n} = \sum_{k=0}^{2n} \sum_{j=0}^{k} (-1)^j \binom{k}{j} \frac{j^{2n}}{k+1}$$

for $n \geq 1$.

The following theorem by Noble & Beighton [48] shows that, even though there are singularities in $F(y;x)$, the error term E is bounded for all $x \in (a,b)$ and is second order in the grid spacing h.

Theorem 3. *If $f(y) \in C^\infty(a,b)$, then the error term (B.3) for the trapezoidal rule as applied in (B.2), is given by*

$$E(x) = \frac{h^2}{24}\left[f''(\alpha) - f''(\beta)\right] + \mathrm{O}\left(h^4\right),$$

for some α, β where $a \leq \alpha \leq x \leq \beta \leq b$.

Proof. Let δ_{nk} be the Kronecker delta, the derivatives of $F(y;x)$ from (B.3) are evaluated as follows;

$$\begin{aligned}
\frac{\partial^n}{\partial y^n} F(y;x) = \frac{\partial^n}{\partial y^n}\left(\frac{f(y)-f(x)}{y-x}\right) &= \sum_{k=0}^{n} (-1)^k \frac{n!}{(n-k)!} \frac{f^{(n-k)}(y) - \delta_{nk} f(x)}{(y-x)^{k+1}}, \\
&= \frac{1}{(y-x)^{n+1}} \int_x^y (t-x)^n f^{(n+1)}(t)\,\mathrm{d}t, \\
&= \frac{f^{(n+1)}(c)}{n+1}
\end{aligned} \tag{B.4}$$

for some $c \in \mathbb{R}$ such that $x < c < y$, given by the mean value theorem for integrals.

This result is sufficient to prove the theorem. □

B.2 Extension to integrals with a change of variables

A similar proof follows that the error E is of the same order in h and is bounded when a change of variables in the integral is considered; let

$$G(y;x) = \frac{(f \circ g)(y) - f(x)}{g(y) - x} g'(y)$$

where $y \to g(y)$ is a smooth monotonic change of variables.

The trapezoidal rule applied to a integral with the change of variables $y \to g(y)$ is

$$\int_{g^{-1}(a)}^{g^{-1}(b)} \frac{(f \circ g)(y)}{g(y) - x} g'(y)\,\mathrm{d}y = f(x)\left|\frac{b-x}{x-a}\right| + h\left[\frac{1}{2}G_0 + G_1 + \ldots + G_{n-1} + \frac{1}{2}G_n\right] + E, \quad \text{(B.5)}$$

where $nh = g^{-1}(b) - g^{-1}(a)$, and $y_i = g^{-1}(a) + ih$ and $G_i = G(y_i; x)$. Here E is given by (B.3) with F replaced by G, and with evaluation at a and b replaced by $g^{-1}(a)$ and $g^{-1}(b)$ respectively.

Corollary 2 (Change of variables in theorem 3)**.** *If $f(y)$ and $g(y) \in C^\infty(a,b)$, the error in the trapezoidal rule (B.5) is given by*

$$E(x) = \frac{h^2}{12}\left(f''(\alpha)\cdot g'(g^{-1}(a))^2 + \left[\frac{\hat{f}(y) - f(x)}{g(y) - x} g''(y)\right]\Bigg|_{y=g^{-1}(a)} - f''(\beta)\cdot g'(g^{-1}(b))^2 - \left[\frac{\hat{f}(y) - f(x)}{g(y) - x} g''(y)\right]\Bigg|_{y=g^{-1}(b)}\right) + \mathrm{O}\left(h^4\right). \quad \text{(B.6)}$$

for $\hat{f}(y) = (f \circ g)(y)$, and some α and β which vary with x obeying $a < \alpha < x < \beta < b$.

Proof. By the product rule;

$$\frac{\partial^n}{\partial y^n} G(y;x) = \sum_{k=0}^{n} \binom{n}{k} \left[\frac{\partial^k}{\partial y^k} \frac{(f \circ g)(y) - f(x)}{g(y) - x} \right] \left[\frac{\partial^{n-k}}{\partial y^{n-k}} g'(y) \right].$$

Using the chain rule on the first term in the product inside the sum we obtain

$$\frac{\partial^k}{\partial y^k} \left[\frac{(f \circ g)(y) - f(x)}{g(y) - x} \right] = \sum_{j=0}^{k} a_{k,j}(g', g'', \ldots)(y) \left[\frac{\partial^j}{\partial g^j} \left(\frac{f(g) - f(x)}{g - x} \right) \right] \Bigg|_{g=g(y)}$$

for some functions $a_{k,j}(g', g'', \ldots)(y)$ which depend only on the derivatives (with respect to y) of g, as given by Faá di Bruno's formula [31].

Each $a_{k,j}$ is bounded on the interval $(g^{-1}(a), g^{-1}(b))$ as g is chosen to be smooth and continuous there, while terms containing the partial derivatives with respect to g are bounded on (a, b) following from the result given by (B.4). This is sufficient to prove that the coefficient of each h^n term is bounded. The expression for the error term given by (B.6) follows by using the chain rule to replace derivatives with respect to g with derivatives with respect to y. □

It can be easily shown that the limit as $x \to a$ and $x \to b$ is well defined in equation (B.6) provided f and g satisfy the conditions in Corollary 2. This confirms that the error is bounded on the interval from $y = g^{-1}(a)$ up to $y = g^{-1}(b)$. Note also that substituting the identity $g(y) = y$ gives the expected result of Theorem 3.

Appendix C

Derivation of the time dependent fKdV equation

C.1 Long wavelength asymptotics

The variables are rescaled according to long-wavelength asymptotics. Akylas [2] was the first to derive the fKdV as a model equation for these kinds of flow with a pressure disturbance. In order to balance nonlinear growth with dispersion, we assume that the waves are relatively long. For the long-wavelength regime, we consider the flow to have a characteristic length L (e.g. a length related to wavelength) such that $(H/L)^{1/\alpha} = \epsilon \ll 1$, where $\alpha > 0$.

We wish to re-write the equations of fluid motion derived in Appendix A in terms of scaled quantities which are ~ 1, which we will denote with a hat $\hat{}$. Following Akylas [2], the rescaled time is $\epsilon^{-3\alpha}\hat{t} = t$. Assuming that $y \sim 1$, it follows that O(1) spatial variables are given by $(\epsilon^{-\alpha}\hat{x}, \hat{y}) = (x, y)$.

Define a velocity potential φ which is the perturbation potential of a perturbed uniform flow, so $\varphi = \phi - x$. Being a perturbation, it is assumed small, so let the associated O(1) quantity be given by $\epsilon^{\beta}\hat{\varphi} = \varphi$ with $\beta > 0$. The remaining variables

are rescaled arbitrarily for now, let

$$\epsilon^{\gamma}\hat{\eta} = \eta, \quad \epsilon^{\lambda}\hat{p} = p \quad \text{and} \quad \epsilon^{\kappa}\hat{\sigma} = \sigma.$$

Bernoulli's equation (A.9) in the rescaled variables is;

$$\underbrace{\epsilon^{3\alpha+\beta}\hat{\varphi}_{\hat{t}}}_{\text{(a)}} + \frac{1}{2}\underbrace{\epsilon^{2\alpha+2\beta}(\hat{\varphi}_{\hat{x}})^2}_{\text{(b)}} + \frac{1}{2}\epsilon^{2\beta}(\hat{\varphi}_{\hat{y}})^2 + \epsilon^{\alpha+\beta}\hat{\varphi}_{\hat{x}} + \frac{1}{F^2}(\epsilon^{\gamma}\hat{\eta} + \underbrace{\epsilon^{\lambda}\hat{p}}_{\text{(c)}}) = 0.$$

Assume the set of leading order terms in the above equation does not include (c). It follows from the assumption that $\alpha, \beta > 0$ that the set of leading order terms in the dynamic boundary condition cannot include (a) and (b) either. If we balance out the remaining terms, then;

$$\alpha = \beta = \gamma/2.$$

By arbitrarily choosing $\gamma = 1$ (so the free surface height is assumed small), it follows that $(\epsilon^{-1/2}\hat{x}, \hat{y}) = (x, y)$. As the pressure term is to be considered relatively small, we let $\lambda = \kappa = 2$. Thus the other rescaled variables are;

$$\epsilon^{1/2}\hat{\varphi} = \varphi, \quad \epsilon\hat{\eta} = \eta, \quad \epsilon^{2}\hat{p} = p, \quad \epsilon^{2}\hat{\sigma} = \sigma \quad \text{and} \quad \epsilon^{-3/2}\hat{t} = t.$$

The next step is to re-write the equations of the fluid flow in the rescalred variables: Bernoulli's equation is

$$2\epsilon\hat{\varphi}_{\hat{t}} + \epsilon(\hat{\varphi}_{\hat{x}})^2 + (\hat{\varphi}_{\hat{y}})^2 + 2\hat{\varphi}_{\hat{x}} + \frac{2}{F^2}(\hat{\eta} + \epsilon\hat{p}) = 0 \quad \text{for } y = 1 + \epsilon\hat{\eta};$$

Laplace's equation is

$$\epsilon\hat{\varphi}_{\hat{x}\hat{x}} + \hat{\varphi}_{\hat{y}\hat{y}} = 0 \quad \text{for } \epsilon^2\hat{\sigma} < \hat{y} < 1 + \epsilon\hat{\eta};$$

The kinematic conditions are

$$\epsilon^2\hat{\eta}_{\hat{t}} + \epsilon^2\hat{\varphi}_{\hat{x}}\hat{\eta}_{\hat{x}} + \epsilon\hat{\eta}_{\hat{x}} = \hat{\varphi}_{\hat{y}} \quad \text{for } \hat{y} = 1 + \epsilon\hat{\eta} \text{ and}$$
$$\epsilon^3\hat{\varphi}_{\hat{x}}\hat{\sigma}_{\hat{x}} + \epsilon^2\hat{\sigma}_{\hat{x}} = \hat{\varphi}_{\hat{y}} \quad \text{for } \hat{y} = \epsilon^2\hat{\sigma};$$

Finally the far field conditions are;

$$\epsilon\hat{\varphi} + \hat{x} \sim \hat{x} \quad \text{and} \quad \epsilon\hat{\eta} \to 0 \qquad \text{as } \hat{x} \to \infty \text{ and}$$
$$\epsilon\hat{\varphi} + \hat{x} \sim \mu\hat{x} \quad \text{and} \quad \epsilon\hat{\eta} \to \frac{1}{\mu} - 1 \quad \text{as } \hat{x} \to -\infty.$$

We now apply Taylor series expansions to Bernoulli's equation to allow us to determine asymptotic solutions. On $\hat{y} = 1$ we have

$$F^2\left(2\epsilon\hat{\varphi}_{\hat{t}} + \epsilon\hat{\varphi}_{\hat{x}}^2 + \hat{\varphi}_{\hat{y}}^2 + 2\epsilon\hat{\varphi}_{\hat{y}}\hat{\eta}\hat{\varphi}_{\hat{y}\hat{y}} + 2\hat{\varphi}_{\hat{x}} + 2\epsilon\hat{\eta}\hat{\varphi}_{\hat{x}\hat{y}}\right) + 2\hat{\eta} + 2\epsilon\hat{p} + \mathrm{O}\left(\epsilon^2\right) = 0.$$

The following asymptotic expansions are now assumed,

$$F = F_0 + \epsilon F_1 + \dots$$
$$\hat{\eta} = \hat{\eta}_0 + \epsilon\hat{\eta}_1 + \epsilon^2\hat{\eta}_2 + \dots,$$
$$\hat{\varphi} = \hat{\varphi}_0 + \epsilon\hat{\varphi}_1 + \epsilon^2\hat{\varphi}_2 + \dots,$$
$$\hat{p} = \hat{p}_0 + \epsilon\hat{p}_1 + \dots.$$

Comparing the powers of ϵ on $\hat{y} = 1$, we obtain a system of equations that if satisfied, will approximate solutions to Bernoulli's equation up to a certain order of accuracy;

$$\epsilon^0 \Rightarrow \quad 0 = F_0^2\hat{\varphi}_{0\hat{y}}^2 + 2F_0^2\hat{\varphi}_{0\hat{x}} + 2\hat{\eta}_0$$
$$\epsilon^1 \Rightarrow \quad 0 = F_0^2\left(2\hat{\varphi}_{0\hat{t}} + \hat{\varphi}_{0\hat{x}}^2 + 2\hat{\varphi}_{0\hat{y}}\hat{\varphi}_{1\hat{y}} + 2\hat{\varphi}_{0\hat{y}}\hat{\eta}_0\hat{\varphi}_{0\hat{y}\hat{y}} + 2\hat{\varphi}_{1\hat{x}} + 2\hat{\eta}_0\hat{\varphi}_{0\hat{x}\hat{y}}\right) +$$
$$2F_0F_1\left(\hat{\varphi}_{0\hat{y}}^2 + 2\hat{\varphi}_{0\hat{x}}\right) + 2\hat{\eta}_1 + 2\hat{p}_0.$$

C.1.1 Leading order approximation

Gathering all the leading order expressions gives;

$$0 = \hat{\varphi}_{0\hat{y}\hat{y}} \qquad \text{for } 0 < \hat{y} < 1; \tag{C.1}$$
$$0 = \hat{\varphi}_{0\hat{y}} \qquad \text{on } \hat{y} = 1; \tag{C.2}$$
$$0 = \hat{\varphi}_{0\hat{y}} \qquad \text{on } \hat{y} = 0; \text{ and} \tag{C.3}$$
$$0 = {F_0}^2\hat{\varphi}_{0\hat{y}}^2 + 2{F_0}^2\hat{\varphi}_{0\hat{x}} + 2\hat{\eta}_0 \quad \text{on } \hat{y} = 1; \tag{C.4}$$

with far field conditions

$$\hat{\varphi_0} \to 0 \quad \text{and} \quad \hat{\eta}_0 \to 0 \quad \text{as } \hat{x} \to \infty.$$

By integrating $\int_0^{\hat{y}} \mathrm{d}\hat{y}$ twice (C.1) and incorporating (C.3),

$$\hat{\varphi}_0 = f(\hat{x}, \hat{t}) \tag{C.5}$$

for some twice differentiable function $f(\hat{x}, \hat{t})$. Clearly, any partial derivative of $\hat{\phi}_0$ with respect to $\hat{y}$ is zero. By differentiation and substitution into (C.4)

$$\hat{\phi}_{0\hat{x}} = f_{\hat{x}}(\hat{x}, \hat{t}) = -\frac{\hat{\eta}_0}{{F_0}^2}. \tag{C.6}$$

C.1.2 First order terms

Without using the information gained from the ϵ^0 level of approximation, the system of equations at order ϵ is;

$$\begin{aligned}
0 &= \hat{\varphi}_{0\hat{x}\hat{x}} + \hat{\varphi}_{1\hat{y}\hat{y}} && \text{for } 0 < \hat{y} < 1;\\
\hat{\eta}_{0\hat{x}} &= \hat{\varphi}_{1\hat{y}} + \hat{\eta}_0\hat{\varphi}_{0\hat{y}\hat{y}} && \text{on } \hat{y} = 1;\\
0 &= \hat{\varphi}_{1\hat{y}} && \text{on } \hat{y} = 0; \text{ and}\\
0 &= 2{F_0}^2\hat{\varphi}_{0\hat{t}} + {F_0}^2\hat{\varphi}_{0\hat{x}}^2 + 2{F_0}^2\left(\hat{\varphi}_{0\hat{y}}\hat{\varphi}_{1\hat{y}} + \hat{\varphi}_{0\hat{y}}\hat{\eta}_0\hat{\varphi}_{0\hat{y}\hat{y}}\right) + 2F_0F_1\hat{\varphi}_{0\hat{y}}^2 + \\
&\quad 2{F_0}^2\left(\hat{\varphi}_{1\hat{x}} + \hat{\eta}_0\hat{\varphi}_{0\hat{x}\hat{y}}\right) + 4F_0F_1\hat{\varphi}_{0\hat{x}} + 2\hat{\eta}_1 + 2\hat{p}_0 && \text{on } \hat{y} = 1.
\end{aligned}$$

Incorporating the information gained from the order ϵ^0 level of approximation, the order ϵ equations are;

$$0 = -\frac{\hat{\eta}_{0\hat{x}}}{{F_0}^2} + \hat{\varphi}_{1\hat{y}\hat{y}} \qquad \text{for } 0 < \hat{y} < 1; \tag{C.7}$$

$$\hat{\eta}_{0\hat{x}} = \hat{\varphi}_{1\hat{y}} \qquad \text{on } \hat{y} = 1; \tag{C.8}$$

$$0 = \hat{\varphi}_{1\hat{y}} \qquad \text{on } \hat{y} = 0; \text{ and} \tag{C.9}$$

$$0 = 2{F_0}^2\hat{\varphi}_{0\hat{t}} + \frac{\hat{\eta}_0^2}{{F_0}^2} + 2{F_0}^2\hat{\varphi}_{1\hat{x}} - 4F_0F_1\frac{\hat{\eta}_0}{{F_0}^2} + 2\hat{\eta}_1 + 2\hat{p}_0 \quad \text{on } \hat{y} = 1. \tag{C.10}$$

Apply $\int_0^{\hat{y}} \mathrm{d}\hat{y}$ to (C.7), and incorporate the condition (C.9) and the result is

$$\hat{\varphi}_{1\hat{y}} = \hat{y}\frac{\hat{\eta}_{0\hat{x}}}{{F_0}^2}.$$

Using this result in (C.8) implies that either $\eta_0 \equiv 0$ or $F_0 = \pm 1$. The case that $\eta \equiv 0$ is trivial, so we assume the positive solution $F_0 = 1$ (so that the downstream velocity is positive). Applying $\int_0^{\hat{y}} \mathrm{d}\hat{y}$ to $\hat{\varphi}_{1\hat{y}}$;

$$\hat{\varphi}_1 = \frac{1}{2}\hat{y}^2\hat{\eta}_{0\hat{x}} + G(\hat{x}, \hat{t}) \tag{C.11}$$

for some twice differentiable function G.

Use (C.10) to obtain an expression for $G_{\hat{x}}$,

$$G_{\hat{x}} = 2F_1\hat{\eta}_0 - \frac{1}{2}\left(\hat{\eta}_0^2 + \hat{\eta}_{0\hat{x}\hat{x}}\right) - \left(\hat{\eta}_1 + \hat{p}_0 + \hat{\varphi}_{0\hat{t}}\right). \tag{C.12}$$

C.1.3 Second order terms

Laplace's equation at second order, by substituting in (C.11), is

$$\frac{1}{2}\hat{y}^2\hat{\eta}_{0\hat{x}\hat{x}\hat{x}} + G_{\hat{x}\hat{x}} + \varphi_{2\hat{y}\hat{y}} = 0 \tag{C.13}$$

for $0 < \hat{y} < 1$. Applying $\int_0^1 \mathrm{d}\hat{y}$, we get

$$\frac{1}{6}\hat{\eta}_{0\hat{x}\hat{x}\hat{x}} + G_{\hat{x}\hat{x}} + \left[\hat{\varphi}_{2\hat{y}}\right]_{\hat{x},0,\hat{t}}^{\hat{x},1,\hat{t}} = 0. \tag{C.14}$$

The kinematic conditions at order ϵ^2 with (C.5), (C.6), and (C.11) are used to find an expression for the $\hat{\varphi}_{2\hat{y}}$ term in (C.14);

$$\left[\hat{\varphi}_{2\hat{y}}\right]_{\hat{x},0,\hat{t}}^{\hat{x},1,\hat{t}} = \hat{\eta}_{0\hat{t}} + \hat{\eta}_{1\hat{x}} - 2\hat{\eta}_0\hat{\eta}_{0\hat{x}} - \hat{\sigma}_{0\hat{x}}.$$

Then substituting $G_{\hat{x}\hat{x}}$ from (C.12) and the previous equation into (C.14) and collect the terms together to get the fKdV equation

$$6\hat{\eta}_{0\hat{t}} - \hat{\eta}_{0\hat{x}\hat{x}\hat{x}} + 6F_1\hat{\eta}_{0\hat{x}} - 9\hat{\eta}_0\hat{\eta}_{0\hat{x}} = 3\left(\hat{p}_{0\hat{x}} + \hat{\sigma}_{0\hat{x}}\right)$$

Undoing the scalings to retrieve an equation in the original fully nonlinear variables gives the same equation,

$$6\eta_t - \eta_{xxx} - 9\eta\eta_x + 6(F-1)\eta_x = 3\left(p_x + \sigma_x\right)$$

C.2 Forcing terms in non-dimensional variables

The forcing terms considered in this thesis are either Gaussian, such as the pressure disturbance (2.1.2), or based on a sum of hyperbolic tangent functions such as for a topographical disturbance (2.1.3). To determine the scale of the parameters, for these forcings, we examine the condition that as $\epsilon \to 0$,

$$\int_{-\infty}^{\infty} \hat{\sigma}(\hat{x})\,\mathrm{d}\hat{x} \sim 1. \tag{C.15}$$

The same condition, where σ is replaced by p, applies to a pressure disturbance, and as the results for the scale of the variables are the same, we only perform the analysis using the topographical function σ, and so the hyperbolic tangent function type of forcing is examined.

By integrating $\sigma(x) = \epsilon^2\hat{\sigma}(\hat{x})$ over the whole domain

$$\int_{-\infty}^{\infty} \hat{\sigma}(\hat{x})\,\mathrm{d}\hat{x} = \epsilon^{-3/2}\int_{-\infty}^{\infty} \sigma(x)\,\mathrm{d}x. \tag{C.16}$$

For the smoothed disturbance using hyperbolic tangent functions,

$$\begin{aligned}
\sigma(x) &\approx \frac{A}{2l}\left[\tanh B(x+l/2) - \tanh B(x-l/2)\right], \\
\Rightarrow \quad \int_{-\infty}^{\infty}\sigma(x)\,\mathrm{d}x &= \frac{A}{2Bl}\lim_{R\to\infty}\left[\ln\cosh B(x+l/2) - \ln\cosh B(x-l/2)\right]_{-R}^{R}, \\
&= \frac{A}{2Bl}\lim_{R\to\infty}\left[\ln\frac{\cosh B(x+l/2)}{\cosh B(x-l/2)}\right]_{-R}^{R}.
\end{aligned}$$

The limits can be evaluated by letting $a = \ln\frac{\cosh B(\pm R+l/2)}{\cosh B(\pm R-l/2)}$, then from the expo-

nential of a (using continuity),

$$e^a = \frac{\cosh B(\pm R + l/2)}{\cosh B(\pm R - l/2)},$$
$$\Rightarrow \quad e^{\mp Bl/2+a} + e^{-2BR\pm Bl/2+a} = e^{\pm Bl/2} + e^{-2BR\mp Bl/2}.$$

It is clear that $a \to \pm Bl$ when taking the limit $R \to \infty$. Therefore

$$\lim_{R\to\infty} \left[\ln \frac{\cosh B(x + l/2)}{\cosh B(x - l/2)} \right]_{-R}^{R} = 2Bl.$$

So

$$\int_{-\infty}^{\infty} \sigma(x)\, \mathrm{d}x = A.$$

Now if $\hat{\sigma}(\hat{x}) = \hat{A}\delta(x)$, then by (C.16)

$$\int_{-\infty}^{\infty} \hat{\sigma}(\hat{x})\, \mathrm{d}\hat{x} = \int_{-\infty}^{\infty} \hat{A}\delta(\hat{x})\, \mathrm{d}\hat{x} = \epsilon^{-3/2}A.$$

Using the value of the integral of (or the convolution with) a delta function, the previous equation implies that $\hat{A} = \epsilon^{-3/2}A$. The condition (C.15) informs us that $A \sim \epsilon^{3/2}$. Recalling that the height/depth of the disturbance is $\frac{A}{l} \sim \epsilon^2$, it follows that $l \sim \epsilon^{-1/2}$. $l \sim \epsilon^{-1/2}$ is consistent with the long wavelength scaling, thus the bump/trench needs to be on the scale of a wavelength.

Repeating this same work for a Gaussian function, the result that $A \sim \epsilon^{3/2}$ is found to apply to the Gaussian disturbances as well. Then given the scaling for either type of disturbance, then $AB/\sqrt{\pi} \sim \epsilon^2$, and it follows that $B/\sqrt{\pi} \sim \epsilon^{1/2}$.

Appendix D

Linearisation of flow in the far field

For this derivation we again consider a perturbation potential given by $\varphi = \phi - x$. Then we have the following governing equations and boundary conditions to satisfy from Appendix A;

$$0 = \varphi_{xx} + \varphi_{yy} \qquad \text{for } \sigma < y < 1 + \eta; \tag{D.1}$$

$$\varphi_y = \varphi_x \eta_x + \eta_x \qquad \text{on } y = 1 + \eta; \tag{D.2}$$

$$\varphi_y = \varphi_x \sigma_x + \sigma_x \qquad \text{on } y = \sigma; \text{ and} \tag{D.3}$$

$$0 = F^2({\varphi_x}^2 + {\varphi_y}^2) + 2F^2\varphi_x + 2(y + p - 1) \qquad \text{on } y = 1 + \eta. \tag{D.4}$$

As an expression for the flow in the far field is desired, we also consider that as $x \to \infty$, the radiation condition must be satisfied as well as the following;

$$\varphi + x \sim x \quad \text{and} \quad \eta \to 0 \quad \text{as } x \to \infty. \tag{D.5}$$

Let there be some small parameter $\epsilon \ll 1$ such that $\varphi = \epsilon\varphi_1$, $\eta = \epsilon\eta_1$, $\sigma = \epsilon\sigma_1$ and $p = \epsilon p_1$ are all of the same order. By substituting these scaled quantities into the system (D.1) – (D.4), expanding about $y = 1$ and $y = 0$ in the boundary conditions, and equating the highest order terms, then to first order the unscaled

variables must satisfy;

$$\begin{aligned} F^2\varphi_x + \eta + p = 0 \quad & \text{on } y = 1; \\ \varphi_{xx} + \varphi_{yy} = 0 \quad & \text{for } 0 < y < 1; \\ \eta_x - \varphi_y = 0 \quad & \text{on } y = 1, \text{ and} \\ \sigma_x - \varphi_y = 0 \quad & \text{on } y = 0. \end{aligned}$$

Let $p = \sigma \equiv 0$, and assume that the solution for φ can be expressed as a (real) linear combination of real valued eigenfunctions $X_\lambda(x)Y_\lambda(x)$ given eigenvalues $\lambda \in \Lambda \subseteq \mathbb{C}$. The eigenfunctions and eigenvalues are found by satisfying the following equations;

$$X_\lambda''(x) = \lambda X_\lambda(x) \qquad \text{for } 0 < y < 1; \tag{D.6}$$

$$Y_\lambda''(y) = -\lambda Y_\lambda(y) \quad \text{on } 0 < y < 1; \tag{D.7}$$

$$-F^2 Y_\lambda''(1) + Y_\lambda'(1) = 0 \qquad \text{for } y = 1; \text{ and} \tag{D.8}$$

$$Y_\lambda'(0) = 0 \qquad \text{for } y = 0. \tag{D.9}$$

Suppose $Y_\lambda = \exp(k_\lambda y)$, and substitute this into (D.7) and incorporate the boundary conditions (D.8) and (D.9). These are all satisfied by,

$$Y_\lambda = e^{k_\lambda y} + e^{-k_\lambda y}$$

for $\lambda \neq 0$, where $k_\lambda = \sqrt{-\lambda}$ (using the positive branch) and

$$\frac{\tanh(k_\lambda)}{k_\lambda} - F^2 = 0. \tag{D.10}$$

A solution for $\lambda = 0$ is given (without loss of generality) by

$$Y_0(y) = 1.$$

Equating the imaginary component of equation (D.10), then either $\mathrm{Re}\,(k_\lambda) = 0$

or Im $(k_\lambda) = 0$. Let $k_\lambda = a_\lambda + ib_\lambda$, then either

$$\frac{\tanh a_\lambda}{a_\lambda} - F^2 = 0 \quad \text{for } b_\lambda = 0 \text{ or}$$
$$\frac{\tan b_\lambda}{b_\lambda} - F^2 = 0 \quad \text{for } a_\lambda = 0,$$

thus there are a countable number of solutions for λ when $F > 1$. The radiation condition is not satisfied in the far field for the case of $b_\lambda = 0$, as the corresponding solutions for X_λ are oscillatory, thus only the case $a_\lambda = 0$ is required for a solution in the far field.

In the case that $a_\lambda = 0$ we have purely imaginary eigenvalues and Y_λ is given (for $\lambda \neq 0$) by

$$Y_\lambda = \cos(b_\lambda y).$$

From the differential equation for X_λ (for $\lambda \neq 0$) and given the requirement that solutions decay as $x \to \infty$ due to (D.5), it follows that

$$X_\lambda = D_\lambda e^{-b_\lambda x}$$

and for the particular case of $\lambda = 0$ using the same conditions on the solutions it follows that $X_0 = 0$.

Substitute these into the definition of the complex velocity w and

$$\begin{aligned} w = \frac{\mathrm{d}f}{\mathrm{d}z} &= \frac{\partial \phi}{\partial x} - i\frac{\partial \phi}{\partial y}, \\ &= 1 + \frac{\partial \varphi}{\partial x} - i\frac{\partial \varphi}{\partial y} = u - iv. \\ &= 1 + \sum_{\lambda \in \Lambda} D_\lambda e^{-b_\lambda x}(cos(b_\lambda y) + i \sin(b_\lambda y). \end{aligned}$$

Using $\phi \sim x$ and $y \to 1$ as $x \to \infty$, an approximation as $\phi \to \infty$ is given by

$$u - iv \approx 1 + D_\mathrm{d} e^{-\lambda_0 \phi}(\cos \lambda_0 - i \sin \lambda_0) \tag{D.11}$$

for some real D_{d}, and λ_0 being the smallest positive solution of

$$\tan \lambda_0 = F^2 \lambda_0.$$

In the case of flow which satisfies the radiation condition and that $y \to 1$ and $\phi \sim x$ as $x \to -\infty$, then

$$u - iv \approx 1 + D_{\mathrm{u}} e^{\lambda_0 \phi} (\cos \lambda_0 + i \sin \lambda_0) \tag{D.12}$$

as $\phi \to \infty$, for some real D_{u}.

Appendix E

Calculation of interior streamlines using boundary integrals

The streamlines and equipotential lines can be evaluated using a boundary-integral approach derived using the conformal mapping $\zeta = e^{\pi(\phi+i\psi)}$ from (2.2.8). Streamlines are calculated by fixing a value of ψ and evaluating $x(\zeta)$ and $y(\zeta)$ at discrete values of ϕ. An expression for $x(\zeta)$ and $y(\zeta)$ is found by using the transformed velocity variables τ and θ given by (2.2.23), and integrating the expression for the complex velocity given by (2.2.9), giving

$$\begin{aligned} x(\zeta) &= \int_0^{\phi} \exp\left(-\tau(e^{\hat{\phi}+\mathrm{i}\psi})\right) \cos\left(\theta(e^{\hat{\phi}+\mathrm{i}\psi})\right)\, \mathrm{d}\hat{\phi} \text{ and} \\ y(\zeta) &= \psi + \int_{-\infty}^{\phi} \exp\left(-\tau(e^{\hat{\phi}+\mathrm{i}\psi})\right) \sin\left(\theta(e^{\hat{\phi}+\mathrm{i}\psi})\right)\, \mathrm{d}\hat{\phi}. \end{aligned} \tag{E.1}$$

The two integrals above are evaluated numerically using adaptive integration supplied by the `quad()` routine in MATLAB. A boundary-integral method is used to determine $\tau(\zeta)$ and $\theta(\zeta)$ in the integrands on the right hand side of (E.1). The boundary integrals are evaluated using $\tau_s(\phi)$ and $\theta_s(\phi)$ from the solution to the free-surface problem, as well as the known function $\theta_b(\phi)$.

Consider a contour Γ in the $\zeta = \alpha + i\beta$ plane, shown schematically in figure

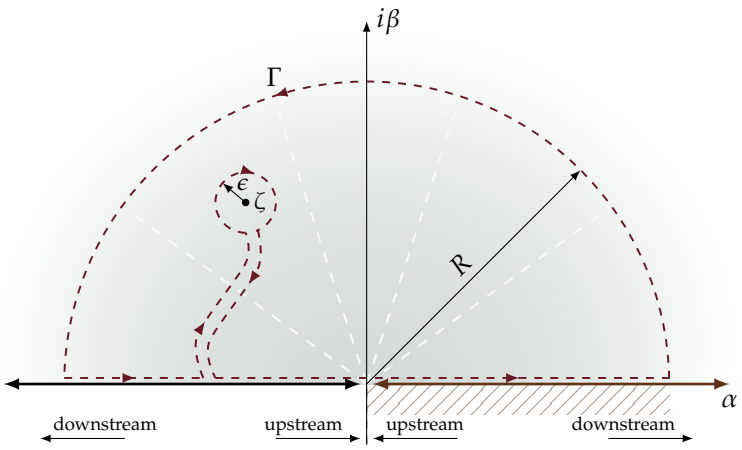

Figure E.1: Sketch of the contour Γ in the $\alpha + i\beta$ plane used to evaluate τ and θ via the Cauchy integral formula.

E.1. The contour Γ is composed of a semi-circle of radius R in the $\beta > 0$ half-plane, centred at the origin, and the line segment from $-R$ to R along the the α axis.

Cauchy's integral theorem [5] is applied to the function $\tau(\zeta) - \mathrm{i}\theta(\zeta)$ using this contour, and thus for any point ζ enclosed by Γ we have

$$\tau(\zeta) - \mathrm{i}\theta(\zeta) = \frac{1}{2\pi\mathrm{i}} \lim_{R\to\infty} \int_\Gamma \frac{\tau(\hat{\zeta}) - \mathrm{i}\theta(\hat{\zeta})}{\hat{\zeta} - \zeta}\, \mathrm{d}\hat{\zeta}.$$

Now, applying Lemma 1 from §2.2.1 to the semi-circular segment of the contour gives

$$\tau(\zeta) - \mathrm{i}\theta(\zeta) = \frac{1}{2\pi\mathrm{i}} \lim_{R\to\infty} \int_{-R}^{R} \frac{\tau(\hat{\alpha}) - \mathrm{i}\theta(\hat{\alpha})}{\hat{\alpha} - \zeta}\, \mathrm{d}\hat{\alpha}. \tag{E.2}$$

To evaluate (E.2) numerically, the real and imaginary parts are separated, thus

$$\tau(\zeta) = \frac{1}{2\pi} \int_{-\infty}^{\infty} \frac{\tau(\hat{\alpha}) e^{\pi\phi} \sin\pi\psi - \theta(\hat{\alpha})(\hat{\alpha} - e^{\pi\phi}\cos\pi\psi)}{|\hat{\alpha} - e^{\pi(\phi+\mathrm{i}\psi)}|^2}\, \mathrm{d}\hat{\alpha} \text{ and} \tag{E.3}$$

$$\theta(\zeta) = \frac{1}{2\pi} \int_{-\infty}^{\infty} \frac{\tau(\hat{\alpha})(\hat{\alpha} - e^{\pi\phi}\cos\pi\psi) + \theta(\hat{\alpha}) e^{\pi\phi}\sin\pi\psi}{|\hat{\alpha} - e^{\pi(\phi+\mathrm{i}\psi)}|^2}\, \mathrm{d}\hat{\alpha} \tag{E.4}$$

where $\zeta = e^{\pi(\phi+\mathrm{i}\psi)}$. The domain corresponding to integration over the free surface,

$\hat{\alpha} < 0$, is then evaluated separately from the integration over the topography, where $\hat{\alpha} > 0$.

For integration over the free surface, the integral is broken up into three further sub-domains. The first being the interval $-e^{\pi\phi_m} < \hat{\alpha} < -e^{-\pi\phi_m}$ which corresponds to where the free-surface variables τ and θ are known from the boundary-integral calculations for the free-surface. The contribution in this domain is evaluated by fitting a spline, using MATLAB's `spline()` function, to the known values of τ_s and θ_s from the discrete grid, and integrating the resulting piece-wise polynomial. The other domains correspond to the far upstream and far downstream regions of the flow, where the variables τ_s and θ_s are approximately known via the linearised solution, given by equations (D.11) and (D.12) derived in Appendix D. The values for the parameters D and λ in the linearised solution are obtained from the free-surface calculations. These contributions are evaluated using the same mappings from §4.2 and MATLAB's adaptive Gauss-Kronrod numerical integration routine, `quadgk()`.

The integral over the channel topography, where $\hat{\alpha} > 0$, is evaluated by truncating the domain and ignoring the contributions from the far field, as the contribution is negligible outside of the domain $e^{-2\pi\phi_m} < \hat{\alpha} < e^{2\pi\phi_m}$. The value of τ in this interval can be calculated using the same approach outlined in §4.2.1, while the angle of the topography, $\theta(\alpha > 0)$, is given by (4.2.9). The integral over this truncated domain is evaluated using MATLAB's `quadgk()` function.

Using this procedure, equations (E.3) and (E.4) can be numerically evaluated for any value of ϕ and any value of $\psi \in (0, 1)$. The numerical integration functions supplied by MATLAB were called with a requested relative error tolerance of 10^{-6}. This was sufficient to ensure that the streamlines $x(\zeta)$ and $y(\zeta)$ found by numerically integrating (E.1) were accurate to the order of 10^{-3} in terms of the absolute error.

Bibliography

[1] ABRAMOWITZ, M. & STEGUN, I. 1972 *Handbook of mathematical functions: with formulas, graphs, and mathematical tables*. Courier Dover Publications.

[2] AKYLAS, T. R. 1984 On the excitation of long nonlinear water waves by a moving pressure distribution. *Journal of Fluid Mechanics* **141**, 455–466.

[3] ALLGOWER, E. L. & GEORG, K. 1990 *Numerical continuation methods: an introduction*. Springer Verlag.

[4] BAINES, P. 1998 *Topographic effects in stratified flows*. Cambridge University Press.

[5] BAK, J. & NEWMAN, D. J. 1997 *Complex Analysis*. Springer Science, New York, 2nd edition.

[6] BATCHELOR, G. 2000 *An introduction to fluid dynamics*. Cambridge University Press.

[7] BINDER, B. J. 2005 *Numerical and Analytical Studies of Nonlinear Free Surface Flows Past Distrubances*. Ph.D. thesis, University of East Anglia.

[8] BINDER, B. J., DIAS, F. & VANDEN-BROECK, J.-M. 2007 Influence of rapid changes in a channel bottom on free-surface flows. *IMA Journal of Applied Mathematics* **73**(1), 254–273.

[9] BINDER, B. J. & VANDEN-BROECK, J.-M. 2007 The effect of disturbances on the flows under a sluice gate and past an inclined plate. *Journal of Fluid Mechanics* **576**, 475–490.

[10] BINDER, B. J., VANDEN-BROECK, J.-M. & DIAS, F. 2005 Forced solitary waves and fronts past submerged obstacles. *Chaos* **15**(3), 37106.

[11] BYATT-SMITH, J. G. B. & LONGUET-HIGGINS, M. S. 1976 On the speed and profile of steep solitary waves. *Proceedings of the Royal Society of London, Series A* **350**(1661), 175–189.

[12] CAMASSA, R. & WU, T. Y. 1991 Stability of forced steady solitary waves. *Philosophical Transactions of the Royal Society of London, Series A* **337**(1648), 429–466.

[13] CASCIOLA, C. M. & LANDRINI, M. 1996 Nonlinear long waves generated by a moving pressure disturbance. *Journal of Fluid Mechanics* **325**, 399–418.

[14] CHARDARD, F., DIAS, F., NGUYEN, H. Y. & VANDEN-BROECK, J.-M. 2010 Stability of some stationary solutions to the forced KdV equation with one or two bumps. *Journal of Engineering Mathematics* **70**(1-3), 175–189.

[15] DIAS, F. & VANDEN-BROECK, J.-M. 1989 Open channel flows with submerged obstructions. *Journal of Fluid Mechanics* **206**, 155–170.

[16] DIAS, F. & VANDEN-BROECK, J.-M. 2002 Generalised critical free-surface flows. *Journal of Engineering Mathematics* **42**(3-4), 291–301.

[17] DIAS, F. & VANDEN-BROECK, J.-M. 2004 Trapped waves between submerged obstacles. *Journal of Fluid Mechanics* **509**, 93–102.

[18] EE, B. K. & CLARKE, S. R. 2007 Weakly dispersive hydraulic flows in a contraction : Parametric solutions and linear stability. *Physics of Fluids* **19**(5), 056601.

[19] EE, B. K., GRIMSHAW, R. H. J., CHOW, K. W. & ZHANG, D.-H. 2011 Steady transcritical flow over an obstacle: Parametric map of solutions of the forced extended Korteweg-de Vries equation. *Physics of Fluids* **23**(4), 046602.

[20] EE, B. K., GRIMSHAW, R. H. J., ZHANG, D.-H. & CHOW, K. W. 2010 Steady transcritical flow over a hole: Parametric map of solutions of the forced Korteweg-de Vries equation. *Physics of Fluids* **22**(5), 056602.

[21] ELCRAT, A. R. & MILLER, K. G. 2006 Free Surface Waves in Equilibrium with a Vortex. *European Journal of Mechanics B/Fluids* **25**(2), 255–266.

[22] ERTEKIN, R. C. 1986 Waves caused by a moving disturbance in a shallow channel of finite width. *Journal of Fluid Mechanics* **169**, 275–292.

[23] FORBES, L. K. & SCHWARTZ, L. W. 1982 Free-surface flow over a semicircular obstruction. *Journal of Fluid Mechanics* **114**, 299–314.

[24] GALASSI, M., THEILER, J., DAVIS, J., GOUGH, B., JUNGMAN, G., ALKEN, P., BOOTH, M. & ROSSI, F. 2009 *GNU Scientific Library Reference Manual*. Network Theory Ltd., 3rd edition.

[25] GRADSHTEIN, I. S., RYZHIK, I. M. & JEFFREY, A. 2000 *Table of integrals, series, and products*. Academic Press, 6th edition.

[26] GRIMSHAW, R. H. J. & MALEEWONG, M. 2013 Stability of steady gravity waves generated by a moving localised pressure disturbance in water of finite depth. *Physics of Fluids* **25**(7), 076605.

[27] GRIMSHAW, R. H. J. & SMYTH, N. 1986 Resonant flow of a stratified fluid over topography. *Journal of Fluid Mechanics* **169**, 429–464.

[28] GRIMSHAW, R. H. J., ZHANG, D.-H. & CHOW, K. W. 2007 Generation of solitary waves by transcritical flow over a step. *Journal of Fluid Mechanics* **587**, 235–254.

[29] HAVELOCK, T. H. 1918 Periodic irrotational waves of finite height. *Proceedings of the Royal Society of London, Series A* **95**(665), 38–51.

[30] HUNTER, J. K. & VANDEN-BROECK, J.-M. 1983 Accurate computations for steep solitary waves. *Journal of Fluid Mechanics* **136**, 63–71.

[31] JOHNSON, W. P. 2002 The Curious History of Faa di Bruno's Formula. *The American Mathematical Monthly* **109**(3), 217–234.

[32] KATAOKA, T. 2006 The stability of finite-amplitude interfacial solitary waves. *Fluid Dynamics Research* **38**, 831–867.

[33] KORTEWEG, D. J. & DE VRIES, G. 1895 On the change of form of long waves advancing in a rectangular canal and on a new type of long stationary waves. *Philosophical Magazine, Series 5* **39**(240), 422–433.

[34] KRYLOV, V. I. 1962 *Approximate Calculation of Integrals*. Macmillan Co, New York.

[35] LAMB, H. 1932 *Hydrodynamics*. Cambridge University Press.

[36] LEE, S.-J., YATES, G. T. & WU, T.-Y. 1989 Experiments and analyses of upstream-advancing solitary waves generated by moving disturbances. *Journal of Fluid Mechanics* **199**, 569–593.

[37] LENAU, C. W. 1966 The solitary wave of maximum amplitude. *Journal of Fluid Mechanics* **26**, 309–320.

[38] LONGUET-HIGGINS, M. S. & CLEAVER, R. P. 1994 Crest instabilities of gravity waves. Part 1. The almost-highest wave. *Journal of Fluid Mechanics* **258**, 115–129.

[39] LONGUET-HIGGINS, M. S. & FENTON, J. D. 1974 On the Mass, Momentum, Energy and Circulation of a Solitary Wave. II. *Proceedings of the Royal Society of London, Series A* **340**(1623), 471–493.

[40] LONGUET-HIGGINS, M. S. & FOX, M. J. H. 1996 Asymptotic theory for the almost-highest solitary wave. *Journal of Fluid Mechanics* **317**, 1–19.

[41] LONGUET-HIGGINS, M. S. & TANAKA, M. 1997 On the crest instabilities of steep surface waves. *Journal of Fluid Mechanics* **336**, 51–68.

[42] LUSTRI, C. J., MCCUE, S. W. & BINDER, B. J. 2012 Free surface flow past topography: a beyond-all-orders approach. *European Journal of Applied Mathematics* **23**(4), 441–467.

[43] MAKLAKOV, D. V. 2002 Almost-highest gravity waves on water of finite depth. *European Journal of Applied Mathematics* **13**(1), 67–93.

[44] MALOMED, B. A. 1988 Interaction of a moving dipole with a soliton in the KdV equation. *Physica D: Nonlinear Phenomena* **32**(3), 393–408.

[45] MATLAB 2011 *(R2011b)*. The Mathworks Inc., Natick, Massachusetts.

[46] MCLEOD, J. B. 1997 The Stokes and Krasovskii conjectures for the wave of greatest height. *Studies in Applied Mathematics* **98**(4), 311–333.

[47] MILES, J. W. 1986 Stationary, transcritical channel flow. *Journal of Fluid Mechanics* **162**, 489–499.

[48] NOBLE, B. & BEIGHTON, S. 1980 Error estimates for three methods of evaluating Cauchy principal value integrals. *IMA Journal of Applied Mathematics* **26**(4), 431–446.

[49] PETHIYAGODA, R., MCCUE, S. W. & MORONEY, T. J. 2014 What is the apparent angle of a Kelvin ship wave pattern? *Journal of Fluid Mechanics* **758**, 468–485.

[50] PETHIYAGODA, R., MCCUE, S. W., MORONEY, T. J. & BACK, J. M. 2014 Jacobian-free Newton-Krylov methods with GPU acceleration for computing nonlinear ship wave patterns. *Journal of Computational Physics* **269**, 297–313.

[51] SCHWARTZ, L. W. & FENTON, J. D. 1982 Strongly nonlinear waves. *Annual Review of Fluid Mechanics* **14**(1), 39–60.

[52] SHEN, J., TANG, T. & WANG, L. 2011 *Spectral methods: algorithms, analysis and applications*. Springer-Verlag.

[53] SHEN, S. S.-P. 1991 Locally forced critical surface waves in channels of arbitrary cross section. *Journal of Applied Mathematics and Physics (ZAMP)* **42**(1), 122–138.

[54] SHEN, S. S.-P. 1993 *A course on nonlinear waves*. Kluwer Academic, Dordrecht and Boston, third edition.

[55] SHEN, S. S.-P. 1996 On the accuracy of the stationary forced Korteweg-de Vries equation as a model equation for flows over a bump. *Quarterly of Applied Mathematics* **53**(4), 701–719.

[56] SHEN, S. S.-P., MANOHAR, R. P. & GONG, L. 1995 Stability of the lower cusped solitary waves. *Physics of Fluids* **7**(10), 2507–2509.

[57] STOKER, J. J. 1957 *Water waves*. Interscience Publishers Inc.

[58] STOKES, G. G. 1847 On the theory of oscillatory waves. *Transactions Cambridge Philosophical Society* **8**, 441–455.

[59] STOKES, G. G. 1880 Supplement to a paper on the theory of oscillatory waves. *Mathematical and Physical Papers* **1**, 314–326.

[60] TANAKA, M. 1986 The stability of solitary waves. *Physics of Fluids* **29**(3), 650.

[61] TOLAND, J. F. 1978 On the existence of a wave of greatest height and Stokes's conjecture. *Proceedings of the Royal Society of London, Series A* **363**(1715), 469–485.

[62] TREFETHEN, L. N. 2000 *Spectral methods in MATLAB*. SIAM, tenth edition.

[63] TREFETHEN, L. N. 2013 *Approximation theory and approximation practice*. SIAM.

[64] VANDEN-BROECK, J.-M. 1986 Steep gravity waves: Havelock's method revisited. *Physics of Fluids* **29**(9), 3084–3085.

[65] VANDEN-BROECK, J.-M. 1987 Free surface flow over an obstruction in a channel. *Physics of Fluids* **30**(8), 2315–2317.

[66] VANDEN-BROECK, J.-M. 1997 Numerical calculations of the free-surface flow under a sluice gate. *Journal of Fluid Mechanics* **330**, 339–347.

[67] VANDEN-BROECK, J.-M. & SCHWARTZ, L. W. 1979 Numerical computation of steep gravity waves in shallow water. *Physics of Fluids* **22**(10), 1868–1871.

[68] WADE, S. L., BINDER, B. J., MATTNER, T. W. & DENIER, J. P. 2014 On the free-surface flow of very steep forced solitary waves. *Journal of Fluid Mechanics* **739**, 1–21.

[69] WILLIAMS, J. M. 1981 Limiting gravity waves in water of finite depth. *Philosophical Transactions of the Royal Society of London, Series A* **302**(1466), 139–188.

[70] WU, T. Y. 1987 Generation of upstream advancing solitons by moving disturbances. *Journal of Fluid Mechanics* **184**, 75–99.

[71] ZHANG, D.-H. & CHWANG, A. T. 1996 Numerical study of nonlinear shallow water waves produced by a submerged moving disturbance in viscous flow. *Physics of Fluids* **8**(1), 147–155.